FRIEDRICH-SCHILLER-UNIVERSITÄT JENA
Chemisch-Geowissenschaftliche Fakultät
Institut für Geographie
Lehrstuhl für Fernerkundung

Masterarbeit zur Erlangung des akademischen Grades
Master of Science (M.Sc.)

Influence of environmental parameters on quantifying point-source emissions of CO_2 and CH_4 from observations of the future DLR satellite mission CO2Image

Anna Lindenberger

Geb. 10.01.1996 in Bietigheim-Bissingen

Studiengang: Geoinformatik M.Sc.

Jena, November 2022

Erstgutachterin: Prof. Dr. Christiane Schmullius

Zweitgutachter: Dr. Dietrich Feist

Erstellt am Deutschem Zentrum für Luft- und Raumfahrt (DLR), Oberpfaffenhofen

Abstract

Over the last decades climate observations show an increase of global land and sea surface temperature. As there is scientific consensus that the dominant cause of this global warming is the increase in anthropogenic greenhouse gas (GHG) emissions, countries must report their GHG emissions to the United Nations Framework Convention on Climate Change (UNFCCC). The CO2Image mission of the German Aerospace Center (DLR) with a spatial resolution of 50 x 50 m^2 will be able to observe specifically large and medium-sized point sources, which are responsible for around 88% of the global CO_2 emissions. The independent verification of reported emissions through CO2Image will be a great contribution to mitigate climate change.

This thesis examines the impact of scattering due to aerosols on the reflected solar radiation in the shortwave infrared (SWIR) spectrum which is measured by the CO2Image instrument. To investigate the influence of aerosol scattering on the quantification of emitted CO_2, this work performs simulations based on the retrieval algorithm RemoTeC by varying values for the parameters of the aerosol optical thickness, aerosol height and size distribution. This leads to the result that for a spatial resolution of 50 x 50 m^2 scattering due to aerosols can be neglected if the aerosols are homogenously dispersed over the whole scene and the location and size of the plume is known. Contrarily, if there is no knowledge about the location and size of the plume, the automatic plume detection fails to find the entire plume and thus the CO_2 concentration is underestimated. However, if the aerosol optical thickness, aerosol height or aerosol size only changes inside the plume and the background still has a low aerosol amount, significant errors occur. As aerosol scattering shortens the light path of the measured reflected solar radiation, the integrated mass enhancement (IME) is underestimated. Hence, with increasing values for the three aerosol parameters the true CO_2 concentrations are significantly underestimated for a heterogeneous aerosol scenario. Furthermore, a strong correlation of the surface albedo with the errors in the retrieved CO_2 was found. While dark surfaces reinforce the underestimation of the true CO_2 due to aerosol scattering, bright surfaces can be a mediator for errors caused by aerosol scattering.

Zusammenfassung

Die Klimabeobachtungen der letzten Jahrzehnte zeigen einen Anstieg der globalen Land- und Meeresoberflächentemperatur. Es herrscht wissenschaftlicher Konsens darüber, dass die Hauptursache für diese globale Erwärmung der Anstieg der anthropogenen Treibhausgase ist. Die einzelnen Staaten müssen ihre Treibhausgasemissionen an die UNFCCC (United Nations Framework Convention on Climate Change) melden. Die CO2Image-Mission des Deutschen Zentrums für Luft- und Raumfahrt (DLR) wird mit einer räumlichen Auflösung von 50 x 50 m^2 insbesondere große und mittelgroße Punktquellen beobachten können, die für rund 88 % der globalen CO_2-Emissionen verantwortlich sind. Die unabhängige Verifizierung der gemeldeten Emissionen durch CO2Image ist daher ein wichtiger Beitrag zur Abschwächung des Klimawandels.

Diese Arbeit untersucht den Einfluss Aerosolstreuung auf die reflektierte Sonnenstrahlung im kurzwelligen Infrarot (SWIR), die mit dem CO2Image-Instrument gemessen wird. Um den Einfluss der Aerosole auf die Quantifizierung des emittierten CO_2 zu untersuchen, werden Simulationen mit dem Retrieval-Algorithmus RemoTeC mit unterschiedlichen Werten für die Parameter der Aerosolmenge, der Aerosolhöhenverteilung und der Aerosolgrößenverteilung durchgeführt. Diese Studie stellt fest, dass bei einer räumlichen Auflösung von 50 x 50 m^2 die Streuung durch Aerosole vernachlässigt werden kann, wenn die Aerosole homogen über die gesamte Szene verteilt sind und die Lage und Größe der Emissionsfahne bekannt ist. Allerdings kommt es zu einer Unterschätzung der CO_2 Konzentration, wenn die Lage und Größe der Emissionsfahne nicht bekannt ist, da bei einer automatischen Detektion der Emissionsfahne nicht die komplette Emissionsfahne gefunden wird. Wenn sich jedoch die Aerosolmenge, die Höhe oder die Größe der Aerosole innerhalb der Emissionsfahne ändert und der Hintergrund noch eine geringe Aerosolmenge aufweist, kommt es zu einer deutlichen Unterschätzung der wahren CO_2-Konzentrationen. Da die Aerosolstreuung den Lichtweg der gemessenen reflektierten Sonnenstrahlung verkürzt, wird für eine heterogene Aerosolverteilung das Integrated mass enhancement (IME), mit steigenden Werten aller drei Aerosolparameter deutlich unterschätzt. Ergänzend wurde eine starke Korrelation zwischen der Oberflächenalbedo und den Fehlern bei der CO_2-Messung festgestellt. Während dunkle Oberflächen die Unterschätzung des CO_2 aufgrund von Aerosolstreuung verstärken, können helle Oberflächen die Fehler, die durch Aerosolstreuung verursacht werden, verringern.

Contents

List of Abbreviations

Alt1	Parameter for the aerosol height distribution
ASI	Italian Space Agency (Agenzia Spaziale Italiana)
C3S	Copernicus Climate Change Service
CarbonSat	Carbon Monitoring Satellite
CDS	Copernicus Climate Data Store
CH_4	Methane
CNES	French Space Agency (Centre national d'études spatiales)
CO_2	Carbon dioxide
CO_2FFI	CO2 coming from fossil fuels or
CO2M	Copernicus CO2 Monitoring
Cot_inp	Cirrus optical thickness
DKRZ	German Climate Computer Center (Deutsches Klimarechenzentrum)
DLR	German Aerospace Center (Deutsches Zentrum für Luft- und Raumfahrt)
ECV	Essential Climate Variable
EnMAP	Environmental Mapping and Analysis Program
ENVISAT	ENVIronmental SATtellite
ESA	European Space Agency
EU	European Union
GCOS	Global Climate Observing System
GHG	GreenHouse Gas
GHGSat	GreenHouse Gas Satellite
GOSAT	Greenhouse Gases Observing SaTellite
IEA	International Energy Agency
IME	Integrated Mass Enhancement
IR	Infrared Radiation
JAXA	Japan Aerospace Exploration Agency

LEO	Low Earth Orbit
LES	Large Eddy Simulations
LIDAR	LIght Detection And Ranging
N2	Nitrogen
NASA	National Aeronautics and Space Administration
O2	Oxygen
O3	Ozon
OCO-2	Orbiting Carbon Observatory-2
OS	Optical Sensor Systems
Ot_inp	Total optical thickness
PRISMA	Hyperspectral Precursor of the Application Mission (PRecursore IperSpettrale della Missione Applicativa)
Reff	Parameter for the aerosol size distribution
RS	Remote Sensing
SCIMACHY	Scanning Imaging Absorption Spectrometer for Atmospheric Chartography
SNR	Signal to Noise Ratio
SWIR	Short-Wave InfraRed
TANSO	Thermal And Near infrared Sensor for carbon Observation
Tau_ref	Parameter for the aerosol optical thickness
TCCON	Total Carbon Column Observing Network
TIR	Thermal InfraRed
TOA	Top-Of-Atmosphere
TROPOMI	TROPOspheric Monitoring Instrument
UNFCCC	United Nations Framework Convention on Climate Change
UV	UltraViolet radiation
XCO_2	retrieved Carbon dioxide
XCO_4	retrieved Methane

List of Figures

List of Tables

1 Introduction

Over the last decades climate observations show an increase of the global land and sea surface temperature. There is scientific consensus that the primary cause of global warming is the increase in anthropogenic greenhouse gas (GHG) emissions since (IPCC, 2021). Carbon dioxide (CO_2) and Methane (CH_4), being two of the most important GHG's, have been classified as Essential Climate Variables (ECVs) by the Global Climate Observing System (GCOS). Since the industrial revolution CO_2 concentrations in the atmosphere increased rapidly to 414.7 parts per million (ppm) in 2021 mainly by burning fossil fuels (NOAA, 2022b). According to climate models this human induced climate change is expected to cause a further increase in air and sea surface temperature. This is accompanied by unpredictable consequences, for instance extreme weather events, sea level rise, droughts or a decrease in snow and ice cover (IPCC, 2021; Reuter et al., 2020). These consequences can limit habitats for animals and humans, leading to losses in biodiversity and can expose humankind to different health risks (Román-Palacios & Wiens, 2020).

Since the Kyoto Protocol, which became effective in 2005, countries must report their GHG emissions to the United Nations Framework Convention on Climate Change (UNFCCC). Furthermore, in the Paris agreement from 2015 195 countries and the European Union (EU) committed themselves to limit global temperature increase less than 2°C. However, independent monitoring and verification for these reported emissions is still rare. Methods for verification are mostly based on inverse modelling of measured GHG concentrations but due to a lack of observations not globally possible (Bovensmann et al., 2010; Nassar et al., 2017). Missing data and thus inefficient models are improved by the use of satellite data, which is able to observe also remote regions with a greater coverage. Furthermore, verification from industries reported emissions can be ensured by measurements of GHG emissions from satellite missions. Since the end of 2016 data about GHG emissions is available from the Copernicus Climate Change Service (C3S) on the Copernicus Climate Data Store (CDS) as an independent tool to verify reported emissions. However, already existing, and future missions with global coverage, such as the CO2M mission - one of Europe's Copernicus Sentinel Expansion - are only able to record the largest of GHG emissions. Yet, point sources such as power plants and

industrial facilities account for a large share of global CO_2 and CH_4 emissions, which are the cause for increasing temperatures due to radiative forcing (IPCC, 2014)[1].

Besides these largest GHG emissions (>10 megatons (Mt) CO2 year-1), detectable by existing satellite projects, large and medium-sized point sources are responsible for around 88% of the global CO_2 emissions (Strandgren et al., 2020). With the new CO2Image mission the German Aerospace Center (DLR) is planning to observe specifically medium-sized point sources, emitting 1-10 Mt CO_2 $year^{-1}$. The satellite instrument of the CO2Image mission, called COSIS will observe an area of 50 x 50 km² with a ground resolution of 50 x 50 m^2. In this spatial resolution CO_2 and CH_4 plumes from sources with medium and high emission rates can be monitored and allow the determination of actual emissions. COSIS will measure the backscattered solar radiation in the shortwave infrared (SWIR) spectrum. From the measured spectrum the GHG emissions can be retrieved.

Nevertheless, environmental parameters, like clouds, aerosols or heterogenic surface are influencing and modifying the measured solar radiation, which makes the observation GHG emissions from space a challenging issue. Therefore, this thesis aims to find out the influence of environmental parameters on quantifying CO_2 and CH_4 emissions in the DLR satellite mission CO2Image on basis of light scattering through aerosols in the atmosphere and surface albedo. For this purpose, simulations of emission plumes from a satellite perspective were carried out by the retrieval algorithm RemoTeC on the supercomputer “Levante” of the German Climate Computer Center (Deutsches Klimarechenzentrum, DKRZ).

1.1 Interest of using satellite data

Current estimates of sources and sinks of GHG emissions by inverse models are mostly based on measurements close to the surface. Predominantly, this ground-based measurements are based on continuous in-situ measurements, flask samples, towers, and ships and flight campaigns (Guerlet et al., 2013). Ground-based measurement networks, such

[1] The total radiative forcing due to well-mixed greenhouse gases is 2.83W*m^{-2}, of which CO_2 alone makes up 1.82W*m^{-2}, making it the greenhouse gas with the largest anthropogenic contribution to global warming IPCC (2014).

as the Total Carbon Column Observing Network (TCCON), have been built to provide long-term records worldwide and have been used for various validations (Wu et al., 2018; Wunch et al., 2017; Zhou et al., 2016).

Figure 1.1 shows the worldwide stations of TCCON, a network of ground-based Fourier Transform Spectrometers recording direct solar spectra in the near-infrared spectral region. From these spectra column-averaged abundance of CO_2, CH_4, N_2O, HF, CO, H_2O, and HDO can be retrieved. These data provide a validation source for different satellite missions like OCO-2 (Orbiting Carbon Observatory-2), GOSAT (Greenhouse Gases Observing Satellites), TROPOMI on Sentinel 5P and other missions (Wunch et al., 2011). Ground-based networks like TCCON can provide accurate and precise data but are lacking global coverage as there are many areas with few or no stations.

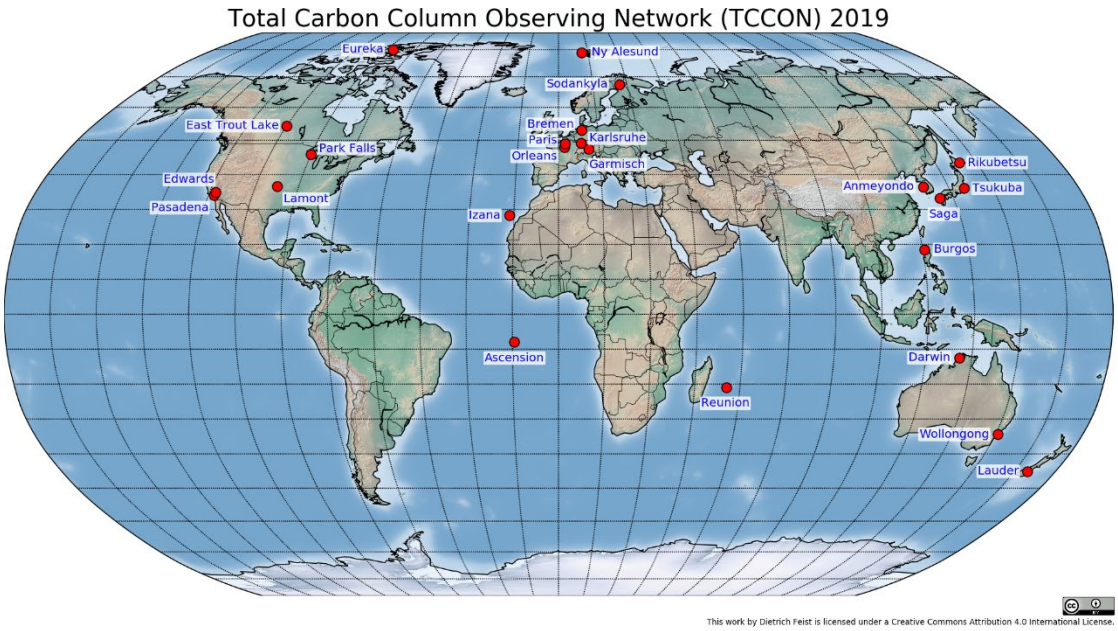

Figure 1.1: TCCON site map (MPI, 2022).

Additionally, ground-based measurements providing surface concentration data, are sensitive to the description of boundary layer height and vertical mixing in transport models. Furthermore, these measurements are influenced by local and large-scale fluxes, making the interpretation of these data complex (Guerlet et al., 2013). Because of their high observation density and global coverage, satellite observations, if accurate enough, have the ability to provide data about GHG total columns and could therefore reduce

uncertainties in sources and sinks characterization (Guerlet et al., 2013; Miller & Michalak, 2017). Although data density of satellite measurements is supposed to be much higher than of in-situ measurements, the retrieved abundances of GHG are expected to have a lower precision and accuracy as the measurement and retrieval itself is a lot more complex.

To comply with the demands of climate policy and be able to report emissions to the UNFCCC, as each country is obliged to on a yearly basis since the Kyoto protocol and the Paris agreement, better global quantification of GHG emissions is necessary (Jacob et al., 2022; Nassar et al., 2017).

Currently the global and continuous monitoring of GHG emissions is only possible with the help of Earth observation satellites such as those operated by the European Space Agency (ESA) and EUMETSAT within the Copernicus program (includes the future CO2M mission). However, due to the different observation concepts studies show that CO2M can only detect and quantify sources bigger than 10 Mt CO_2 per year (Kuhlmann et al., 2021). The International Energy Agency (IEA) reported that emissions from coal-fired power plants in 2018 exceeded 10 Gt CO_2 per year, constituting approximately 30% of the global CO_2 emissions (IEA, 2019). The majority of these emissions (approx. 88%) originate from sources with medium and high emission rates (>1 Mt CO_2 per year) which thus contribute significantly to the global CO_2 budget (Strandgren et al., 2020). Current satellite mission, having at best a spatial resolution of 2 x 2 km^2 are consequently not able to quantify most of the CO_2 emissions, coming from point sources. Thus, a higher spatial resolution satellite mission like the CO2Image mission of the DLR is needed.

1.2 Research objectives

This work aims to ascertain the influence of environmental parameters on the quantification of CO_2 and CH_4 emissions of point sources by the future satellite project CO2Image of DLR. CO2Image is a project which will significantly help to provide independent verification of reported emissions from industry. This will be a great contribution in mitigating the global climate crisis.

This thesis examinates the impact of scattering through aerosols on the reflected solar radiation in the SWIR spectrum, which is measured by the CO2Image instrument. To achieve this goal, the full physics algorithm RemoTeC is used for simulations of CO_2 plumes. Thereby, studies including varying values for the parameters of aerosol amount, aerosol height distribution and aerosol size distribution are performed to investigate the influence of every individual parameter.

In the implementation of these aerosol studies the focus of this work lies on investigating the following hypotheses:

1. Due to aerosol scattering depending on three parameters: aerosol amount, aerosol size distribution and aerosol height distribution errors in the quantification of CO_2 can occur. It can be assumed, that:
    - with increasing aerosol amounts, the measured light path gets shortened and CO_2 values will be underestimated.
    - the higher the aerosol abundance in the atmosphere, the more the measured light path gets shortened and CO_2 values will be underestimated.
    - with increasing aerosol sizes, the measured light path gets shortened and CO_2 values will be underestimated.

2. Scattering through aerosols can be neglected in the CO2Image mission of the DLR, as it is the same amount in and outside the plume and the satellites instrument is detecting the “signal to noise” ratio

3. Pixels in the simulations with dark surfaces, having low albedo values, will cause more errors and causing challenges in the retrieval. Furthermore, low albedo values are assumed to amplify effects due to aerosol scattering.

1.3 Outline of this thesis

The following work is structured in one part about the theoretical background (chapter 0), giving an overview on the Earth atmosphere radiation budget and greenhouse gases in general. Followed by a general description about observations of greenhouse gases in

atmospheric science and different approaches. Chapter 3 gives an overview of existing satellite projects, which monitor CO_2 and CH_4 emissions. DLR's future CO2Image satellite mission is presented in chapter 0. Chapter 5 describes the methods used in this thesis to estimate GHG emissions with the full physics algorithm Remote C and the analysis methods. Chapter 0 presents the results on studying the influence of environmental parameters on the quantification of greenhouse gas emissions from point sources in the future DLR satellite project CO2Image. The results are discussed in chapter 0. Following this chapter 8 contains the summary and conclusion. This thesis ends with an outlook in chapter 0. Due the fact that during this thesis supercomputer on DKRZ changed from "Mistral" to its successor "Levante" in May 2022 one of the challenges was to get the algorithm running properly again. Therefore, there is one chapter describing these challenges and necessary steps to solve the problems in the appendix A.

2 Theoretical background

A tool, independent from the GHG emitting industries, to estimate GHG emission is crucial in mitigating the global climate crisis. In principle it is possible to measure atmospheric concentrations by remote sensing (RS). Especially satellites providing a global coverage can be a valuable tool in monitoring GHGs. This chapter describes the theoretical background of the physical description of Earth's atmosphere. The focus lies on solar radiation, since it is the source of the measured radiation of the CO2Image instrument. Moreover, the constituents of the atmosphere are described and the contribution of CO_2 and CH_4 to anthropogenic climate change is explained. Chapter 2.2 explains the methods of RS of GHG's and different approaches in their observation.

2.1 Earth's atmosphere and energy budget

The following chapter, which provides an overview of the Earth's energy budget, is based on Petty (2006), unless otherwise noted.

Earths energy budget causes heating or cooling of the atmosphere and is influencing the weather and climate. The incoming short-wave electromagnetic radiation originates from the sun and is therefore referred to as solar radiation. This incoming solar radiation is either directly reflected to space or absorbed and emitted as long-wave thermal radiation. As atmospheric radiation operates continuously over long distances throughout the atmosphere it complicates the weather prediction and climate models.

Figure 2.1 shows the components of the energy budget expressed as percentages of the incoming solar radiation. 70% of the incoming solar radiation is absorbed by land and ocean surfaces (51%) as well as the atmosphere, clouds included (19%). The absorbed energy is either directly emitted back to space and lost for the Earth's energy budget or transferred to the atmosphere. The energy which is staying in the atmosphere is the latent heat of vaporization, transported by the evaporation of water, conduction of sensible heat, the emission and reabsorption of radiation. The absorption of solar radiation by the atmosphere and the Earth's surface assures the atmosphere average temperature and its structure including the horizontal gradients that drive atmospheric circulations. The remaining 30% of the incoming solar radiation is backscattered to space by the surface,

clouds, or the atmosphere itself. This reflected solar radiation is then measured by the CO2Image instrument to determine GHG emissions.

The following chapter explains the source of the measured radiation. Furthermore, the constitutes of the atmosphere as well as the role and interactions of CO_2 and CH_4 are described in more detail. In Section 2.1.3 the contribution of CO_2 and CH_4 to anthropogenic climate change is explained.

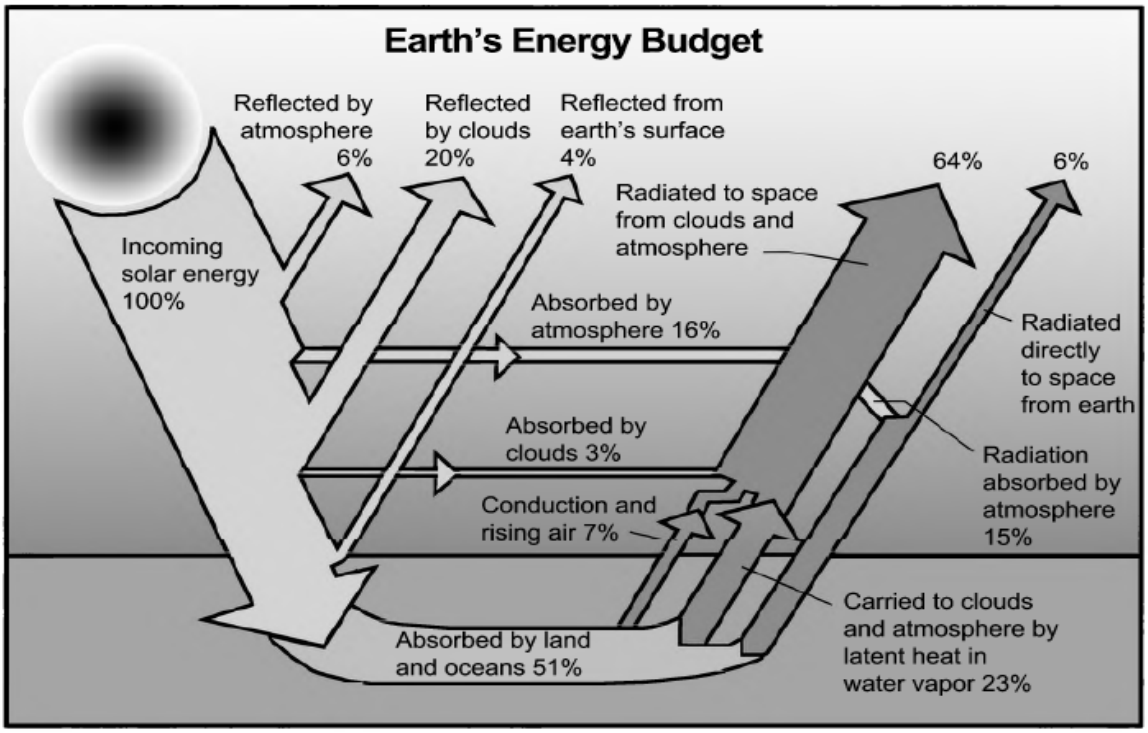

Figure 2.1: The global Earth's energy budget with the individual components expressed as percentages of the incoming solar radiation. Light arrows depict the shortwave radiation and dark arrows show the long-wave thermal radiation. Redrafted from an illustration by J.T. Kiehl and Kevin E. Trensberth. Taken from Petty (2006).

2.1.1 Solar radiation

Atmospheric radiation, visible and invisible, originates from the sun and is referred to as solar radiation.

The solar radiation, invisible to human eye, arrives in form of infrared (IR) or ultraviolet (UV) radiation. This solar radiation is the source of the measured radiation of many satellite projects. In the proposed satellite mission CO2Image the instrument on board of the satellite will measure backscattered light in the SWIR range. The solar

radiation can be described as photons travelling through the atmosphere. Whereby the flow of these group of photons is defined as the radiative transfer. The radiant flux Φ is defined as:

$$\Phi = \frac{\delta Q}{\delta t} \tag{2.1}$$

as Q being the sum of all photon's energy over one unit of time t.
The radiant flux received by a unit area A for a given frequency ν is the spectral irradiance E_ν.

$$E_\nu = \frac{\delta \Phi}{\delta A \delta \nu} \tag{2.2}$$

2.1.2 Structure and constitution of the atmosphere

The Earth's atmosphere is divided in several layers depending on the temperature profile. The density of the atmosphere decreases by increasing altitude, due to the gravity of the Earth. Figure 2.2 visualizes the structure of the atmosphere, giving information about the layers, their extent, and temperature profile, as well as additional information about the phenomena in the layers like weather or polar mesospheric clouds. The layer closest to the surface is called troposphere and extends approximately to the height of 15 km. Here occur different processes and climatic phenomena which are commonly known as weather. Typical for this layer, humankind lives in, is the vertical temperature profile, whereby the temperature decreases with increasing altitude. The troposphere is separated from the second layer, the stratosphere, by the tropopause. In the stratosphere heavier cold air lays below the warm air as there is no turbulence present. The ozone layer, which protects life on Earth from the UV radiation of the sun, is located in the stratosphere. The layer between the stratosphere and the thermosphere is the mesosphere. Separated from the mesosphere by the mesopause, the thermosphere extends to a height between 500 to 900 km. Here low Earth orbit (LEO) satellites are present.

The atmosphere, reaching an extent of approximately 900 km, consists of water vapor, aerosols (e.g. dust and sea salt) and different composition of gases. There is a mixture of gases which are constantly consisting of molecular nitrogen (N_2) (~78 %), molecular oxygen (O_2) (~21 %), and the noble gas Argon (~1%). Also, there are gases with variable amounts like the carbon compounds CO_2 and CH_4, which have a great impact on atmospheric processes and therefore climate change.

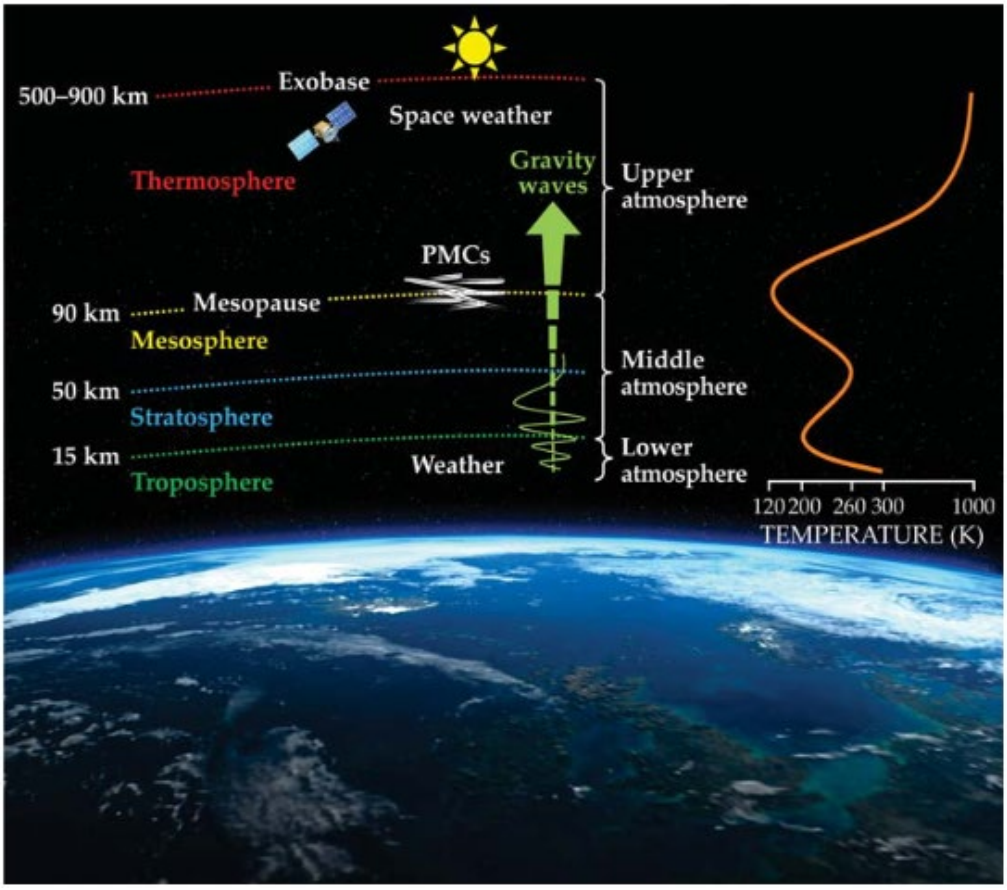

Figure 2.2: The vertical structure of the atmosphere including lower, middle and upper atmosphere. Taken from Yiğit and Medvedev (2019).

2.1.3 Contribution of CO_2 and CH_4 to climate change

The understanding of the carbon cycle has become essential as a major part of the anthropogenic global warming is attributed to the increase of the carbon compounds CO_2 and CH_4 since the industrial revolution. In order to predict future changes in the carbon cycle and related changes in climate the understanding and quantification of carbon fluxes, as well as their natural and anthropogenic sources and sinks, are crucial. Further information about the carbon cycle and measuring carbon fluxes can be found in Grace (2004) and Prentice et al. (2001).

Figure 2.3 shows the CH_4 budget with the main natural sources coming from freshwaters, wetlands, and geological sources. Future uncertainties lie in the impact of global warming on CH_4 stocks like permafrost and the ocean. The main anthropogenic

sources of CH_4 are fossil fuels, landfills and agriculture including livestock and rice cultivation.

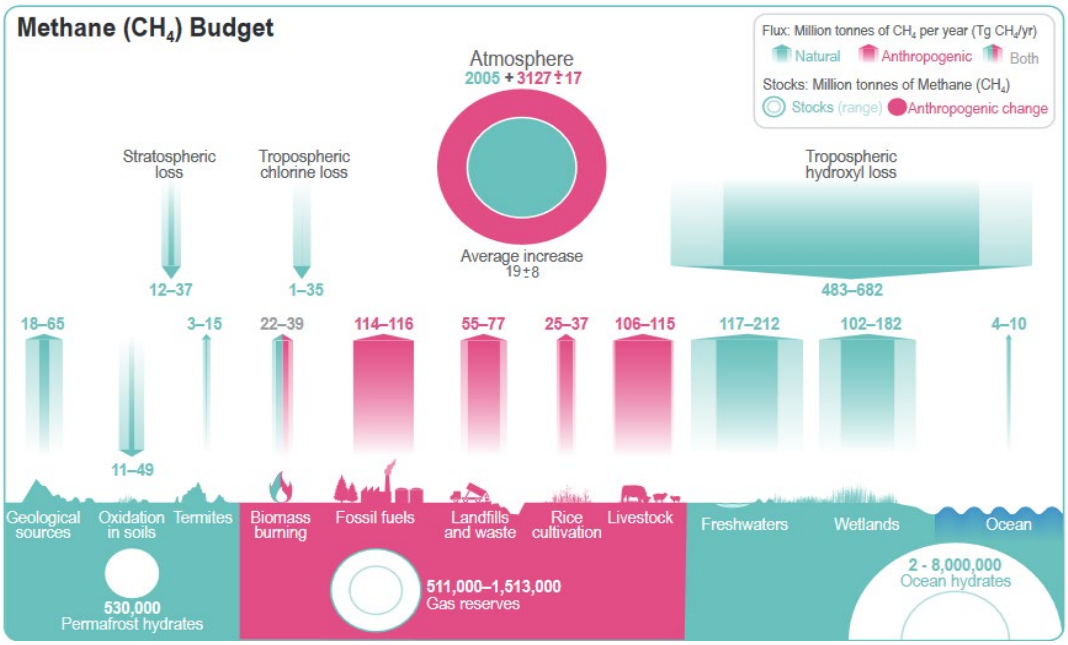

Figure 2.3 Global CH4 budget from 2008 until 2017 (IPCC, 2021). The arrows in red mark the anthropogenic emissions, while the green arrows show the natural emissions. The emissions are presented as fluxes in million tons CH4 per year. The bottom bar shows the current stock of CH4 in million tons by individual source.

Natural sources of CO_2 are the ocean to atmosphere exchange, plant and animal respiration, as well as soil respiration, decomposition and volcanic eruptions. However, the natural sources and sinks of CO_2 are in equilibrium or fluctuating within a natural range and are not responsible for the recent global warming. The main anthropogenic sources are related to burning fossil fuels and land cover change (IPCC, 2022; Oda et al., 2018). Over 60% of the global GHG emissions are coming from fossil fuels and industry emitting CO_2 (Boden et al., 2017; EPA, 2016; IPCC, 2022). Figure 2.4 shows the global net anthropogenic GHG emissions with the proportions of the major groups of sources. The atmospheric concentration of CO_2 increased by more than 30% since the industrial revolution and is continuously rising since 1900 (Bovensmann et al., 2010; Canadell et al., 2007; IPCC, 2022). Because of the increasing amount and their role as strong GHG, CO_2 and CH_4 have contributed 1.0°C through CO_2 to global warming since pre-industrial time and 0.6°C through CH_4 (Boden et al., 2017; IPCC, 2021) . Power plants, especially coal-fired power plants, are among the largest CO_2 emitters (Bovensmann et al., 2010;

EPA, 2016). The satellite mission CO2Image aims to detect and quantify CO_2 and CH_4 point sources like these power plants.

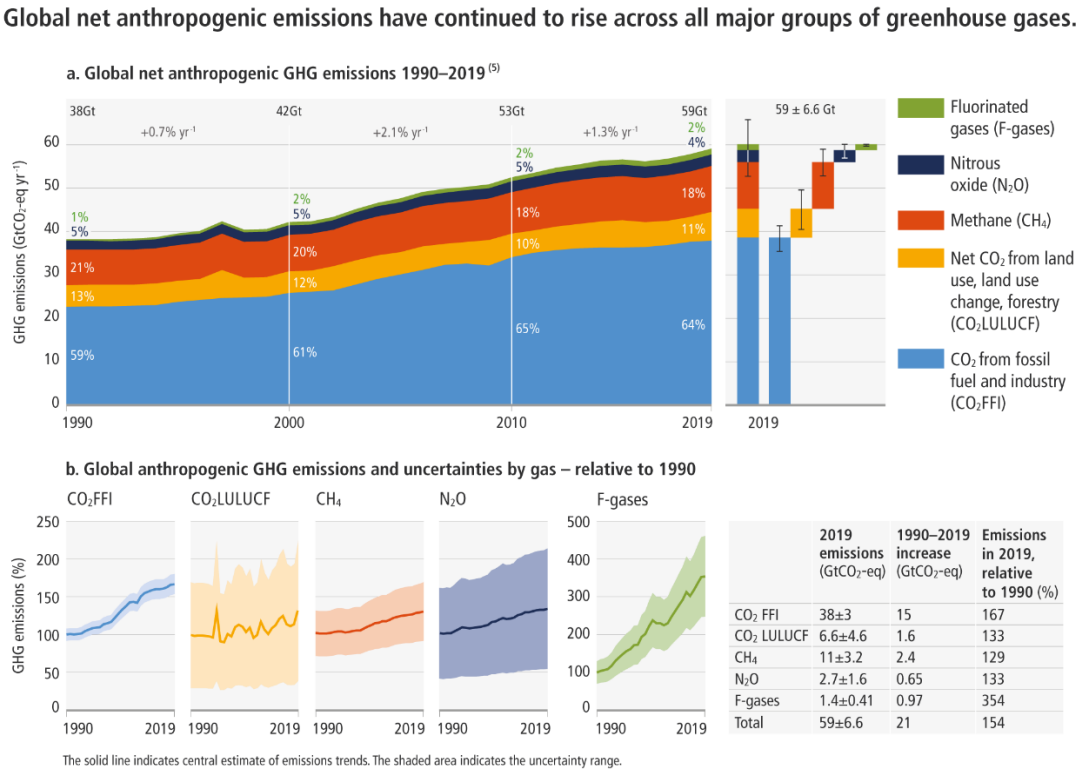

Figure 2.4: Global net anthropogenic GHG emissions. (a) Global net anthropogenic GHG emissions in the period from 1990 until 2019. The rise of GHG is separated across the major gases: CO_2, CH_4, N_2O and fluorinated gases. CO_2 is separated into CO_2 coming from fossil fuels or industry (CO_2FFI) and CO_2 coming from land use, its changes and forestry. (b) shows the increase in global anthropogenic GHG emissions with uncertainties by gas since 1990. Taken from IPCC (2022).

2.2 Observations of greenhouse gas emissions

RS is one possibility to monitor GHG's. While in-situ measurements sample directly at the point of interest, RS methods rely on reflected signals and measure from distance. Hence, RS can provide a broad spatial coverage of data. It is differentiated into active and passive RS sensors. Active RS systems emit waves or pulses themselves and therefore have their own light or illumination source. Common examples for active sensors are radar (RADAR) or LIght Detection And Ranging (LIDAR) systems. These sensors send out a pulse and the backscattered pulse is measured by the sensor. Passive sensors rely on

direct or indirect sunlight. Thus, they can only measure during daylight, when they can detect the solar radiance reflected from the Earth's surface.

RS data is either space-based retrieved from satellite measurements, airborne related to aircrafts and balloons (airborne), or from ground-based measurements. Ground based measurements monitor local emissions and meteorological processes. Yet, as permanent measurement stations are spread infrequently, ground-based measurements are limited to local sources and processes and not representative for large regions. Airborne RS is spatially and temporally flexible and thereby covering horizontal and vertical domains. Nevertheless, global coverage is currently not accomplished since measurements by aircrafts or balloons are expensive and complex. This work is based on spaceborne measurements. Although globally coverage is mostly given, satellite observations provide column-averaged mole fractions (see chapter 2.2.2). The column-average mole fraction does not provide information on the vertical distribution of GHGs.

The satellite mission of this work aims to quantify CO_2 and CH_4 emissions from point sources. For this purpose, sunlight backscattered by the Earth's surface and atmosphere in the SWIR spectral range is measured by spectroscopic instruments (Butz et al., 2012). The absorption spectra for CO_2 and CH_4 in the light reflection signal is used to quantify concentrations.

The following chapter 2.2.1 gives detailed information about the two approaches of observing GHG - the bottom up and top-down approach. In addition, chapter 2.2.2 explains the dry air mole fraction in which satellite measurements are typically reported, followed by the CO_2 and CH_4 absorption and emission characteristics (chapter 2.2.3).

2.2.1 Bottom-up vs. top-down

There are two different approaches to observe GHG emissions. The bottom-up approach uses statistical activity data whereas the top-down approach is based on independent GHG measurements in the atmosphere. More precisely, the bottom-up approach begins with the release of GH, while the top-down approach aims to quantify fluxes and the impact of GHG on the atmosphere. Both approaches have different advantages and disadvantages.

The bottom-up approach starts with an analysis of processes of release of emissions and absorption, whereby emissions can be calculated sector wise, globally, or from single emitters. Hence, it also includes information about emission processes. If the interactions and dynamics of ecological processes are known on a statistical level, ecosystem models, aiming to understand and predict carbon fluxes can be developed. Therefore, the bottom-up approach can be used to conclude carbon fluxes, even if interactions are dynamic and complex. Especially at large scales it is difficult to rebuild the interaction of the processes completely, which is called the "upscaling problem" of ecosystem modelling. However, the bottom-up approach suffers from uncertainties in the boundary conditions in ecosystem modelling like ecosystem response on water or nutrient limitation or temperature sensitivity of plants or soil respiration.

The top-down approach enables modelling to use atmospheric measurements from RS instruments on satellites or aircrafts as an independent quantification with high spatial and temporal resolution of reported emissions. Accordingly, these measurements can be used to validate bottom-up emissions and control emission reports independently (Nisbet & Weiss, 2010). Furthermore, the top-down approach improves the understanding of processes involved in the carbon cycle. Starting from the impact of GHG on the atmosphere the top-down approach has the goal to monitor GHG emissions. With the aid of inversive atmospheric transport models the measured abundance of GHG is traced back to the source (Corazza et al., 2011; Hirsch et al., 2006; Houweling et al., 2017).

The main problem of the top-down approach is the lack of adequate knowledge of meteorological conditions like wind and emerging turbulence. Uncertainties of transport models are one reason for mostly failing the goal of more accurate predictions. Another problem is related to low data density. This is further reinforced as sources of emissions are often collocated and thus difficult to measure as high spatial resolution is needed. In addition, measurements from airborne or ground based stations are limited in temporal and mainly spatial coverage. Except of extending intensive aircraft measurements, satellite measurements are supposed to help facing this problem and to provide a higher data density in the future (Miller & Michalak, 2017).

2.2.2 Dry air mole fraction

Satellite measurements are typically reported as column-averaged dry air mole fraction. Thus, the information on the vertical distribution of GHG's is missing. However, using the column-averaged dry air mole fraction avoids the variability through surface pressure (Jacob et al., 2022). Additionally, using the dry air, instead of the total air, removes the dependency on water vapor.

The column-averaged dry air mole fraction X_i is

$$X_i = \frac{\Omega_i}{\Omega_{a,d}} \tag{2.3}$$

where Ω_i is the total atmospheric column of the traced gas i and $\Omega_{a,d}$ is the dry air column with both in the unit molecules per cm^2. It is optimal for the quantification of the length of the light path as this ratio is considered to be constant in time and space.

The retrieval algorithm used in this work, RemoTeC (described in chapter 5) retrieves the column-averaged dry air mole fraction for CO_2 (XCO_2) for each spatial pixel with the associated retrieval error.

2.2.3 CO_2 and CH_4 absorption and emission

This chapter is based on Petty (2006).

In a cloud-free atmosphere the transmittance is primarily controlled by absorption of the incoming short-wave radiation through different constituent gases. The constituent gases of the air in the troposphere and stratosphere are N_2 and O_2, which make up 99% of the total mass of the atmosphere. Furthermore, CO_2, CH_4 and ozone (O_3) and many other gases occur in trace amounts. Even if these gases are a small fraction of the total air mass, they can have a large impact on atmospheric transmission.

The transmittance T_λ of the atmosphere is defined by

$$T_\lambda = \frac{L_\lambda^\downarrow (z=0)}{L_\lambda^\downarrow (z=TOA)} \tag{2.4}$$

with the downwelling radiation $L_\lambda^\downarrow$ at height z, the top of atmosphere (TOA) and the downwelling radiation at the surface ($z = 0$).

In the short visible range and UV wavelength, scattering by molecules of the air also needs to be considered. As the satellite mission CO2Image works with sensors in the SWIR, the scattering by molecules is not described further. Transmittance of nearly 100% can be reached if there is no or weak absorption. On the contrary, if absorption due to gases is strong, the transmittance is small. Figure 2.5 shows the vertical transmittance of an aerosol and cloud free atmosphere as function of the wavelength. It also shows the absorption wavelength of individual gases. The gases, important for this study are CO_2 and CH_4 - have significant absorption bands near 2.8, 4.3, and 15 micrometer (μm) for CO_2 and absorption bands near 1.6, 3.3 and 7.8 μm for CH_4.

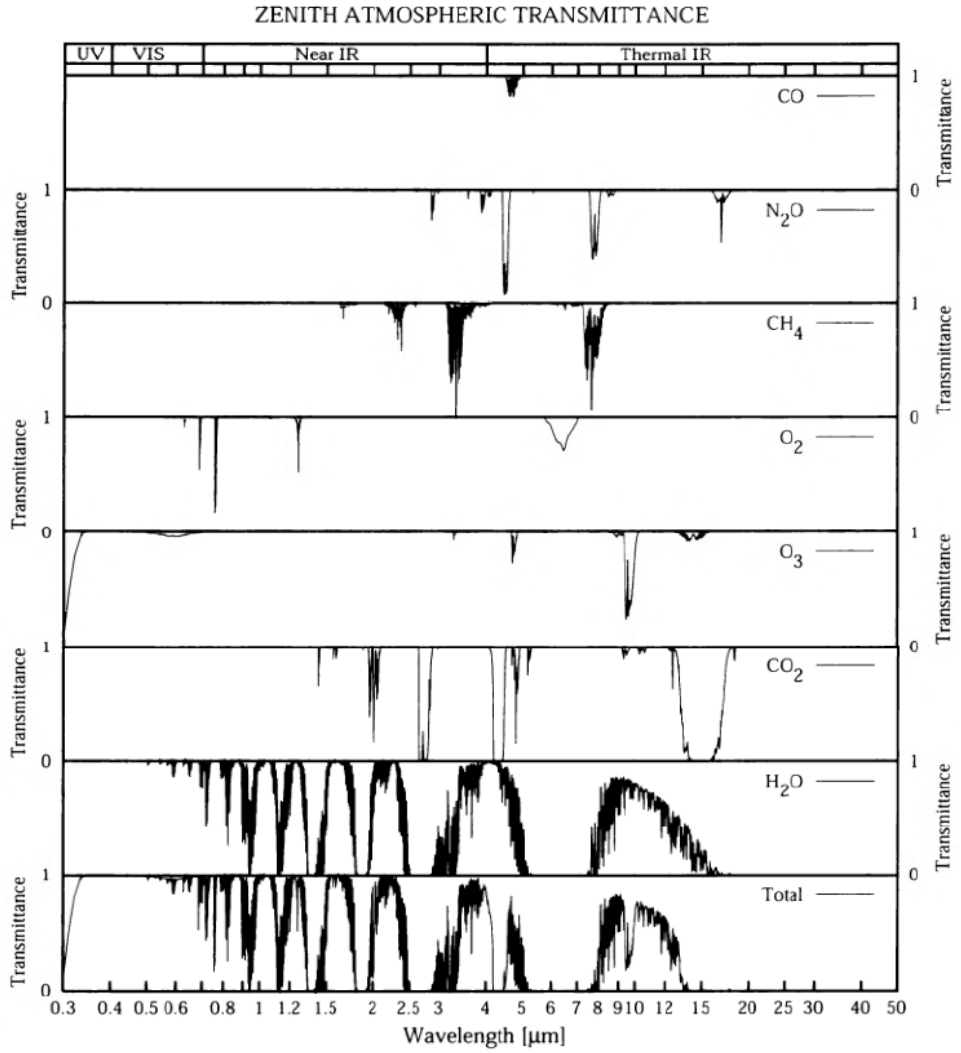

Figure 2.5: Zenith transmittance for a cloud and aerosol-free atmosphere , with typical conditions for a midlatitude summertime atmosphere. Each panel shows the wavelength of the absorption of one individual constituent atmospheric gas. The bottom panel displays the effect of absorption when all constitutes are considered. The plots do not take molecular scattering into account, which is important for wavelengths under 0.5 μm. Taken from Petty (2006).

3 Satellite projects observing CO_2 and CH_4: State of the art

Due to the importance of CO_2 and CH_4 for the current climate change, there are already different satellite projects observing CO_2 and CH_4 emissions from space. Since the start of SCIAMAHY on Envisat in 2003 global observations from space of tropospheric CO_2 and CH_4 were regularly implemented (Frankenberg, Platt, & Wagner, 2005).

Satellite missions, that observe greenhouse gases, can be classified by their onboard instruments as point source imagers and area flux mappers. Fine pixel instruments (<60 m) which are used to quantify individual point sources are called point source imagers. These instruments focus specifically on point sources to image the single plume. Area flux mappers on the other hand are high-precision (<1%) instruments with a pixel size of 0.1-10 km and used to quantify total GHG emissions on a regional to global scale (Jacob et al., 2022). Figure 3.1 gives an overview of existing satellite missions observing CH_4. These missions are divided into area flux mappers and point source imagers. Using Figure 3.1 and the in Jacob et al. (2022) presented missions to observe CH_4 as base, this chapter evaluates these missions regarding to their possibility to additionally monitor CO_2. Furthermore, promising missions to observe CH_4 and CO_2 are presented in the following chapter, separated into area flux mappers and point source imagers.

Table 3.1 summarizes an overview of area flux mappers observing atmospheric CH_4 and their technical details like launch, coverage, pixel size, spectral resolution, return time, and absorption bands. Meanwhile Table 3.2 presents the point source imagers. Both tables are based on Jacob et al. (2022) with specified references to the individual missions. The tables are extended with additional information and missions, which may have the possibility to also observe CO_2. All missions presented in Table 3.1 and Table 3.2 have instruments observing CH_4 and CO_2 in SWIR, fly in a LEO and observe globally at a specific local time of day. Mostly the observation time is in the morning or early afternoon, as mornings have a greater probability of a clear sky while early afternoon has steadier boundary layer winds for interpreting methane enhancements (Jacob et al., 2022). Table 3.2 does not take instruments into account that measure methane in the thermal infrared (TIR), as instruments in the TIR spectrum are not sensitive to methane close to the surface (Jacob et al., 2022). Therefore, these instruments are not suitable for quantifying methane emissions.

The following presents more in detail which satellite missions have a global coverage and the possibility to quantify emission plumes of CH_4, as well as CO_2 of point sources.

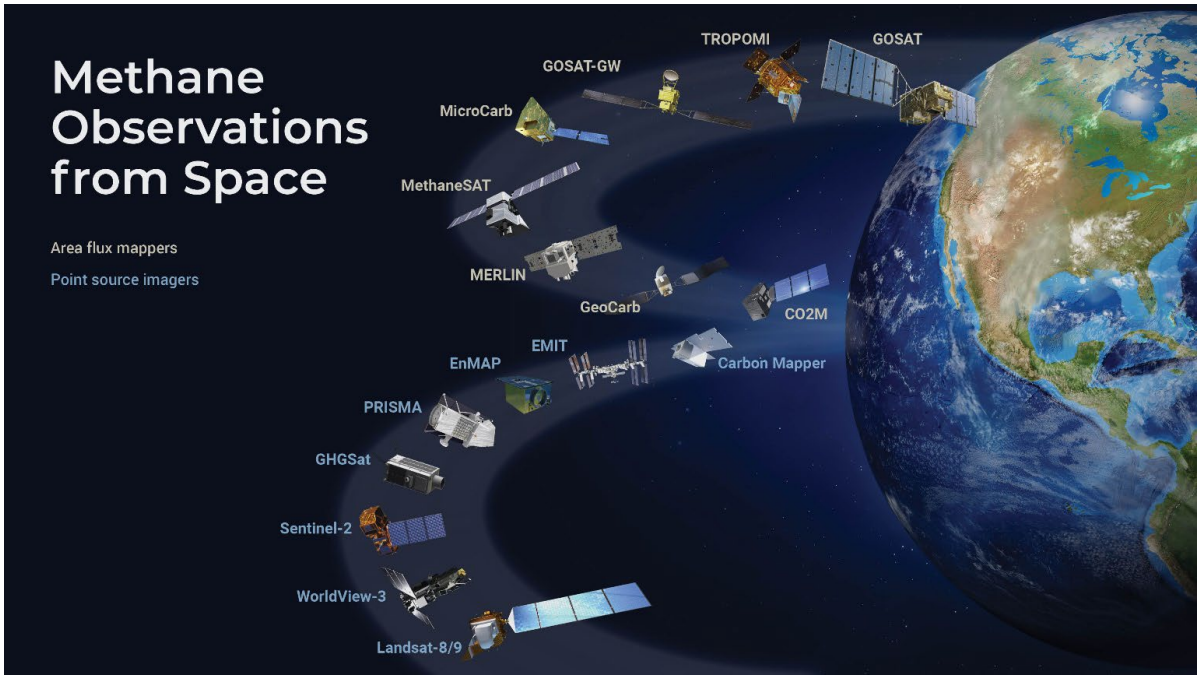

Figure 3.1: Overview of Methane Observation satellite projects. The different satellite missions are divided in area flux mappers and point source imagers after Jacob et al. (2022).

Table 3.1: Area flux mappers: Overview of Satellite Projects observing atmospheric CO2 and CH4 supplemented and extended according to Jacob et al. (2022)

	Company/ Agency	**Launch**	**Coverage**	**Pixel size**	**Spectral resolution [nm]**	**Return time [days]**	**Band (CH_4 or CO_2) [µm]**	**Precision**	**Reference**
SCIMACHY on ENVI-SAT	ESA	2002	±500 km	Limb vertical 3 x 132 km, Nadir horizontal 32 x 215 km	0.22-0.54	3	0.33 – 2.4 (CH_4 and CO_2)		Bovensmann et al. (1999); Frankenberg, Platt, and Wagner (2005)
TANSO on GOSAT	JAXA	2009	global	10-km diameter	0.06	3	0.65 (CH_4)	1-2ppm 0.7%	Kuze et al. (2016); Parker et al. (2020)
TROPOMI	ESA	2017	global	5.5×7 km^2	0.25	1	2.3 (CH_4)	~ 0.8%	Butz et al. (2012); Lorente et al. (2021)
OCO-2	NASA	2014	(≤10.3 km).	1.29 × 2.25 km^2		16	1.61 (CO_2) and 2.06	~1 ppm	Crisp et al. (2017); Nassar et al. (2017)
MicroCarb	CNES	2023	13.5×9 km2 targets	4.5×9 km^2	0.07	7	1.65 (CH_4 and weak CO_2) 2.04 (strong CO_2)	better 1ppm for CO_2 ~ 0.7%	Bertaux et al. (2020)
CO2M	ESA	2025	global	2 x2 km^2	0.3	28	1.65 (CH_4)	0.6%	Sierk et al. (2021)

Table 3.2: Point source imagers: Overview of Satellite Projects observing atmospheric CO2 and CH4 supplemented and extended according to Jacob et al. (2022)

	Company/ Agency	**Launch**	**Coverage**	**pixel**	**Spectral resolution [nm]**	**Return time [days]**	**Band CH_4 or CO_2 [µm]**	**precision**	**Reference**
Lansat-8	NASA	2013	global	30×30 m^2	200	16	2.3 (CH_4)	30-90%	Vermote et al. (2016)
WorldView-3	Digital-Globe	2014	66.5x112 km^2	3.7×3.7 m^2	50	<1	2.3 (CH_4)	6-19%	Sánchez-García et al. (2022)
Sentinel-2	ESA	2015	global	20×20 m^2	200	2-5	2.3 (CH_4)	30-90%	Varon et al. (2021)
GHGSat	GHGSat, Inc.	2016	12x12 km^2	25×25 m^2	0.3-0.7	1-4	1.65 (CH_4)	1.5%	Jervis et al. (2021)
PRISMA	ASI	2019	30x30 km^2	30×30 m^2	10	4	2.3 (CH_4)	3-9%	Guanter et al. (2022)
EnMAP	DLR	2022	30x30 km^2	30×30 m^2	10	4	2.3 (CH_4)	3-9%	Cusworth et al. (2019)
CarbonMapper	Carbon Mapper and Planet	2023	18-km swaths	30×30 m^2, 30×60 m^2	6	1-7	0.4 - 2.5 (CH_4 and CO_2)	1.2-1.5%	Cusworth et al. (2021); Duren et al. (2020)
CarbonSat	ESA	Not further implemented		2x2km^2				0.4 %	Buchwitz et al. (2013); Velazco et al. (2011)

3.1 Area flux mappers

Between 2002 and 2013 SCIAMAHY onboard Envisat provided the first global observations from space of tropospheric CO_2 and CH_4 (Bovensmann et al., 1999). This pioneer covers the wavelengths from 1–1.75 μm, 1.94–2.04 μm and 2.26–2.38 μm within three near infrared channels in moderate spectral resolution (Bovensmann et al., 1999). This range covers the absorption bands for the greenhouse gases CO_2, CH_4, N2O and H_2O as well as CO. However, CO_2 with absorption bands around 2,4 and 4,3 μm is at the edge of the range of SCIAMAHY and thus the detection and quantification of CO_2 emissions are hard. SCIAMAHY was followed by Japan's TANSO (Thermal And Near infrared Sensor for carbon Observation) on GOSAT in 2009 (Kuze et al., 2016). After a failed start of OCO in 2009, NASA's (National Aeronautics and Space Administration) OCO-2 was launched in 2014 (Crisp et al., 2017). Both satellites have high spectral resolution instruments measuring the reflected solar radiation at wavelengths around 0.76, 1.61, and 2.06 μm to derive CO_2 and CH_4 column-averaged dry air mole fractions (XCO_2 and XCH_4). They have the necessary precision, resolution, and coverage to better understand the surface CO_2 and CH_4 sources and sinks on regional scales (≥1000km). This knowledge helps to understand the processes which are controlling the variability of CO_2 and CH_4 sources and sinks over a seasonal cycle (Nassar et al., 2017).

Other current existing or planned flux mappers like TROPOMI, GOSAT-GW, MicroCarb, MethaneSAT, GeoCarb, and CO2M are increasing the potential to quantify emissions, starting from the source (Jacob et al., 2022). Out of all mentioned missions only MicroCarb, CO2M and OCO are capable to reliably detect CO_2 emissions. MicroCarb being focused on CO_2 emissions will measure atmospheric concentration of CO_2 globally with a high degree of precision (on the order of 1 ppm) and with a pixel size of 4.5 km (cross-track) x 9 km(along-track) (Jacob et al., 2022). OCO-2 aims primarily to provide data on natural CO_2 sources and sinks. Although CO_2 and CH_4 fluxes provide valuable information in understanding the carbon cycle, the existing satellite CO_2 sensors were not designed to monitor anthropogenic CO_2 emissions and are therefore limited in their help to mitigate the anthropogenic climate change (Bovensmann et al., 2010).

CO2M is planned to launch in 2025 and will then provide flux measurements with a spatial resolution of 2 x 2km (Sierk et al., 2021). However, individual plumes need to

be spatially separated from other emitters to have the ability to detect a single plume with a spatial resolution of 2 × 2 km^2 (Cusworth et al., 2021). In summary, the spatial scale of all area flux mappers is not high enough to measure single point emissions. Nonetheless, all mentioned missions provide information about CO_2 and CH_4 fluxes but are not able to detect and quantify point source emissions from anthropogenic sources like power-plants (Nassar et al., 2017). The next chapter screens if there are already point flux imagers which can quantify CO_2 emissions on high spatial resolution.

3.2 Point source imagers

Instruments classified as point source imagers aim to detect single point objects. Therefore, these instruments require a high spatial resolution. Landsat-8 and Sentinel-2 provide a global coverage with a spatial resolution of 30 x 30 m^2 and 20 x 20 m^2 while World-View-3 shows a coverage of 66.5 x 112 km^2 targets with a spatial resolution of 3.7 x 3.7 m^2. However, with 200 nm (Landsat-8 and Sentinel-2) and 50 nm (World View-3) their spectral resolution is not fine enough to trace atmospheric gases. Hence, these missions rather aim to detect land cover change and are not suitable to quantify CO_2 and CH_4 emissions from point sources. Besides the above mentioned hyperspectral and multispectral land imaging sensors, PRISMA is able to quantify large emission sources with a spectral resolution of 10nm while covering 30 x 30 km^2 targets with a spatial resolution of 30x30 m^2 (Cusworth et al., 2021). EnMAP, the first German-developed (DLR) hyperspectral satellite, was launched on 1st of April 2022 and covers 30 x 30 km^2 targets in 30 x 30 m^2 pixels every four days. With a spectral resolution of 10 nm EnMAP is able to give accurate ground measurements in high resolution. Having a spectral resolution of 10 nm EnMAP and PRISMA are still capable to extract CH_4 emissions, since the contrast in CH_4 measurements between background and the source is very high. This can be explained by the fact that in our atmosphere the CH_4 concentration is very low so the background noise to the CH_4 plume of a point source is weak. Yet, as CO_2 background noise is with over 400 ppm globally strong, it is not possible to quantify CO_2 emissions with a spectral resolution of 10 nm. GHGSat launched in 2016 is collecting data until now with a coverage of 12x12 km^2 targets in 25x25 m^2 pixel. It provides a fine spectral resolution of 0.3-0.7 nm but is missing the absorption band to detect CO_2 Except GHGSat all

mentioned point source imagers aim to observe land surfaces. Therefore, they have a fine spatial resolution (<50 m). However, to achieve this goal, it is not required to have a fine spectral resolution (Jacob et al., 2022). The Carbon Mapper project with a planned launch for the first two satellites in 2023 will have spectral resolution of 6 nm and with 1-7 days a frequent return time. High spatial coverage is ensured by 18-km swaths and 30x30 m2 pixels (Cusworth et al., 2021; Duren et al., 2020). Even though the spectral resolution of 6 nm increases the precision, the hyperspectral instrument will not be able to resolve surface structures and quantify CO_2 emissions of individual point sources.

As most of the mentioned missions are designed to detect land cover change, their spectral resolution is inadequate to quantify CH_4 and CO_2 plumes from individual power plants. ESA's approach of CarbonSat, the first mission with the precision, accuracy, spatial resolution, and coverage to quantify emissions from single point sources, was not implemented (Bovensmann et al., 2010; Buchwitz et al., 2013). With 2 × 3 km^2 pixels across an approximately 200 km wide swath and spectral bands following the model of OCO-2, CabonSat aimed to quantify CO_2 emission plumes with high precision. However, ESA selected to carry on with FLEX, a mission to reflect photosynthetic activity and therefore plant stress and health, instead of CarbonSat.

Therefore, the future satellite mission of the DLR CO2Image aims to have a spatial resolution of 50 x 50 m^2 to also be able to detect individual point sources, which will be a great contribution to mitigate anthropogenic climate change. From the presented satellite missions to observe GHG emissions it can be concluded that comparable global data products already exist for CH_4, but that there is a research gap in providing global data about CO_2 point source emissions. Independent verification of the reported emissions of each individual country to the UNFCCC will help to better quantify global CO_2 and CH_4 emissions and create strategies to mitigate the anthropogenic climate change.

4 DLR satellite mission CO2Image

Satellites are a strong tool to monitor greenhouse gas emissions continuously. Current missions to detect CO_2 and CH_4 emissions are described in the previous chapter. These missions are already contributing independent data about power plants, industrial facilities, and coal mines emissions, which emit large parts of the world's anthropogenic greenhouse gas emissions. Hence, satellite data has a big impact on the strategy of limiting global warming by the reduction of CO_2 and CH_4 emissions in order to diminish increasing temperatures. However, up to now the instruments of the mentioned satellite missions are not able to detect point sources smaller than 10 Mt per year. This is caused by a missing accuracy of the spatial resolution of the measuring instrument.

Consequently, the DLR designed the CO2Image mission to monitor and quantify also small point sources of CO_2 and CH_4 emissions with an extremely high spatial resolution (DLR, 2022). The goal is not only the monitoring of big sources but also the detection of 90% of the CO_2 and CH_4 point sources (Strandgren et al., 2020). The missions planning is still in progress, aiming to launch in 2026. Therefore, different simulations on the impact of instrument and environmental parameters are still proceeding. This is one important step for the validation of the later measured data of the CO2Image mission.

4.1 Goal and basics of the CO2Image mission

The goal of the CO2Image project is the quantification of CO_2 and CH_4 emissions from power plants, refineries, and other industrial facilities (so-called point sources). Point sources are responsible for a large percentage of anthropogenic CO_2 emissions (Hogue et al., 2016). Therefore, reducing uncertainties for quantifying emissions from point source is crucial to adjust strategies in reducing global fossil fuel CO_2 emissions (Turnbull et al., 2016; Varon et al., 2018). For the quantification of CO_2 and CH_4 emissions from space, CO_2 and CH_4 absorption lines will be measured in the SWIR as column concentrations of dry air (DLR, 2022). Figure 4.1 shows a map of the global power plant emissions rates in 2009, using the CARMA v3.0 database. The cumulative power plant CO_2 emissions reveal that just 24% of the total power plant CO_2 emissions come from sources with more than 10 Mt CO_2 per year. Only if a monitoring of medium-sized power plants with 1-10

Mt CO_2 per year is technical feasible, the detection of 88% of the global CO_2 emissions can be carried out (Strandgren et al., 2020). Hence, the CO2Image mission aims to be able to reliably quantify sources of up to >1Mt CO_2 per year on a global scale. This shall be ensured by a high spatial resolution. In general, a strongly reduced spectral resolution is used since absolute values are not necessary, but only the ratio between the background to the plume of CO_2 or CH_4 is measured ("signal to noise ratio", SNR). This allows the mission to be relatively inexpensive.

In summary, the objectives of the satellite mission CO2Image are:

- Measure (anthropogenic) CO_2 and CH_4 emissions from point sources up to >1Mt/year globally
- Verify industry data on their emissions (independent and neutral).
- Detection of unwanted emissions (pipeline leaks, etc)
- Satellite fleet (cheap and simple enough) better global coverage without losing high spatial resolution

As the primary goal of the CO2Image mission is monitoring CO_2, and CH_4 only comes as an intentional side effect, this master thesis focuses on CO_2. Therefore, all further descriptions and studies will only be referred to CO_2.

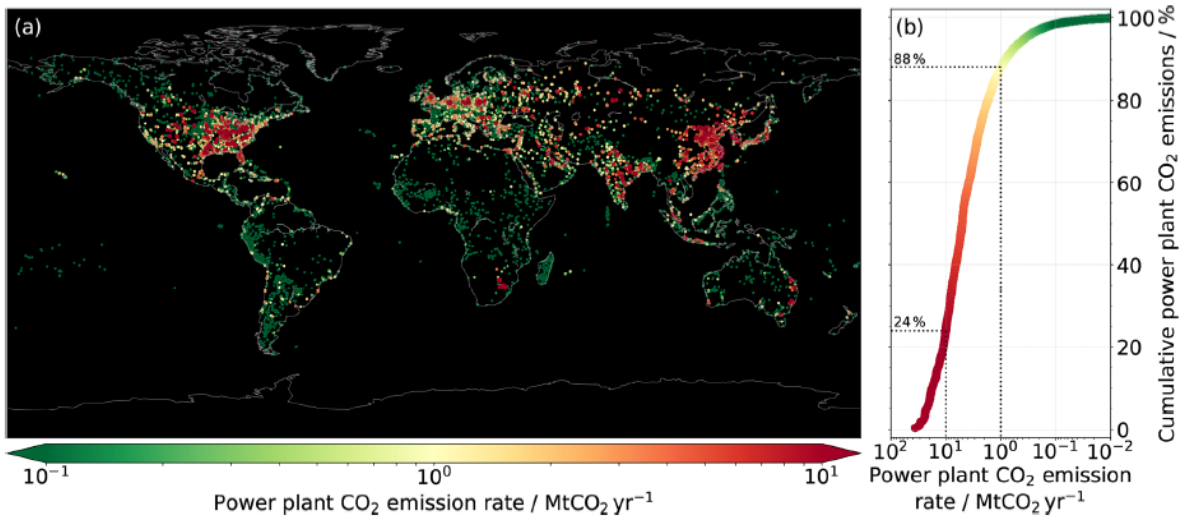

Figure 4.1: Geographical distribution of CO2 emissions from power plants in 2009 provided by the CARMA v3.0 database. (b) is the cumulative distribution, which shows the total power plant emission rates in Mt CO2 year-, with a total emission rate of 9.9 Gt CO2 year-1. Figure from Strandgren et al. (2020).

4.2 Satellite and his instruments

CO2Image will make passive CO_2 observations from space, measuring reflected solar radiation in the SWIR spectrum. Hereby, the focus is on the spectral window for CO_2 covering the weak and strong CO_2 absorption bands near 1600 and 2000 nm. CO2Image instrument, called COSIS, is built by the DLR from the intern Institute of Optical Sensor Systems (OS). COSIS is an imaging grating spectrometer, a RS technology that records multi-channel images, called hyperspectral images, which contain continuous spectra for each individual image element. Different studies with data from OCO-2 (Nassar et al., 2017; Reuter et al., 2019; Schwandner et al., 2017) demonstrated the use of imaging spectrometers to detect strong CO_2 plumes from natural and anthropogenic point sources. COSIS will provide data of the column-averaged dry-air mole fraction of CO_2 (see Chapter 2.2.2).

By following the previous mentioned goals, the CO2Image mission of the DLR stands out from other missions by its exceptional high spatial resolution of 50 x 50 m^2. Furthermore, the high spatial resolution is achieved through a global coverage to monitor single point source emissions. While most currently operating and planned missions (e.g. OCO-2 (Crisp et al., 2017), GOSAT (Kuze et al., 2016) , CO2M (Sierk et al., 2021)), rely on a high spectral resolution around 0.05-0.3 nm, CO2Image trades the high spectral resolution for an extremely high spatial resolution of 50 x 50 m^2. The lower spectral resolution is acceptable as CO2Image will not need absolute values but will work with the signal to noise ratio (SNR), where only background compared to plume concentration of CO_2 or CH_4 is used. Wilzewski et al. (2020) demonstrated the effect of a resolution of 50 x 50 m^2 compared to a 2 x 2km^2 resolution for a schematic Gaussian plume. Figure 4.2 follows this approach and shows the realistic impact of the higher spatial resolution of 50 x 50 m^2 of the CO2Image mission for two power plants in Germany compared to a 2 x 2km^2 spatial resolution like the CO2M mission of the Copernicus program. CO2M, implemented by ESA, EUMETSAT and ECMWF, with a planned start in 2026 will have highest spatial resolution for detecting CO_2 and CH_4 emissions by satellites on a global scale other than CO2Image. CO2M will have difficulties to quantify single point sources with SNR like CO2Image since the plume enhancement versus the background cannot be adequately separated in a spatial resolution of 2 x 2km^2. COSIS will be able to resolve emitters of down to 0.3 $MtCO_2\ yr^{-1}$. Additionally, when scattering is considered,

CO2Image aims to have an accuracy of most 4 ppm (approx. 1%) for two-thirds of the retrievals to be able to make quantifiable statements of the quantification of the CO_2 and CH_4 emissions on a local and regional level (Strandgren et al., 2020; Wilzewski et al., 2020). CO2Image will fly in a non sun-synchronous orbit to ensure a global coverage. To avoid scenes with clouds the equator crossing time will be in the morning at 10:30 local time with an integration time of 70 ms. Table 4.1 summarizes the technical parameters for the CO2Image mission compared to the planned Copernicus mission CO2M.

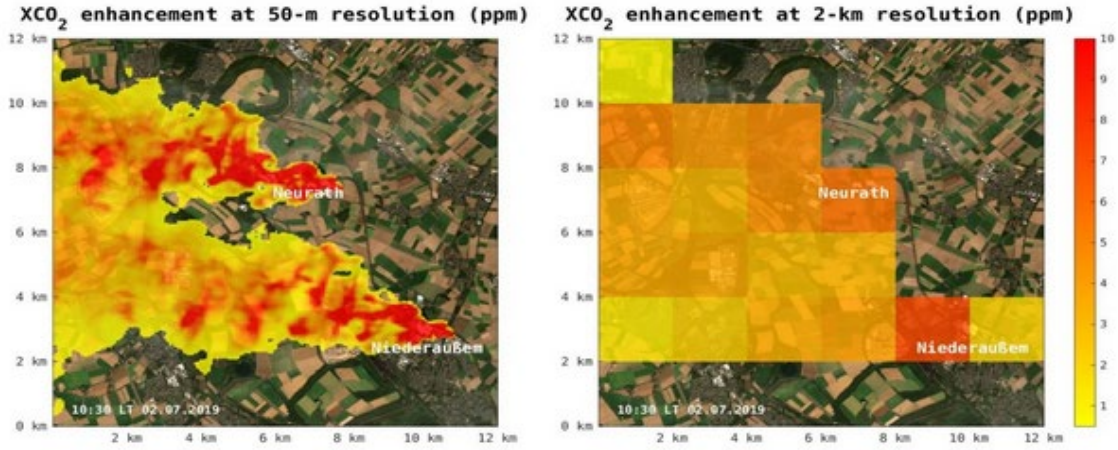

Figure 4.2: XCO_2 enhancement simulations for different spatial resolutions. Difference of CO2Image resolution with 50x50m^2 (left) to a resolution like in CO2M with 2x2km^2 (right) of the Neurath and Niederaußem power plants (Germany) J. Marshall (CC BY-ND-NC 3.0) taken from DLR - Institute for Atmospheric Physics (2022)

Table 4.1: Technical parameters of CO2Image mission after Strandgren et al. (2020), edited after CO2Image workshops at DLR, compared to the planned Copernicus CO2M mission (Kuhlmann et al., 2019)

	CO2Image	CO2M (Kuhlmann et al., 2019)
Orbit	Non sun-synchronous	602.24 km, Sun-synchronous
Mass	~90 kg	
Swath	50 km	250 km
Spatial resolution	50x50 m^2	2x2 km^2
Spectral range	1559–1672 or 1982–2092 nm	NIR, SWIR1 (1600nm), SWIR2 (2000nm)
Integration time (t_{int})	70 ms	Along-track sampling time: 0.286 s
Equator crossing times	~10:30-12:00 local time	~ 11:30 local time

4.3 Uncertainties and further studies needed

The planning of the CO2Image mission is still in progress and uncertainties regarding technical aspects as well as aspects of content and science are remaining up to now. One impact on the CO_2 plume of point sources and its CO_2 transportation is the wind direction and wind speed as well as the plume height (Nassar et al., 2017). As wind causes turbulence the plume endures dilution and CO_2 values will be underestimated. Therefore, it is necessary to take wind data into account when quantifying CO_2 emissions. Especially with wind speeds higher than 2 m per second this is important. If the wind speed is exceeding to 10 m x s^{-1}, it is probably a factor making realistic quantifications nearly impossible. Another impact on quantifying CO_2 emissions will be the height of the planetary boundary layer. Assuming that it is more stable in the mornings, due to less temperature differences, CO2Image will cross the equator around 10:30 local time, so that this issue can be neglected. A further aspect that brings uncertainty in the quantification of XCO_2 is the different Albedo of a scene. Depending on the homogeneity or heterogeneity of the scenes surface, the XCO_2 can vary significantly. Intense studies regarding the influence of the surface albedo are in progress at the DLR institute for Atmospheric Physics.

CO2Image without an own source of light is dependent on the backscattered solar radiation and thus can only measure during daylight. Furthermore, water or cirrus clouds can extend or shorten the light path of the sun to the instrument, and therefore causing CO_2 over- or underestimation of the true XCO_2. Scattering has the effect of extending or shortening the direct light path depends on the scattering angles, scattering heights, and number of events occurring (Butz et al., 2009). Light scattering can be caused by aerosols in the air. The impact of aerosols on light enhancing or shortening and thus their influence on the XCO_2 is the main topic of this thesis. The following chapter presents sensitivity studies of the impact of difference aerosol amount, height, and aerosol size and the correlation of these parameters to Albedo on quantifying XCO_2 with CO2Image.

5 Estimating GHG emissions with the full physics algorithm RemoTeC

The proposed CO2Image mission will monitor CO_2 emissions and provide the data as absorption spectra. To validate this future data different simulations with the retrieval algorithm RemoTeC (see chapter 5.2) are performed. The forward simulation of RemoTeC creates simulated spectra from atmospheric data and the retrieval determines the CO_2 concentrations out of these spectra. By comparing the input CO_2 values (true CO_2) with the retrieved CO_2 concentrations possible errors and the influence of certain parameters like scattering through aerosols can be detected. This thesis aims to detect the influence of environmental parameters like aerosol scattering or albedo on quantifying CO_2 emissions. Chapter 5.1 defines albedo and aerosols as well as aerosol scattering and describes possible impacts of change in albedo and aerosol characteristics.

To quantify this influence, aerosol studies are performed, considering aerosol scattering in creating spectra during the forward run. The studies are all performed for an example scene of 2x2 km^2 with a pixel size of 50 m. The input data for this emission plume scene comes from Large Eddy Simulations (LES) of Indianapolis. First a plume mask, according to Kuhlmann et al. (2019) was created (described in chapter 5.3). This ensures the opportunity to quantify the influence of aerosol scattering, depending on amount, size and height distribution. The automatic plume detection provides the foundation to investigate the enhancement of CO_2 inside the plume. For this step the enhanced CO_2 concentrations inside the plume compared to the background can be determined and analysed in consideration of the respectively parameter value. Moreover, the integrated mass enhancement (IME) for each simulation was calculated as it will be described in detail in chapter 5.4. Additionally, the CO_2 error, being the differences between the true CO_2 (input) and the retrieved CO_2 values, are analysed.

Simulations for this thesis are performed on the supercomputer of the DKRZ. As the DKRZ changed its high-performance computer “Mistral” to its successor “Levante” at the end of May 2022, the challenges on moving from Mistral to Levante are discussed in the appendix A as a special case. This consumed a large amount of time during this thesis, because a small evaluation had to be made in order to assure that the algorithm is running similarly on Mistral.

5.1 Influence of environment parameters on estimating emissions

Estimating CO_2 emissions from space is based on measuring reflected sunlight from the surface or particles in the atmosphere which change the measured light path. Hence, estimating CO_2 emissions is influenced by different environmental parameters. This can lead to under- or overestimating the true XCO_2.

As Nassar et al. (2017) states, the CO_2 transport from the source is conditional on the horizontal wind speed at the plume height. Thus, depending on wind direction and speed, the true XCO_2 gets underestimated due to dilution effects. Since the common observation strategy on monitoring GHG relies on the backscattered sunlight from the Earth's surface in the SWIR spectral range, knowledge about the light path and its modification through the atmosphere is crucial. The light path can be modified by particles in the atmosphere causing scattering such as water clouds or cirrus clouds, consisting of ice particles, as well as different aerosol types (Butz et al., 2012). Furthermore, the effect of surface properties is important to make an accurate estimation of the true CO_2 emissions (Ayasse et al., 2018). The influence of scattering or different surface albedo effects the measured solar radiation spectra from the satellites instrument. This work concentrates on the radiation error coming from:

- aerosol optical thickness (tau_ref)
- size distribution parameter (reff)
- height distribution parameter (alt1)
- albedo

The following chapter describes in detail the environmental parameter of albedo and aerosols and their possible effects on the quantification of CO_2 emissions within the CO2Image mission.

5.1.1 Albedo

The planetary albedo is the fraction of the incoming solar radiation scattered by the Earth's surface back to space. Thus, the albedo α is defined as ratio of upward radiance $L\uparrow$ to downward radiance $L\downarrow$:

$$\alpha = \frac{L\uparrow}{L\downarrow} \qquad (5.1)$$

While zero corresponds to a black body, that absorbs all radiance.

This reflected energy is one important component of the Earth's energy balance. Thus, it is fundamental to understand the climate of the Earth and climate change. Since the Holocene the Earth's climate can be considered nearly stable. Assuming that also the Earth equilibrium temperature has not changed much during this period, rationally the variations in albedo have been also small (Stephens et al., 2015). Being a component of the Earth's energy balance, the variability of the albedo is important to understand for:

- Energy balance models
- Climate systems
- Climate change feedback mechanism and global warming simulations
- Geoengineering

The Earth's albedo and the impact of the variability of albedo is described in detail in Payne (1972) and Stephens et al. (2015). On a global scale the albedo, measured in a height of 1.6 m, ranges from 0.1 to 0.45 if desert areas, which are mostly studied separately, are not considered (Guerlet et al., 2013). Several studies examine the variations of albedo which can cause systematic errors on XCO_2 (Ayasse et al., 2018; Guerlet et al., 2013; Zhang et al., 2017). The impact of albedo on the retrieval algorithm can cause uncertainties and spurious signals. Moreover, the retrieval can fail or cause high errors in the retrieval results, if the surface of the Earth is too dark, e.g. over water or forest canopy (Ayasse et al., 2018). In general, low albedo reduces the detectable reflected radiance between the GHG enhancement concentrations and the background concentration. However, observations over water are possible if the viewing geometry of the satellite to the sun is supportive and brightens up the scene (Jacob et al., 2022).

Therefore, the influence of different albedo scenarios on quantification of CO_2 emissions from space needs to be discussed for corresponding satellite missions. At the DLR studies are currently in progress about the influence of heterogenous and homogenous albedo scenes. This work concentrates on the correlation of albedo to sensitivity studies regarding aerosol scattering.

5.1.2 Aerosol scattering

Aerosols in the atmosphere affect the energy balance of the Earth, the atmospheric circulation, the hydrological cycle and the frequency of greenhouse and reactive trace gases. Therefore, aerosols are fundamental to understand atmospheric chemistry and physics, the biosphere, and climate in their complex completeness and to consider their impact for public health (Pöschl, 2005). Aerosols are defined as airborne solid and liquid particles in a size range of nanometres to micrometres, coming from natural or anthropogenic sources. The impact of aerosols are different depending on concentration, size, structure, and chemical composition. These parameters are highly variable in time and space (Pöschl, 2005). Condensed water, commonly known as clouds, is the most obvious and visible example for aerosols. Due the fact that clouds are widely considered as a separate phenomenon in atmospheric sciences, this work investigates the influence of suspended particles consisting of condensed matter. Sulphate, nitrate, ammonium, sea salt, mineral dust, organic compounds, and black or elemental carbon are the main chemical components of air particulate matter. The residence time of these components in the atmosphere depends on the aerosol properties and meteorological conditions and varies from hours to weeks (Pöschl, 2005). The abundance and type of aerosol has direct and indirect impacts (see Figure 5.1), which cause analytic challenges and need to be considered in simulations.

This work investigates the direct effects of aerosols on radiation focusing on scattering effects of aerosols and how these effects influence the quantification of CO_2 and CH_4 emissions through RS data. Even though RS measurements from satellites can provide data about CO_2 and CH_4 emissions, atmospheric aerosol scattering makes the retrieval challenging. Consequently, it is indispensable to understand the impact of aerosols on CO_2 and CH_4 retrievals.

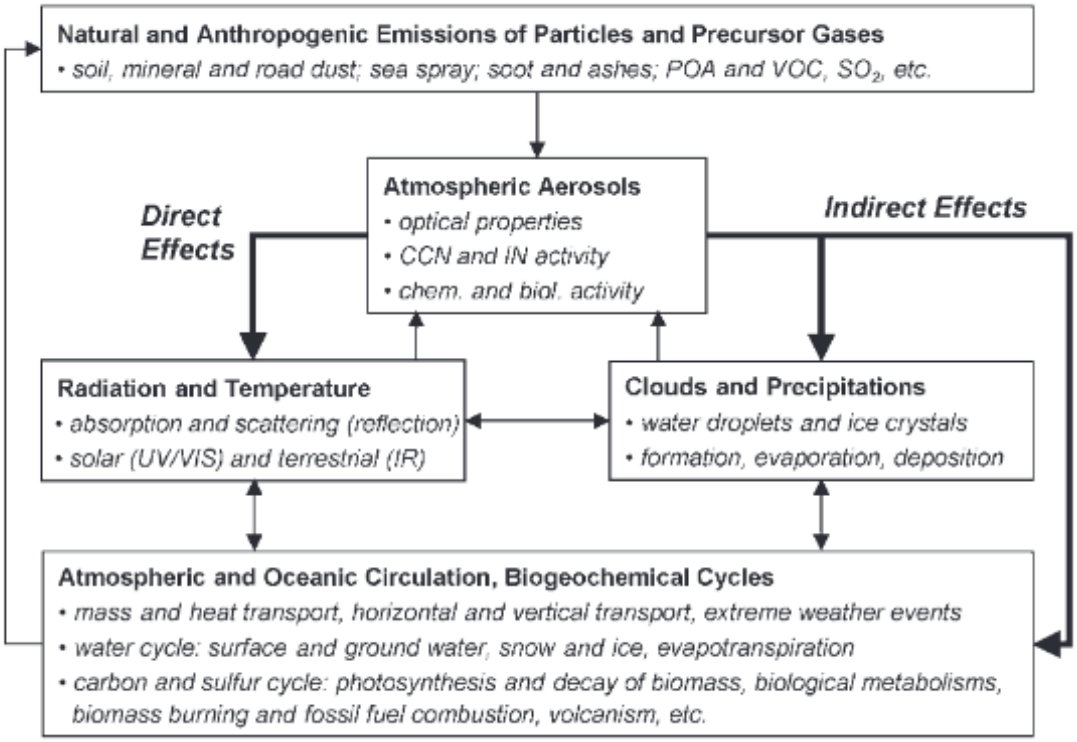

Figure 5.1: Aerosol effects (direct and indirect) and their feedback loops in the climate system from Pöschl (2005)

The present of aerosols modifies the light path of the reflected solar radiation and that's why inadequate treatment of aerosol scattering can cause errors in the process of retrieving column-averaged dry-air mole fractions of CO_2 (XCO_2) from space-based measurements of backscattered solar shortwave radiation (Butz et al., 2010; Guerlet et al., 2013; Strandgren et al., 2020). Hence, accurate knowledge of the light path modified by aerosols through the Earth's atmosphere, which depends on particle amount, type, size, and height distribution, as well as on the albedo of the Earth's surface, is necessary for accurate retrieval methods (Butz et al., 2012; Frankenberg, Meirink, et al., 2005). Uncertainties in the light path make accurate measurements of CO_2 and CH_4 emissions challenging. As CO_2 and CH_4 emissions are frequently correlated with pollution and thus aerosol emissions, a clear understanding of aerosol impact is essential to quantify CO_2 and CH_4 emissions from spaceborne observations (Guerlet et al., 2013; Huang et al., 2020; Strandgren et al., 2020).Therefore, it is crucial to consider light path extension or shortening due to aerosol scattering in the retrieval process. In aerosol science light

scattering simulations are crucial to develop new particle characterization techniques or solving inverse light scattering problems (Hergert & Wriedt, 2015).

The following section is based on Petty (2006). Detailed descriptions are available in his book “A first course of atmospheric radiation”.

Depending on the particle size the scattering of radiations is different and defining the characteristics for scattering. Particles being way smaller than the wavelength will scatter very weak but still can absorb radiation. For large particles, in proportion to the wavelength, the laws of reflection, refraction, and absorption for homogeneous material apply. But most of the atmospheric particles lie between the very small and large category. For these particles in between complex scattering methods which are taking into account wave-related phenomena, need to be used. Most of these particles, no matter if molecules, haze, or cloud droplets or even rain drops and hailstones, can be described by the Rayleigh theory or Mie theory. The Rayleigh theory applies for very small randomly orientated particles, while the Mie theory applies to spheres of random size. Figure 5.2 shows which theory for scattering is used depending on the particle size and wavelength.

This work just considers aerosols. Retrievals of an example scene of a CO_2 plume are made considering three aerosol parameters: aerosol optical thickness (tau_ref), aerosol height distribution (alt1), and aerosol size distribution (reff). The considered aerosols are in the range of such size for which the Mie theory applies. The Lorenz–Mie theory expresses the scattering of radiation in terms of an infinite series of spherical multipole partial waves (Lock & Gouesbet, 2009). Applying the Mie theory, depending on particle amount, type, size, height distribution, and reflection of the Earth’s surface (see 2.3.2 Albedo), the light path is modified differently. As information about these parameters are mostly not available, the retrieval from spectra and quantifying CO_2 and CH_4 emissions get challenging. To solve this challenge the retrieval algorithm RemoTeC was developed (Butz et al., 2009; Guerlet et al., 2013), which takes the aerosol parameters into account. Retrieval methods must deal with the aim of simultaneously inferring gas concentrations and correcting effects of aerosol scattering, as information about the aerosol parameters like amount, type, size and height distribution are mainly not available (Bril et al., 2009; Butz et al., 2009; Butz et al., 2010; Butz et al., 2012; Connor et al., 2008; Frankenberg, Meirink, et al., 2005).

The next chapter will give an overview about the retrieval algorithm RemoTeC, which simulates spectra from atmospheric data in the forward run and then retrieves the greenhouse gas concentrations from these spectra. With the retrieval algorithm aerosol studies are performed and evaluated with the methods described in chapter 5.3 and 5.4. For the evaluation, the enhancement inside the plume and the IME of the plume compared to the background are calculated. Furthermore, this work investigates how the errors coming from aerosol scattering are correlated to the surface albedo.

Thereby, the analysis is following the main research question of this thesis if aerosol scattering can be neglected when looking at the SNR.

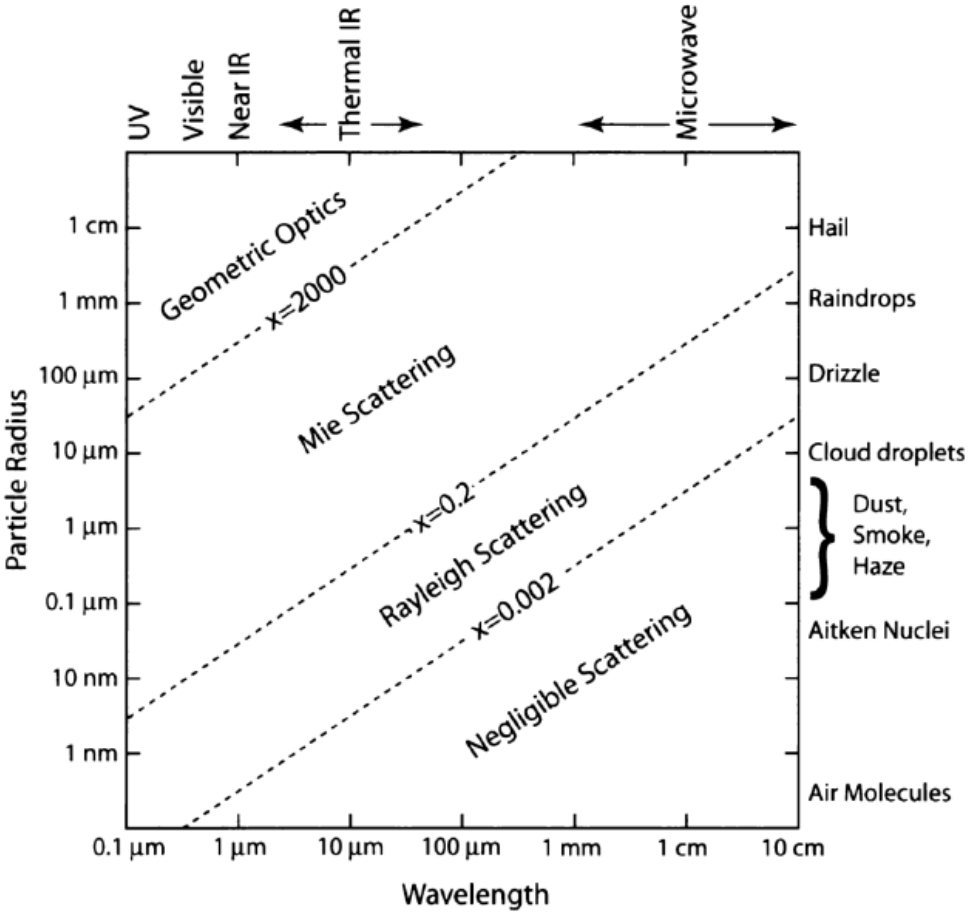

Figure 5.2: Scattering theory applying depending on particle size and radiation wavelength. The diagonal lines show the boundaries between the scattering regimes. Taken from Petty (2006).

5.2 Full physics retrieval algorithm RemoTeC

The full physics algorithm RemoTeC was developed to retrieve mainly CO_2 and CH_4 from SWIR satellite observations of backscattered sunlight.

The retrieval algorithm described here is based on the detailed description in Butz et al. (2009; 2010; 2012). The method relies on the radiative transfer model developed by Hasekamp and Butz (2008).

The forward model F, creating the simulated spectra y (simulated measurement vector with y_i of the i-th spectral element) with the target gas, is described as

$$y = F(x, b) + \epsilon_y + \epsilon_F \tag{5.2}$$

with x as state vector, containing the retrieved parameters (x_j of the j-th retrieved parameter) and b, the parameters, that are not retrieved. ϵ_y is representing the measurement noise error and ϵ_F the forward model error.

The forward model $F(x, b)$ is replaced by its linear approximation to solve the inverse problem to estimate x as the forward model is not linear in x:

$$F(x_{n+1}, b) \approx F(x_n, b) + K(x_{n+1} - x_n) \tag{5.3}$$

with K being the Jacobian matrix.

The model considers multiple scattering by molecules and particles, known as aerosols, as well as molecular and particulate absorption (Hasekamp & Butz, 2008).

Aerosol optical properties, causing aerosol scattering and absorption are derived from the Mie theory, which applies to all aerosols of spherical shape. By applying the Mie theory, the optical properties can be derived from the physical properties which can be defined in the RemoTeC algorithm. The physical input parameters are the aerosol optical thickness, the aerosol size distribution, the aerosol height distribution, and the aerosol real refractive index (m_r) and imaginary refractive index (m_i). The aerosol size distribution $n_{ae}(r)$ with the size parameter α_s is defined following the power-law size distribution after Mishchenko et al. (1999):

$$n_{ae}(r) = \begin{cases} A, & r \leq r_1 \\ A(r/r_1)^{-\alpha_s}, & r < r_1 \leq r_2 \\ 0, & r > r_1 \end{cases} \tag{5.4}$$

where r is the particle radius, r_1 = 0.1 µm, r_2 = 10 µm, and the constant A is determined from normalization of the size distribution. This equation implies that if the radius of the aerosols is big the parameter for aerosol size (reff) is small. (Butz et al., 2009)

The physical parameters about the aerosol optical thickness, aerosol size distribution and aerosol height distribution can be defined separately and different simulations depending on these aerosol parameters can be performed. From the physical parameters RemoTeC calculates the optical quantities via the Mie theory. The most important optical quantities are the single scattering albedo, phase function and optical depth. More precisely if you specify the physical quantities and RemoTeC computes the optical quantities. RemoTeC is thereby one of the few programs that have linearized the aerosol part up to the physical quantities. Accordingly, not only the optical quantities but the physical quantities can be estimated. (A. Butz, personal communication)

The retrieval is calculating the true state vector x_{n+1}, when y is known by minimizing the least squares cost function.

$$x_{n+1} = arg\,min\left(\left\|S_y^{-1/2}\,(F(x_{n+1}, b) - y\right\|^2\right) \qquad (5.5)$$

With S_y as the measurement error covariance of y.

Shortly, the retrieval algorithm RemoTeC is creating a simulated spectrum in the forward run. Hereby, it is taking aerosol scattering into account. The retrieval run estimates the XCO_2 values from this spectrum.

The retrieval algorithm RemoTeC was first used to analyse GOSAT data (Butz et al., 2011). The algorithm is capable to retrieve 12-layer-profiles of CO_2 and CH_4 column number densities while considering the aerosol amount, the aerosol size distribution and the aerosol height distribution. RemoTeC gives adequate retrievals while considering aerosol scattering for values of aerosol optical thickness at 750 nm up to 0.25 (Guerlet et al., 2013).

In this thesis scenes of a CO_2 plume of a point source are generated with the retrieval algorithm RemoTeC. Figure 5.3 shows a CO_2 plume for the example scene used in this thesis without any scattering of aerosols. Further simulations with different values

for aerosols parameters are performed and analysed. The full physics algorithm RemoTeC was provided by Prof. Dr. André Butz at the University Heidelberg and transferred from their server by the help of Leon Scheidweiler.

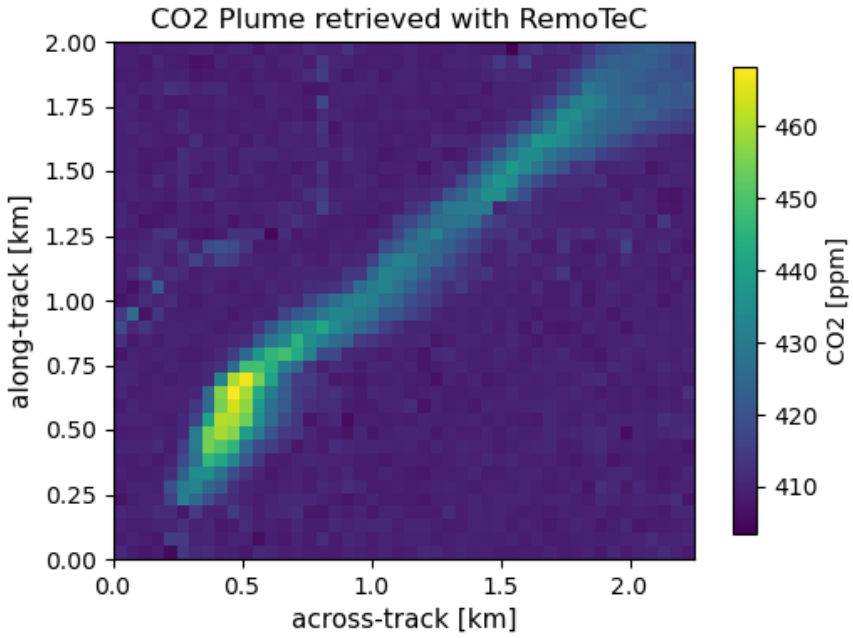

Figure 5.3: Map of CO2 values in ppm. The plume of the point source is clearly visible

5.3 Plume mask detection

The plume detection algorithm used in this thesis and described here is based on Kuhlmann et al. (2019) (Varon et al., 2018). The algorithm identifies pixels inside the emission plume of the targeted point source. Furthermore, scripts used in the analysis regarding the plume mask are based on previous scripts from Leon Scheidweiler and Johan Standgren.

If pixels in a satellite image are spatially connected with enhanced signals starting at a source, it is defined as a plume. The detection of the plume can depend on following factors:

- Visibility of plume in satellite picture, depending on number of satellites and their swath width of the instrument
- Enhanced concentration of target gas of emission plume

- Meteorological conditions, as e.g., wind can dilute the concentration
- Variability of background, surface type
- Presence of water clouds and cirrus, darkening the plume
- Precision of the instrument

Depending on these factors the detection threshold, defined as the ability to determine the plume mask against a noisy background and to retrieve the corresponding emissions, can vary significantly. Generally, it is the lowest for a flat, bright, spectrally homogeneous surface and strongly depends on the wind speed (Varon et al., 2018). The wind speed can make the detection of the threshold values difficult, because weak winds assist the detection but can cause errors in quantification (Varon et al., 2018). In this thesis most of these factors do not apply as the scene is chosen without having difficulties in visibility or problems with meteorological conditions such as wind or clouds.

The plume detection algorithm uses a statistical Z test to filter out pixels with significant higher values than variability in background.

$$Z = \frac{x - \mu}{\sigma} \tag{5.6}$$

with x being the observation, with the mean value μ and standard deviation σ.

The main aspect of this plume detection algorithm is that it takes the spatial average of pixels in a defined neighbourhood instead of a single pixel. This gives the possibility to identify signals of weak plumes and also minimizes the risk of thinning out the signal at the edges of the plume. The spatial average of a pixel is calculated with:

$$X_{CO2}^{pix} = \frac{1}{K} \sum_{k=1}^{K} X_{CO2,k} \tag{5.7}$$

with k as spatial pixel index and K the number of spatial pixels selected. This applies, if the calculating pixel is not at the edge of a scene K =5.

The detected signal enhancement against the background, determined by the Z value (equation 5.6), can be interpreted as the SNR. By that, the signal is the enhanced concentration within the plume against the background. Both, the instrument noise and spatial variability are occurring in the background.

$$SNR = \frac{X_{obs} - X_{bg}}{\sqrt{\frac{\sigma_{rand}^2}{n} + \sigma_{sys}^2}} \tag{5.8}$$

where X_{obs} are the spatially averaged satellite observations, X_{bg} represents the estimated background value, and σ_{rand} the random errors and σ_{sys} the systematic errors. To prevent conflicts in the plume detection through the variability of the background and surface type, the background is a fixed area. This area is chosen, as the scene is known outside of the plume in the upper right and lower left corner. The mean value of this area is calculated and used for X_{bg}. In large neighbourhoods and at the edges of the plume the algorithm may detect pixels outside of plume, which are then assigned to the plume at the edges (Kuhlmann et al., 2021). Thus, according to Strandgren et al. (2020), a median filter with a cross-shaped kernel smooths the finished plume mask by extending the arms of the cross used for the Z-test by one pixel. The largest spatially connected selection of enhanced pixels defines the emission plume mask of the observed point of interest. This plume mask is used for further analyzations in the sensitivity studies regarding the influence of aerosol scattering in this thesis. Figure 5.4 shows the retrieved CO_2 plume by the algorithm RemoTeC and the consequently generated plume mask with the method described in this chapter 5.3. Also, the fixed background is shown, which is chosen based on the knowledge where the plume is.

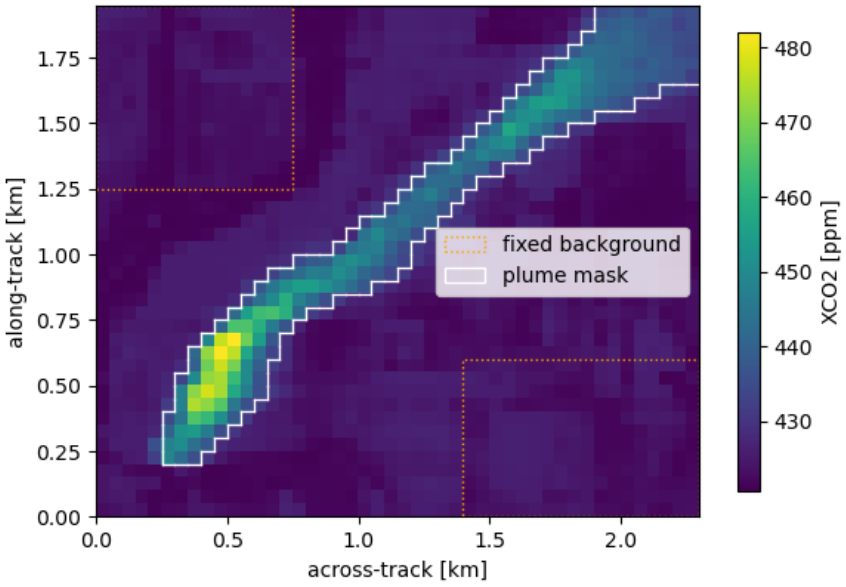

Figure 5.4: Retrieved XCO2 values with marked plume and background area. The simulation was made with aerosol scattering, with the aerosol parameters: aerosol height of 3000 m, aerosol size= 3.5 and aerosol amount = 0.001, having very few aerosols. The white line shows the detected plume. The background pixels are marked with an orange dotted line. The mean value for the background pixels is 427 ppm but depends on the aerosol parameter.

5.4 Evaluating estimated point source emissions

This section is based on Varon et al. (2018) and supplementary based on Kuhlmann et al. (2021). To analyse the results of the aerosol studies performed by the retrieval algorithm RemoTeC the IME method is used. The IME relates the total plume mass to source rate, when detected in wind direction, beginning at the source. Varon et al. (2018) showed in his study that the IME method with local measurements of the wind speed at 10 m height can derive source rates with an error of 0.07 until 0.17 t per hour with +5 %– until 12% uncertainties depending on the instrument precision (1 %–5 %). The IME will be calculated for the different simulations with different aerosol values regarding amount, size and height distribution and giving a quantified expression of the influence of the individual aerosol parameter.

For a first evaluation of the influence of aerosol parameters the XCO_2 error, which is the difference between input CO_2, also referred to as the true CO_2 and the XCO_2 after the retrieval, is calculated for each spatial pixel:

$$X_{CO2}^{err} = X_{CO2}^{retr} - X_{CO2}^{true} \tag{5.9}$$

To determine the IME for each simulation, used to evaluate the influence of aerosol scattering, first the enhancement of XCO_2 in ppm with respect to the background and its error need to be calculated:

$$X_{CO2}^{enh} = X_{CO2} - X_{CO2}^{bg} \tag{5.10}$$

The respective error is calculated through:

$$\Delta[X_{CO2}^{enh}] = \sqrt{(\Delta[X_{CO2}])^2 + (\Delta[X_{CO2}^{enh}])^2} \tag{5.11}$$

The X_{CO2}^{enh} is plotted with its mean and standard deviation against the aerosol parameters: aerosol amount (tau_ref), aerosol height distribution (alt1), and aerosol size distribution (reff) in the analysis.

The enhancement of XCO_2 is converted into mass enhancement Ω^{enh} in kg CO_2:

$$\Omega^{enh} = \frac{COL_{air}}{N_a} * M_{CO2} * X_{CO2}^{enh} \tag{5.12}$$

with COL_{air} as the vertically integrated air mass, Avogadro constant N_a= 6.022 × 10^{23} mol^{-1}, and M_{CO2} = 44.01g mol^{-1}, which is the molar mass of CO_2.
The associated error is described as:

$$\Delta[\Omega^{enh}] = \Omega^{enh} * \sqrt{(\frac{\Delta[X_{CO2}^{enh}]}{X_{CO2}^{enh}})^2} \quad (5.13)$$

The mass enhancement is converted to the integrated mass enhancement IME. Therefore, the IME is the mass of CO_2 which is emitted by an observed point source for the area of the entire scene. Therefore, the IME is expressed as the sum of the mass enhancement over all spatial pixel:

$$IME = \sum_{j=1}^{M} * \Omega_j^{enh} * Aj \quad (5.14)$$

with M, the number of spatial pixels, j the index of spatial pixels and Aj the area of j. In this thesis this area is 50 x 50m^2 for all j.
The error of the IME is given with:

$$\Delta[IME] = \sqrt{\sum_{j=1}^{M}(\Delta[\Omega_j^{enh}] * A_j)^2} \quad (5.15)$$

As the plume detection finds a plume for every simulation separately, the plume mask varies for each scenario. Therefore, the IME is calculated per plume length in order to ensure comparability.

$$IME_{per\ lenght} = \frac{IME}{L} \quad (5.16)$$

The length of the plume is calculated by:

$$L = \sqrt{A} \quad (5.17)$$

with A as the area of pixels inside plume. Thereby, the number of pixels is multiplied by the pixel size. In this thesis one pixel is 50 x 50 m^2.

6 The influence of environmental parameters on the quantification of CO_2

This chapter presents the results of studying the influence of environmental parameters on the quantification of CO_2 emissions of point source emissions in the DLR satellite mission CO2Image. To perform this study different simulations with RemoTeC were performed.

At first, this chapter gives a short overview of the input data that was used for the example Indianapolis scene. This scene is used for all simulations. Afterwards, this chapter presents the results of the aerosol studies on quantifying CO_2 emissions. Even if CO2Image will be able to monitor CO_2 and CH_4 emissions, it primarily aims to quantify CO_2 emissions. Therefore, this study concentrates on monitoring CO2 emissions and all case studies are simulated and calculated for CO2.

The measured light path of the backscattered solar radiation is modified depending on the amount of aerosols in the atmosphere, their optical properties and height and the surface albedo (Strandgren et al., 2020). Incomplete and uncertain knowledge about this modification of the light path can therefore lead to errors in estimating the CO_2 emissions. To quantify the impact of aerosol scattering, different simulations with the RemoTeC algorithm on DKRZ's supercomputer Levante are performed. The full-physics algorithm is capable of considering aerosol optical thickness, aerosol height distribution and aerosol size distribution. Thereby, in the forward model of RemoTeC these parameters are considered by simulating the synthetic spectra. From these simulated spectra the CO_2 values are retrieved. All simulations are performed at the O_2A-band at 765 nm. The methods used for this thesis are described in detail in chapter 5. Different XCO_2 retrieval errors can occur when retrieving the XCO_2 values from the simulated synthetic spectra. Such errors are expected on a global scale and appear as a result of instrument noise or lack of knowledge about the modification of the light path by scattering of aerosols in the atmosphere (Strandgren et al., 2020). This study evaluates the XCO_2 retrieval errors and the influence on quantifying CO_2 emissions due to different aerosol optical thickness (tau_ref), aerosol size distribution (reff) and aerosol height distribution (alt1), as well as the influence of the surface albedo.

Chapter 6.2 shows the difference between simulations without aerosol scattering and simulations that consider aerosol scattering in the forward run of RemoTeC. Furthermore, the source of error due to adding random noise is addressed. The following studies show the impact of aerosol optical thickness (study 1), aerosol height distribution (study 3) and aerosol size distribution (study 5) each separately. For each parameter different simulations with increasing values are performed and analysed. Therefore, the partial derivation for every aerosol parameter is given.

Moreover, studies with different values for aerosol amount, height distribution and size distribution inside the plume, while the background stays constant with very few aerosols outside the plume, are performed (studies 2, 4 and 6). These studies investigate the impact of aerosols on the quantification of CO_2 when the values for aerosol amount, height distribution and size distribution increase within the plume whereas outside the plume is a very low aerosol concentration. This is considered as the most realistic case. Additionally, the influence of the albedo of the scene is investigated in chapter 6.4.

When performing these studies, the main research questions is how much aerosol scattering influences the CO_2 quantification of emission plumes of small to middle sized point sources is investigated. Through the aerosol studies this thesis aims to answer the question if aerosol scattering can be neglected as the SRN is measured for the CO2Image mission of the DLR.

6.1 Input Data for the simulations

The example scene used for the simulations is located in the city of Indianapolis in the US state Indiana. It has a size of 2 x 2 km^2 with 50 x 50 m^2 pixels size. For all simulations of a CO_2 plume this section of the city Indianapolis is used. This ground resolution is chosen so that valid statements can be drawn for the CO2Image project of the DLR. CO2Image will be the first satellite mission to detect CO_2 and CH_4 with a ground resolution of 50 x 50 m^2. Therefore, new studies are necessary for the satellite mission CO2Image.

The CO_2 background concentration for this scene in Indianapolis is provided by the CarbonTracker CT2017 dataset (NOAA, 2022a; Peters et al., 2007). The annual estimated CO_2 emissions for Indianapolis from fossil fuels are contributed by the Hestia project (Gurney et al., 2012; Gurney et al., 2019). The Hestia project gives bottom-up estimates of CO_2 emissions for an entire urban landscape of point sources like individual buildings and industrial facilities on an hourly basis (Gurney et al., 2012).

As the spatial resolution of the CarbonTracker CT2017 dataset with its 1° x 1° is not detailed enough the whole example scene with emissions from Hestia in Indianapolis is covered by one CarbonTracker CT2017 pixel (Strandgren et al., 2020). This means a constant CO_2 value is set for the background concentration for all simulations. Furthermore, the ICON dataset of the Max-Planck-Institute (ICON, 2022) and the CarbonTracker CT2017 dataset provide vertical profiles of temperature, pressure, CO_2 and H_2O, of July, 15 2016 for the Indianapolis scene (Strandgren et al., 2020). Whilst the CO_2 is the main absorber for the retrieval, H_2O is interfering as an additional absorber.

To get realistic surface reflectance, data from Sentinel-2 (Sentinel-2, 2022) is used. It provides TOA reflectance for the Indianapolis scene. This data is converted into a surface albedo at a wavelength of 2000 nm. Figure 6.1 shows the albedo values for each pixel in the example scene of Indianapolis at 2000 nm. The albedo input values show a realistic heterogenous scene with a river in the upper right corner. The river is indicated by the bow of very low albedo values.

Sentinel-5 Precursor data (Sentinel-5P, 2022) provide the solar irradiance. The knowledge about the airmass, which is needed to calculate the retrieved XCO_2 values, is assumed. Nevertheless, meteorological and topography data would be necessary to estimate the airmass (Strandgren et al., 2020).

The input file for the simulation in RemoTeC is summarizing all the above-mentioned data. The input file, as well as the output file, of RemoTeC is in the netCDF format.

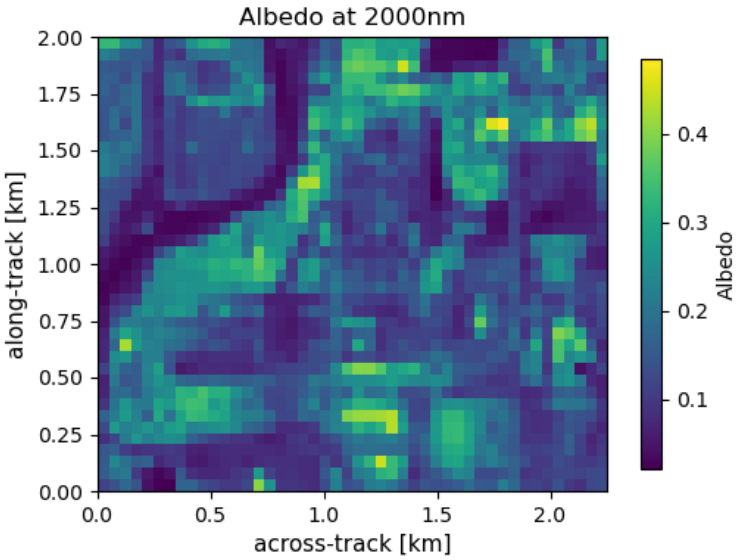

Figure 6.1: Map of the surface albedo at 2000 nm. This scene is the input albedo for all further simulations.

6.2 Simulations without vs. with aerosol scattering

This thesis aims to analyse the influence of aerosol scattering on the CO_2 quantification of emission plumes. Therefore, simulations of the example scene of Indianapolis for one single plume are performed. Simulations that do not consider scattering by particles which are present in the atmosphere are called nonscattering simulations. These nonscattering simulations figure out the transmittance of the light path (Strandgren et al., 2020). This chapter shows the difference between simulations without aerosol scattering and simulations which consider aerosol scattering in the forward run of RemoTeC. Furthermore, the source of error by adding random noise error is addressed shortly in this section.

Figure 6.2 shows a nonscattering simulation of a CO_2 plume. Therefore, scattering by aerosols is not considered during the forward run in RemoTeC. Moreover, the XCO_2 error (equation 5.10) and its correlation to the albedo values is shown. Pixels with low albedo show a bigger error than pixels with high albedo values which have an error close to zero. Low albedo values are related to a dark surface like the river which is visible in the upper left corner of the plot. Accordingly, it can be concluded that pixels with dark surfaces in the scene lead to a bigger XCO_2 up to 11 ppm.

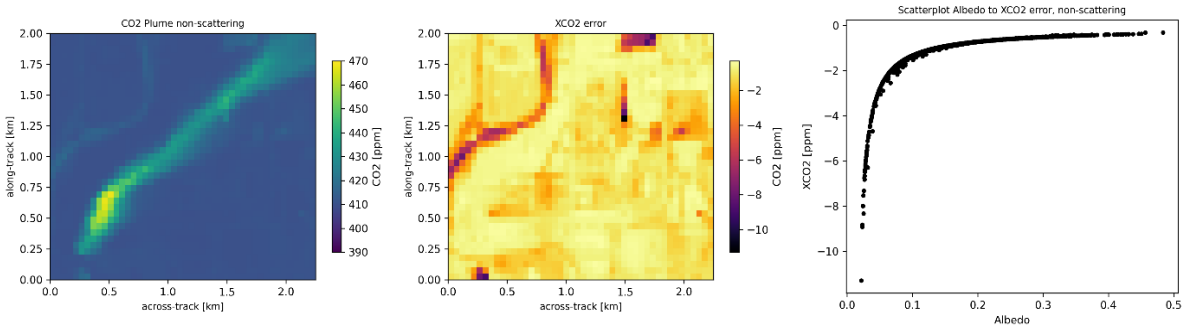

Figure 6.2: CO2 Plume with no scattering of aerosols retrieved with RemoTeC (left), XCO2 error (middle), Scatterplot albedo vs error XCO2 (right).

One example for the difference between the CO_2 plume performed on Levante without considering aerosol scattering (upper plot) and one simulation considering aerosol scattering (lower plot) is presented in Figure 6.3. The plot on the right gives the difference of every pixel between the two simulations. The CO_2 values vary from 50 ppm to -20 ppm. It is clearly visible, that the biggest differences occur at pixels with very low albedo values. If these pixels are not considered the difference between the simulation without aerosol scattering and with aerosol scattering will be around ± 10 ppm. Having these single pixels, which got randomly very high (up to 800 ppm) CO_2 values, was one main problem that occurred when performing the simulations on Levante. These pixels came from randomly added noise error. To solve this problem the seed for all simulations was set constantly to 3.1415. By having the same noise error for every pixel, these very high CO_2 values did not occur anymore what makes it possible to compare differences caused by environmental parameters and not by noise error. Precisely, with a fixed seed it is possible to compare the simulations and it is ensured that the observed differences are caused by the changed parameter. Furthermore, a fixed seed makes the simulations and also the analysis reproducible.

Simulations of CO_2 plumes with random seeds are shown in the appendix in Figure B.1. All further studies to investigate the influence of the environmental parameters coming from aerosol scattering or different albedo scenarios are performed with a fixed noise seed.

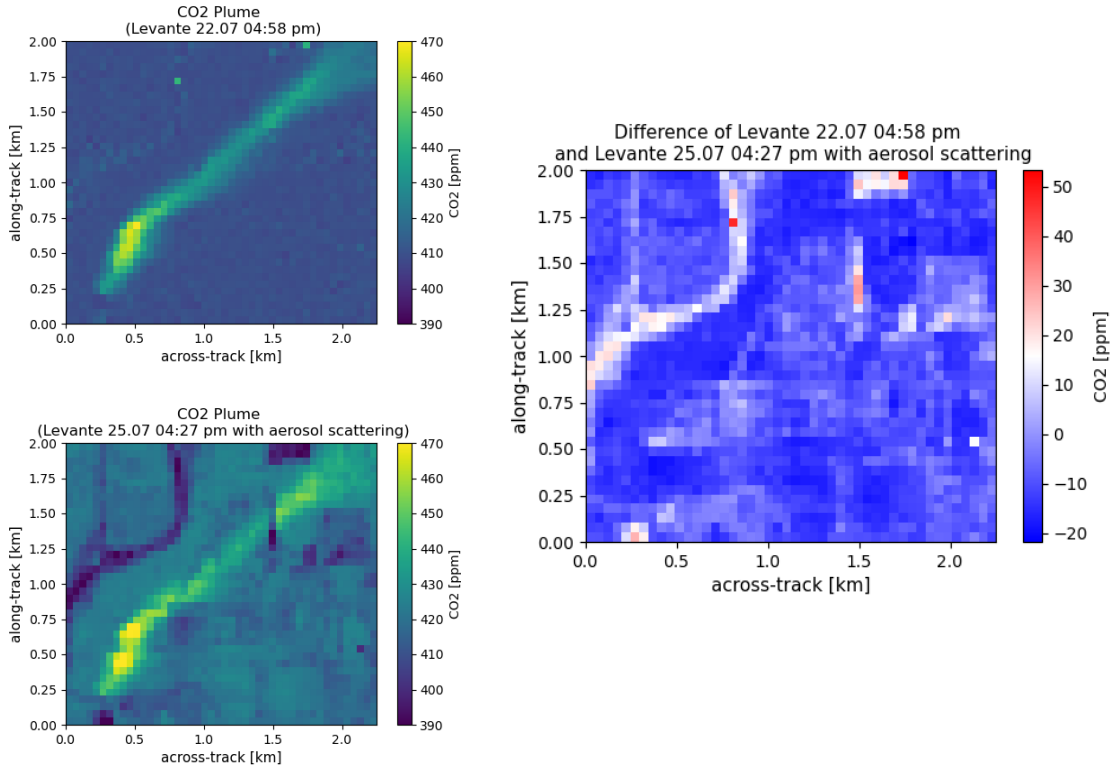

Figure 6.3: Plume without aerosol scattering (upper), Plume with aerosol scattering (lower) and the difference between the two simulated plumes (right).

6.3 Results of the aerosol studies

The light path of the reflected solar radiation measured by the instrument of the DLR satellite mission CO2Image can get modified by scattering due to aerosols in the atmosphere. As a consequence, large errors in the retrieved XCO_2 values can occur when the effect of absorption of CO_2 and the scattering effect of particles cannot be cut apart. (Strandgren et al., 2020).

Therefore, this thesis performs aerosol studies to define the influence of different aerosol parameters. Different simulations which consider aerosol scattering in the forward run of the retrieval algorithm RemoTeC are performed for the aerosol studies. Thereby, the influence of three aerosol parameters is investigated. These three physical aerosol parameters are aerosol optical thickness, which is referred to as aerosol amount (tau_ref), aerosol height distribution (alt1) and aerosol size distribution (reff). The influence of these aerosol parameters is estimated by setting different values for each parameter. Thereby, each parameter is calculated and analysed individually to get the respective

partial derivative. For each aerosol parameter the following values are set, and simulations are performed with RemoTeC:

- tau_ref = 0.001, 0.01, 0.05, 0.1, 0.3, 0.5
- alt1 = 0, 500, 1500, 3000, 5000, 8000, 12000
- reff = 2.5, 3.5, 4.5, 5.5

Whereas one value is changed the other parameters stay constant with tau_ref= 0.1, alt1= 3000 and reff= 3.5.

The configuration used for the retrieval algorithm RemoTeC applies only for one aerosol type. Thus, it is assumed that all aerosols have the same index of refraction. With the real refractive index m_r=1.3 and the imaginary refractive index m_i=0.001, the refraction index is close to the refraction index of liquid water. The optical parameters of the aerosols get calculated by RemoTeC through the defined physical parameters like the aerosol amount, aerosol size distribution and aerosol height distribution. Consequently, the optical parameters are different for each simulation, as one of the three mentioned physical parameters gets changed for each simulation. The retrieval algorithm RemoTeC, its configuration and the physical aerosol parameters which can be defined for different runs are explained in detail in chapter 5.2.

In the evaluation the CO2 values of the scene for each individual simulation are shown, as well as the XCO2 error and its correlation to the surface albedo. Furthermore, a plume mask for the CO_2 emissions is applied by the automatic plume detection described in chapter 5.3. Then the enhancement inside the plume can be calculated. With the IME (see chapter 5.4) calculated from the enhancement inside the plume, statements can be made about the influence of the respective parameter on the quantification of the CO_2 emissions.

Additionally, study 2, 4 and 6 present the results of a case with varying values for aerosol amount, height distribution and size distribution inside the plume and a constant background with low aerosol amount outside the plume (tau_ref=0.0001). As it is assumed that point sources like industries not just emit CO_2 but also aerosols like soot particles, this is expected to be the most realistic case. Table 6.1 gives an overview of the different scenarios investigated in this work. The different studies can be separated into two main scenarios. The first scenario applies to the studies where the aerosols are homogenously dispersed over the whole scene (studies with uneven numbers), whereas the

second scenario refers to studies which have the changing aerosol parameters inside the plume while outside the plume the aerosol amount stays constantly low (studies with even numbers). The scenario of the aerosols being homogenously dispersed over the whole scene can once again be split into two cases. Thereby, the first case presents the results, that an automatic plume detection is applied. This leads to differences in the plume mask in size and shape. The other case applies the same plume mask to all different simulations. Here knowledge about the location and size of the plume is assumed. All scenarios are calculated for each aerosol parameter: the aerosol optical thickness, the aerosol height distribution, and the aerosol size distribution.

Table 6.1: Overview over the different case studies performed to investigate the influence of the aerosol parameters of aerosol optical thickness, aerosol height distribution and aerosol size distribution. The respective study and important Figures and Tables are listed for each case. Mainly the result part of this work can be divided into two groups: one scenario having the aerosols

	Aerosols homogenously dispersed over the whole scene		**Increasing values for the aerosol parameters inside plume**
	Plume mask with different size and shape	**Same plume mask (tau_ref=0.0001)**	
aerosol optical thickness (tau_ref)	**Study 1:** Figure 6.5, Figure 6.7, Figure 6.8, Table 6.2	**Study1:** Figure 6.9, Figure 6.10, Table 6.3	**Study 2:** Figure 6.11, Figure 6.12, Table 6.4
aerosol height distribution (alt1)	**Study 3:** Figure 6.14, Figure 6.15, Table 6.5	**Study 3:** Figure 6.16, Figure 6.17, Table 6.6	**Study 4:** Figure 6.18, Figure 6.19, Table 6.7
and aerosol size distribution (reff)	**Study 5:** Figure 6.21, Figure 6.22, Table 6.8	**Study 5:** Figure 6.23, Figure 6.24, Table 6.9	**Study 6:** Figure 6.25, Figure 6.26, Table 6.10

6.3.1 Study 1: Influence of increasing aerosol optical thickness for a homogeneously dispersed aerosol scenario

This section presents the analysis and the results of the influence of the aerosol parameter aerosol optical thickness (tau_ref).

In order to generate statistically robust statements on the influence of the increase of the aerosol optical thickness on the quantification of CO_2 emissions on point sources, different simulations with increasing aerosol optical thickness were performed. The exact values for tau_ref are 0.001, 0.01, 0.05, 0.1, 0.3 and 0.5. The Sahara dust events with values from 0.3 to 0.5 provide a reference for the aerosol optical thickness, because they occur quite frequently in central Europe lately.For each value one simulation with RemoTeC was carried out. While the parameter for the aerosol height distribution (alt1) was set constantly to 3000 m and the value for the aerosol size distribution was set to 3.5.

Figure 6.4 shows the image plot for the simulated scene on the left side for each simulation with different values for the aerosol optical thickness. The scene is the previously mentioned example scene of Indianapolis with a size of 2 x 2 $km^2$and a pixel size of 50 x 50 m^2. Yellow pixels in the plot show high XCO_2 values and mar a very visible plume for the simulations with tau_ref values of 0.001, 0.01 and 0.05. With values of 0.1 for the aerosol optical thickness and higher, the coherent plume is harder to detect. This issue of detecting a coherent plume starting from the source is discussed more detailed in the following. The XCO_2 values for all simulations lay between 320 ppm and 460 ppm. However, to still be able to see structures of the different XCO_2 values between the individual pixels, the range of the CO_2 values in these plots are chosen to start at 390 ppm. This implies that simulations with higher tau_ref values and thus more aerosols in the atmosphere appear darker as those having lower XCO_2 values. To be able to see the differences of this simulations in a wider range in the colour scale and to address the problem of a coherent plume, the simulation with 0.5 for the tau_ref value is shown in Figure 6.6 again but this time more precise in a bigger size.

The middle column of the Figure 6.4 shows the XCO_2 error where the input CO_2 values, which are regarded as true CO_2 are subtracted from the retrieved CO_2 values for each single pixel separately (see equation 5.10). Therefore, the XCO_2 error shows the difference between the retrieved CO_2 and the true CO_2 in ppm. The simulation with a tau_ref of 0.001 gets XCO_2 errors in the negative spectrum from 13 to 22 ppm. An

increase of the tau_ref of 10% to the value of 0.01 does not bring much improvement in the XCO_2 error as the error reaches values from 12 to 21 ppm. The simulation with the least differences between the true CO_2 and the retrieved CO_2 is the simulation with a value of 0.05 for tau_ref with XCO_2 errors of -2 to 20 ppm. The simulation with 0.1 for tau_ref gets errors from 20 to -20 ppm. With increasing values for tau_ref (0.3 and 0.5) the errors for the single pixel get bigger with a difference of -60 ppm and -80 ppm between the true CO_2 and the retrieved CO_2. It is striking that small tau_ref values have positive errors and with increasing tau_ref values the XCO_2 errors get negative. As the error is calculated in the way that the true CO_2 value gets subtracted from the retrieved CO_2 value (equation 5.10), positive errors imply that the retrieved CO_2 gets overestimated. On the other hand, negative XCO_2 errors indicate that the retrieved CO_2 values get underestimated. Consequently, in scenes with few aerosols present in the atmosphere the retrieved CO_2 gets mostly overestimated. On the other hand, with increasing aerosol amounts the retrieved CO_2 gets more underestimated. The column on the right side in Figure 6.4, which shows the correlation of the XCO_2 error to the albedo values of the scene, is presented in a scatterplot. With increasing values for tau_ref the correlation of the XCO_2 error to the albedo of the surface grows stronger. For the tau_ref values of 0.001 and 0.01 dark surfaces and therefore low albedo values corelate with less positive XCO_2 errors. On the other hand, bright surfaces are correlated with higher positive XCO_2 values. This indicates that in simulations with very few aerosols the retrieved CO_2 values get overestimated, especially for bright surfaces more than for low surface albedo values. If tau_ref is equal or bigger than 0.1 the correlation between the XCO_2 values and the surface albedo is increasing. Hereby, negative XCO_2 errors correlate with low albedo values, standing for dark surfaces. The XCO_2 error changes from negative to positive with increasing albedo. For the four simulations with tau_ref= 0.05, 0.1, 0.3 and 0.5, this change from negative to positive XCO_2 values happens for albedo values lower than 0.1. This shows that the retrieved CO_2 values get underestimated for pixels with albedo values lower than 0.1 and overestimated for bright surfaces with albedo values higher than 0.1.

To be able to make statistical statements about the different XCO_2 values and to quantify the CO_2 enhancement inside the plume in contrast to the background concentration of the scene, as first step of the evaluation a plume mask for each simulation is applied. The background area and the automatic plume detection is stated in chapter 5.3.

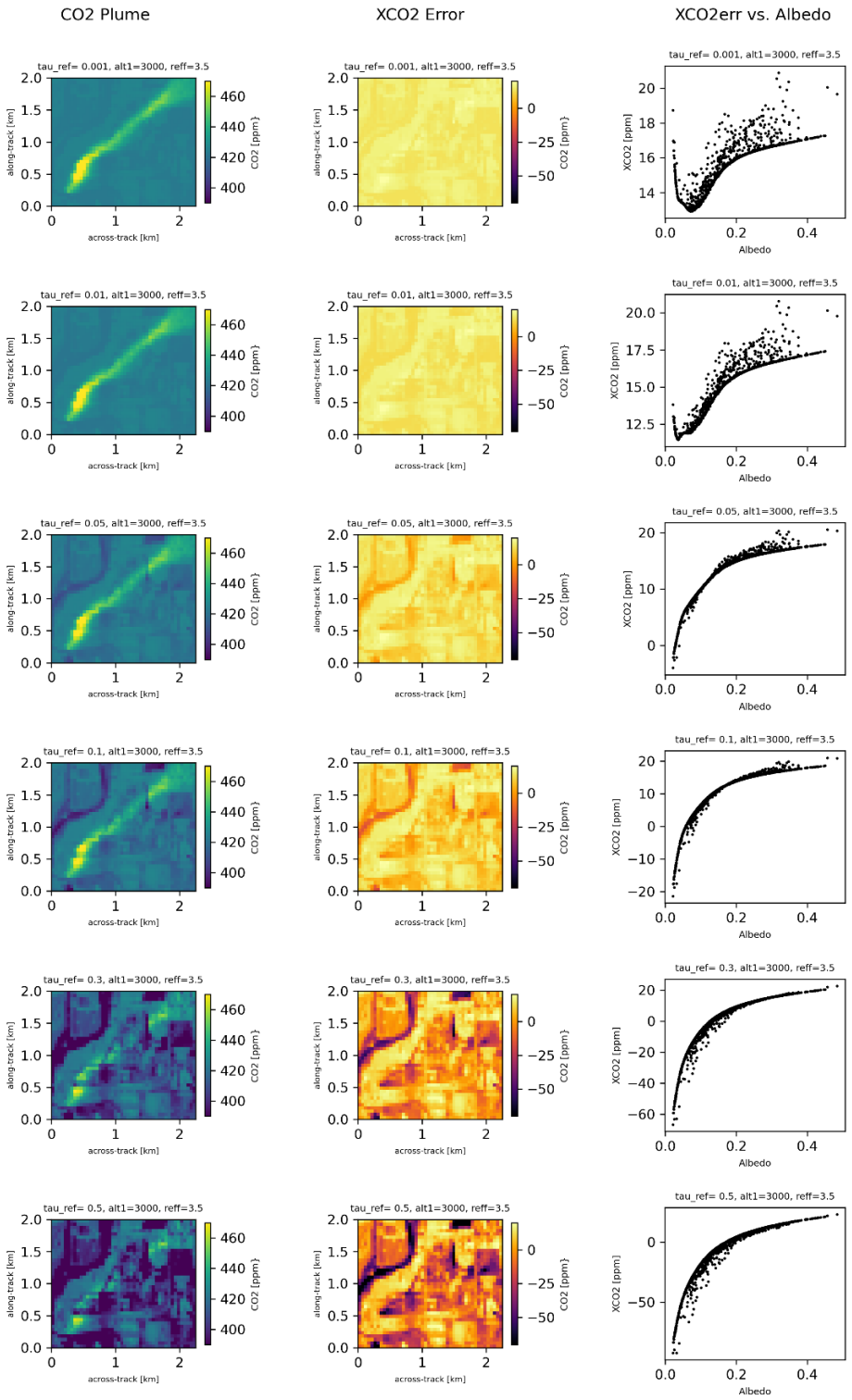

Figure 6.4: CO2 plume, XCO2 error and its correlation to albedo values for simulations with different values for aerosol optical thickness (tau_ref = 0.001, 0.01, 0.05, 0.1, 0.3 and 0.5). The aerosol height distribution is constant with alt1=3000 m for every simulation. The aerosol size distribution (reff) has a constant value of 3.5 for each simulation of varying values for tau_ref.

Figure 6.5 shows the results for XCO_2 inside the plume of the simulations with different tau_ref values. In this plot the automatic plume mask detection is applied for every simulation separately. Hence, every plume mask has a different size and shape depending on the enhancement of the pixels against the mean background value. To find out the exact threshold when the automatic plume detection is not able to find the whole plume anymore and thus missing some pixels inside the plume and changing the size and shape for the plume, more simulations with tau_ref values between 0.01 and 0.1 have been made. As stated earlier, for simulations with tau_ref equal to 0.1 or higher the plume mask detection is not able to find the whole plume as values within the plume are lower than the statistical threshold used to distinguish pixels inside and outside the plume. This threshold is based on the mean values of the pixels itself and neighbourhood pixels against a defined mean background value (see equation 5.7 and 5.8). Furthermore, alarming is that for a tau_ref value of 0.5 the automatic plume detection is not even able to find the plume with its origin at the actual source. The detected plume is instead located in the upper right corner for this simulation and not connected to the source which is located in the down left corner of the plot. Figure 6.6 shows the CO_2 values for the simulation with 0.5 for the aerosol optical thickness while alt1 is 3000 m and reff is 3.5. The CO_2 values for each pixel of the scene lie between 320 ppm and 460 ppm. Light blue and yellow colours mark pixels with CO_2 values over 400 ppm. In the scene it is clearly visible that there is no coherent plume visible. There are two regions with high CO_2 values, one in the upper right corner and one in the lower left corner. Nevertheless, these pixels with high CO_2 values are not connected. Furthermore, it is not possible to make out the location of the source. Apparently, the automatic plume detection, described in chapter 5.3, is not able to find a coherent plume. As this has the consequence that the automatic plume detection just finds a smaller plume, it is assumed that for this simulation the retrieved CO_2 gets even more underestimated.

To evaluate the influence of the aerosol amount on the quantification of CO_2, the enhancement of CO_2 inside the plume against the background for each simulation is calculated. The mean background value for the simulations with tau_ref equal and smaller than 0.1 lies slightly above 427 ppm. For simulations with more aerosols present in the atmosphere the mean background values decrease down to 422.304 ppm for tau_ref= 0.1 and 403.6 ppm for a tau_ref of 0.5. The mean background value is the same than in the

case of a changing plume mask, as the background is a defined area which does not change (see Figure 5.4).

The CO_2 enhancement inside the plume against the mean values of defined background area of each scene varies from around 17 ppm for tau_ref values smaller than 0.01 up to 21.5 ppm for tau_ref= 0.1, up to a 29.2 ppm CO_2 enhancement related to a tau_ref value of 0.5. The mean enhancement for many aerosols, present in the atmosphere, being much bigger, can be explained through a smaller detected plume. This is caused by the automatic plume detection, that does not find the whole coherent plume leading to many pixels with small enhancements getting lost and therefore they are being not considered as part of the plume. Accordingly, only pixels with big enhancements are considered, this result in a bigger mean enhancement in contrast to the background. According to equation 5.13, the CO_2 enhancement in ppm is further on calculated into a mass enhancement in kg. The mass enhancement reaches values from 0 kg to 0.8 kg as shown in Figure 6.5. The mean enhancement of the simulations individually starts with values of around 0.26 kg with the tau_ref value being equal or smaller than 0.1 and increase to 0.441 kg with the tau_ref value being 0.5. The mean background values and the mean CO_2 enhancement in ppm and kg of the plume against the background are summarized in Table 6.2.

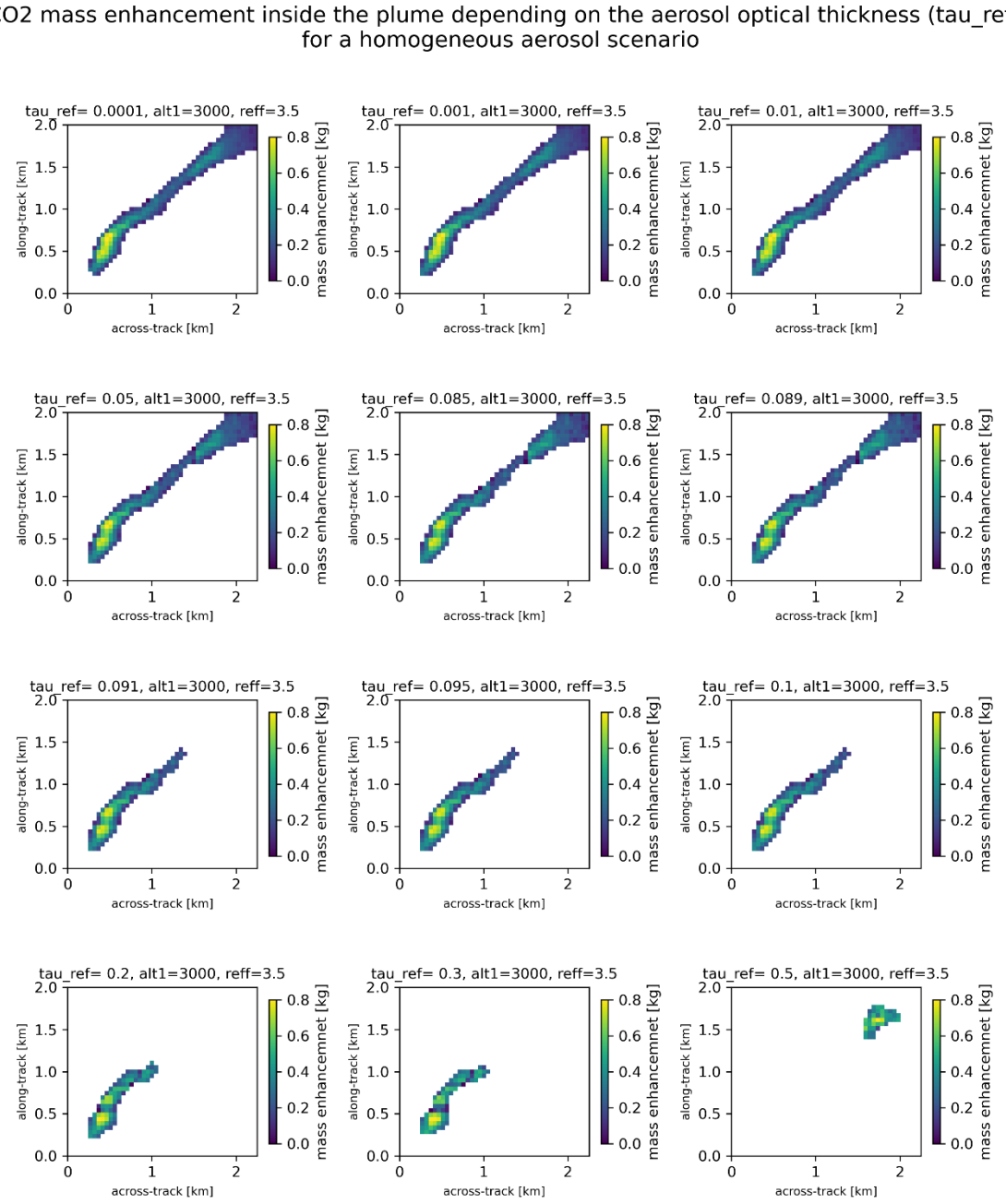

Figure 6.5: The mass enhancement of the XCO2 values inside the plume for different simulations with varying tau_ref values is shown. The automatic plume mask is applied for every simulation separately. Therefore, every plume mask shows differences in size and shape depending on the enhancement of each pixel against the mean background value.

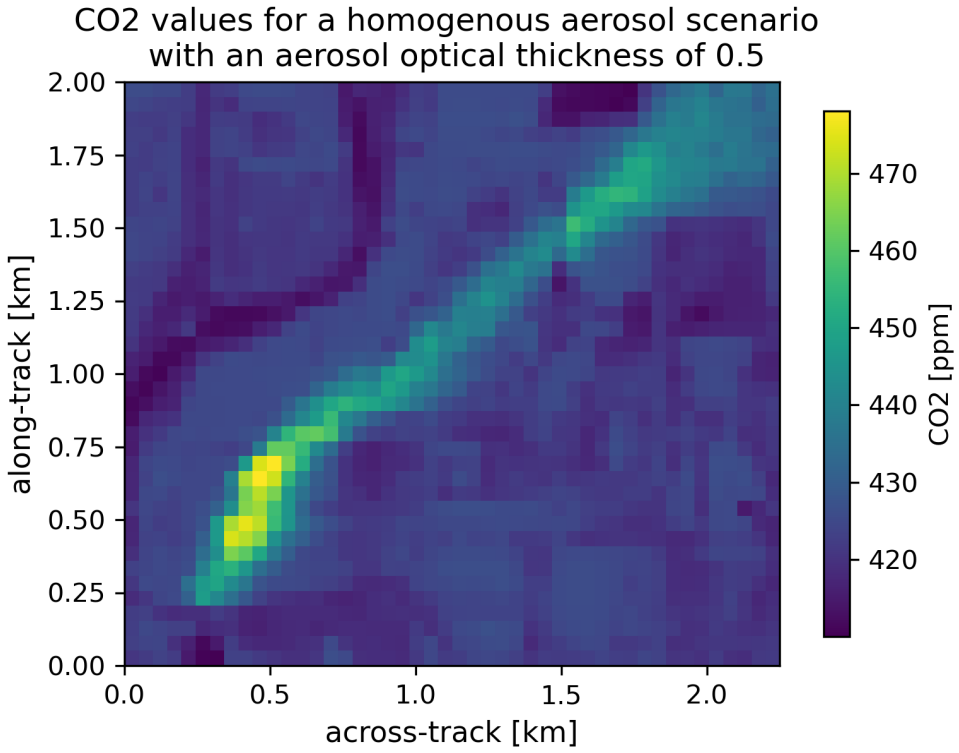

Figure 6.6: CO2 Plume for a scenario with tau_ref= 0.5, alt1=3000 and reff= 3.5. This simulation clearly shows that due to aerosol scattering no coherent plume is visible.

To make statistically valid statements, the IME according to equation 5.15 was calculated for each simulation. Figure 6.7 shows the resulting IME for simulations with different tau_ref values. The x-axis shows the varying tau_ref values and the y-axis the IME for XCO_2 in kg. The range of the IME with different values for the amount of aerosols reaches up to marginally over $1.66 \pm 0.044 \times 10^5$ kg for simulation with tau_ref smaller than 0.089. Then a drop down to $1.0 \pm 0.04 \times 10^5$ kg in the IME for tau_ref values bigger than 0.091 is detected. The lowest value of the calculated IME is $0.474 \pm 0.0574 \times 10^5$ kg for the tau_ref=0.5 simulation.

Additional simulations with tau_ref between 0.05 and 0.1 have been carried out in order to detect the threshold, that leads to the automatic plume mask detection not being able to detect the entire plume anymore. For simulations with tau_ref exceeding 0.9 the automatic plume detection is not able to find the whole plume anymore. This threshold is also visible via the calculation of the IME, as between the IME of tau_ref= 0.089 and tau_ref=0.091 a sudden drop in the calculated IME from marginally over $1.66 \pm 0.044 \times 10^5$ kg to an IME of slightly over $1.0 \pm 0.04 \times 10^5$ kg appears. This sudden drop can be

explained by a significant smaller plume mask that is taking less pixels into account and therefore results in a smaller IME.

As the plume detection finds a plume for every simulation separately, the plume mask varies for each scenario. Thus, the amount of pixels inside the plume varies significantly from 252 pixels for tau_ref values of 0.0001 and 0.001 down to 43 pixels detected as plume for a tau_ref value of 0.5. Hence, the IME is calculated per plume length (equation 5.16 and 5.17) in order to ensure the comparability between simulations. In addition, it is expected that the sudden drop from $1.66 \pm 0.044 \times 10^5$ kg to $1.0 \pm 0.04 \times 10^5$ kg disappears or at least becomes significantly smaller.

The IME per plume length, in Figure 6.8, shows values from marginally over $0.0021 \pm 0.00005 \times 10^5$ kg for small tau_ref values down to $0.0014 \pm 0.00018 \times 10^5$ kg. Between the two IME per plume length for the respective values of tau_ref of 0.089 and 0.091 the sudden drop is still visible. The IME per plume length can be categorised into three levels. The first is related to tau_ref values from 0.0001 until 0.089 with IMEs per plume length around $0.0021 \pm 0.00005 \times 10^5$ kg. The second level includes tau_ref values from 0.091 to 0.3 with IMEs per plume length around $0.0018 \pm 0.00008 \times 10^5$ kg. Then another drop for tau_ref= 0.5 down to an IME per plume length of $0.0014 \pm 0.00018 \times 10^5$ kg is visible. Furthermore, the respective error to the IME per plume length significantly rises with increasing aerosol amount. Accordingly, the IME per plume length leads to no improvement in avoiding the gap coming from different plume sizes. The difference in the automatic plume detection outweighs the visible influence of increasing aerosol amount inside the plume.

The parameters summarized in Table 6.2 are presenting the mean background value in ppm for each simulation and the mean enhancement of CO_2 inside the plume against the mean background value in ppm and kg. Furthermore, the IME and the IME per plume length and their respective errors, as well as the pixels numbers inside the plume, are listed.

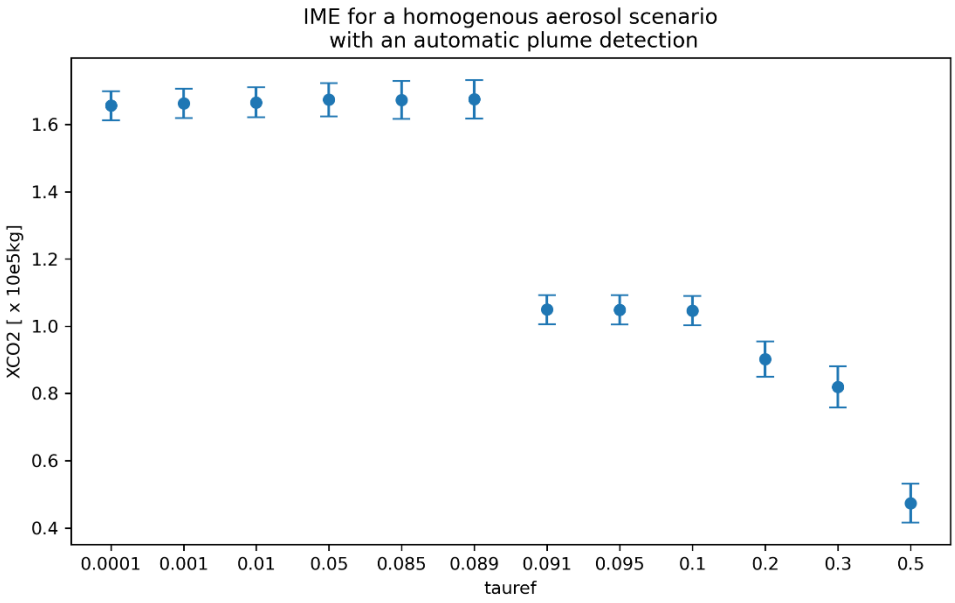

Figure 6.7: IME depending on aerosol optical thickness for the different simulations with increasing values for tau_ref. In this scenario the aerosols are homogenously dispersed over the whole scene. The IME is calculated for the scenario, where every simulation has its own detected plume mask.

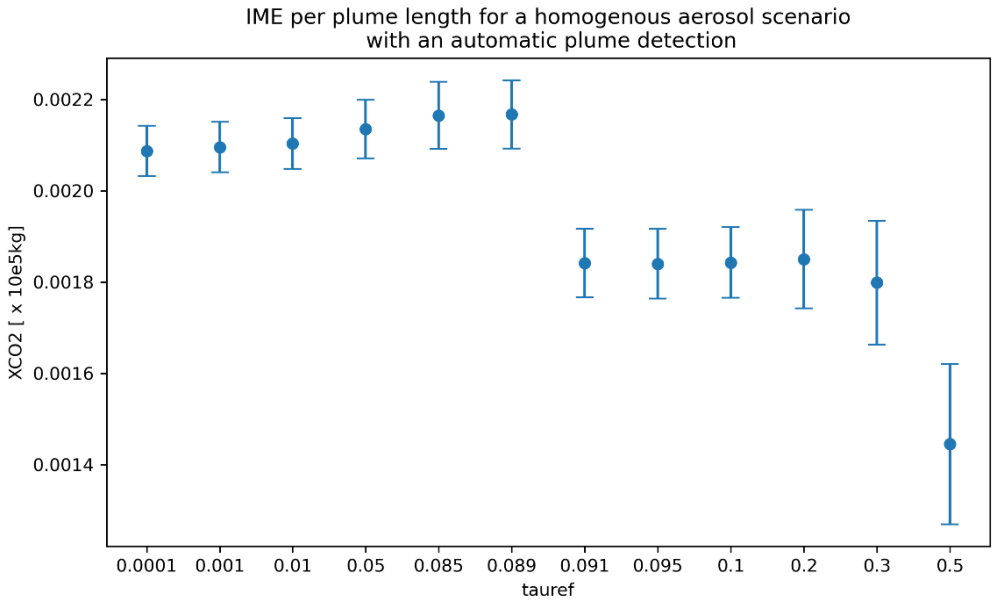

Figure 6.8: IME per plume length depending on aerosol optical thickness for the different simulations with increasing values for tau_ref. In this scenario the aerosols are homogenously dispersed over the whole scene. The IME is calculated for the scenario, where every simulation has its own detected plume mask. To ensure compatibility between the different simulation with different plume mask in size and shape the IME is divided through the plume length.

Table 6.2: Calculated parameters of the simulation with different of aerosol optical thickness (tau_ref). The parameters are calculated for an homogeneously dispersed aerosol scenario where an automatic plume detection is applied. The parameters help to make statistically correct statement on the dependency of the aerosol optical thickness.

tauref	Mean Background CO_2 [ppm]	Mean CO_2 enhancement [ppm]	mean mass enhancement [kg]	IME [x10^5 kg]	Error IME [x10^5 kg]	IME per plume length [x10^5 kg]	Error IME per plume length [x10^5 kg]	number of plume pixel
0.0001	427.9	17.4	0.263	1.657	0.044	0.00209	0.00005	252
0.001	427.8	17.5	0.264	1.663	0.044	0.00210	0.00005	252
0.01	427.3	17.6	0.266	1.666	0.044	0.00210	0.00006	251
0.05	425.0	17.9	0.271	1.674	0.050	0.00213	0.00006	246
0.085	423.1	18.5	0.279	1.673	0.057	0.00216	0.00007	239
0.089	422.9	18.5	0.279	1.675	0.058	0.00217	0.00007	239
0.091	422.8	21.4	0.323	1.050	0.043	0.00184	0.00008	130
0.095	422.7	21.4	0.323	1.049	0.043	0.00184	0.00008	130
0.1	422.3	21.5	0.324	1.046	0.044	0.00184	0.00008	129
0.2	417.2	24.9	0.376	0.902	0.053	0.00185	0.00011	95
0.3	412.5	25.5	0.386	0.819	0.062	0.00180	0.00014	83
0.5	403.6	29.2	0.441	0.474	0.057	0.00144	0.00018	43

To avoid errors coming from different plume mask shapes and sizes, the approach was made to apply the plume mask of the simulation with the tau_ref value of 0.01 on all the other simulations with increasing aerosol optical thickness. Therefore, the background to which the enhancement is compared to has close to no aerosols present in the atmosphere. While the plume mask comes from the simulation with tau_ref=0.001 and is applied to all the simulation, the aerosols are homogeneously dispersed over the whole scene with the specified value for the aerosol amount. More precisely, there is no difference inside and outside the plume regarding the aerosols. As the aerosols are homogenous over the whole scene, the mean values of the background between the simulations are different.

Figure 6.9 shows all simulations with the same plume mask. By applying the same plume mask, the mass enhancement goes from -1.0 kg up to 0.7 kg. The pixels showing the mass enhancement inside the plume ranging from positive values over zero into the negative spectrum with increasing values for the aerosol amount. The simulations with tau_ref equal to 0.3 and 0.5 appear to have dark blue pixels with values in the negative

range down to -1.0 kg. The mean enhancement of the plume against the background varies around 17.4 ppm and 17.5 ppm for all simulations with tau_ref smaller than 0.3. The simulation with the tau_ref value of 0.3 has a mean enhancement inside the plume of 17.1 ppm. With 16.3 ppm the mean enhancement for the simulation with many aerosols present in the atmosphere (tau_ref) is significantly below the enhancement of the other simulations. Accordingly, the enhancement inside the plume varies only by 1.3 ppm with increasing aerosol amount for the scenario that the plume location and size is known and the aerosols are dispersed homogenously over the whole scene.

Figure 6.10 shows the IME and its respective error for the approach of having the same plume mask for all simulations while the aerosol amount stays homogenous over the whole scene. The IMEs are very similar with values slightly above $1.65 \pm 0.044 \times 10^5$ kg for all simulations except for the ones with very high aerosol amounts (au_ref=0.3 and 0.5). The calculated IMEs with tau_ref values of 0.3 and 0.5 differ significantly with values of $1.635 \pm 0.106 \times 10^5$ kg and $1.547 \pm 0.139 \times 10^5$ kg from the other simulations. Therefore, in these cases with many aerosols over the whole scene, the retrieved CO_2 is underestimated. As the SNR is measured with homogenous dispersed aerosols over the whole scene the IME does not vary significantly. However, it should be noted that the respective error of the IME gets bigger with increasing aerosol amounts. Thus, more aerosols in the atmosphere come with higher uncertainties in quantifying the CO2.

Table 6.3 compiles the above-mentioned parameters for the case that the same plume mask is applied to all simulations and the aerosols amount is homogenously dispersed over the whole scene. The different values for the parameters of the mean background value, the mean enhancement inside the plume in ppm and kg, the IME and its error are listed.

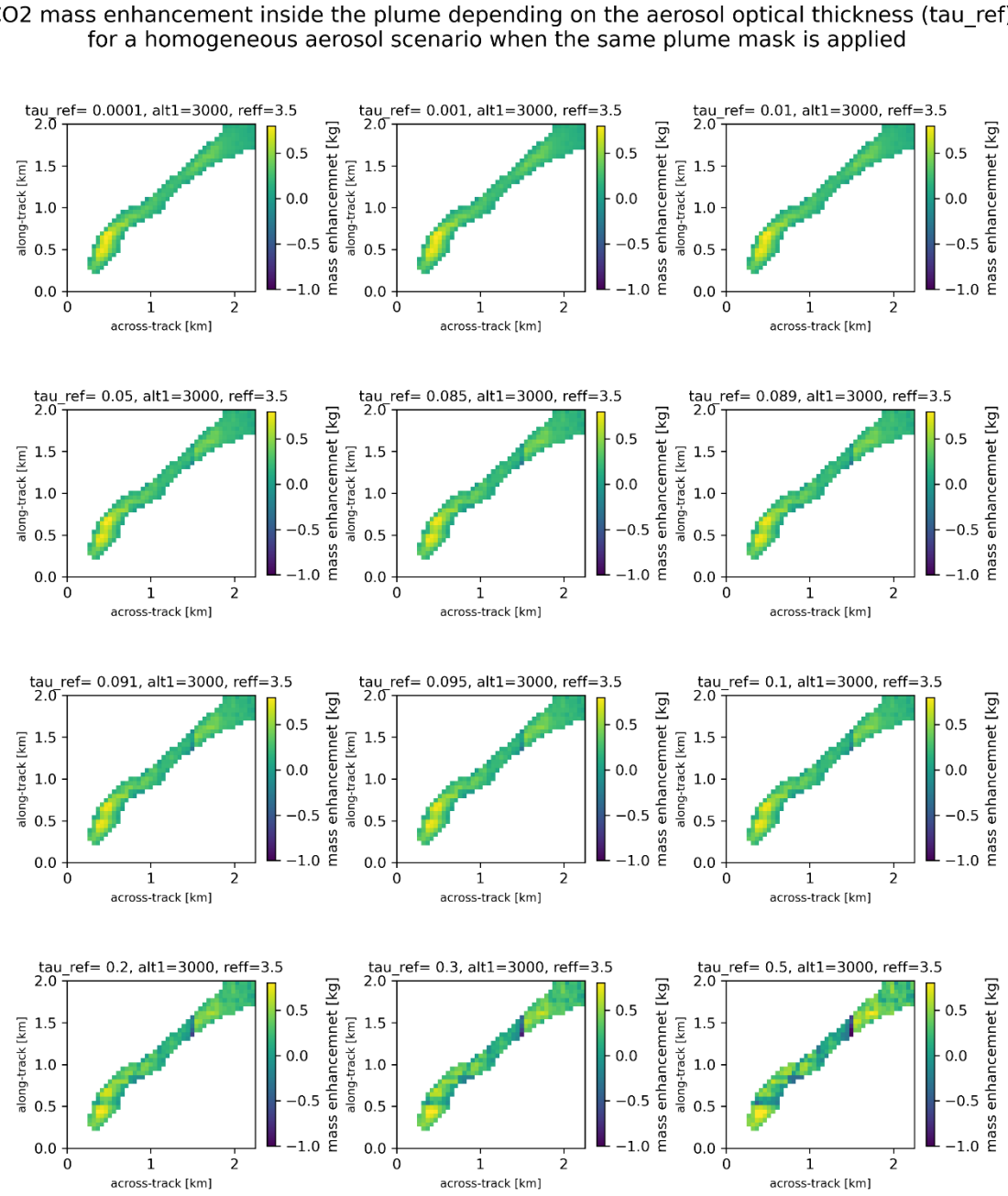

Figure 6.9: The XCO2 mass enhancement inside the plume is shown for simulations with different tau_ref values. The automatic plume mask detection of the simulation with tau_ref value 0.001 is applied for every other simulation to ensure that the plume mask is detected and the same. This makes comparison possible. Aerosols are dispersed homogenous over the whole scene.

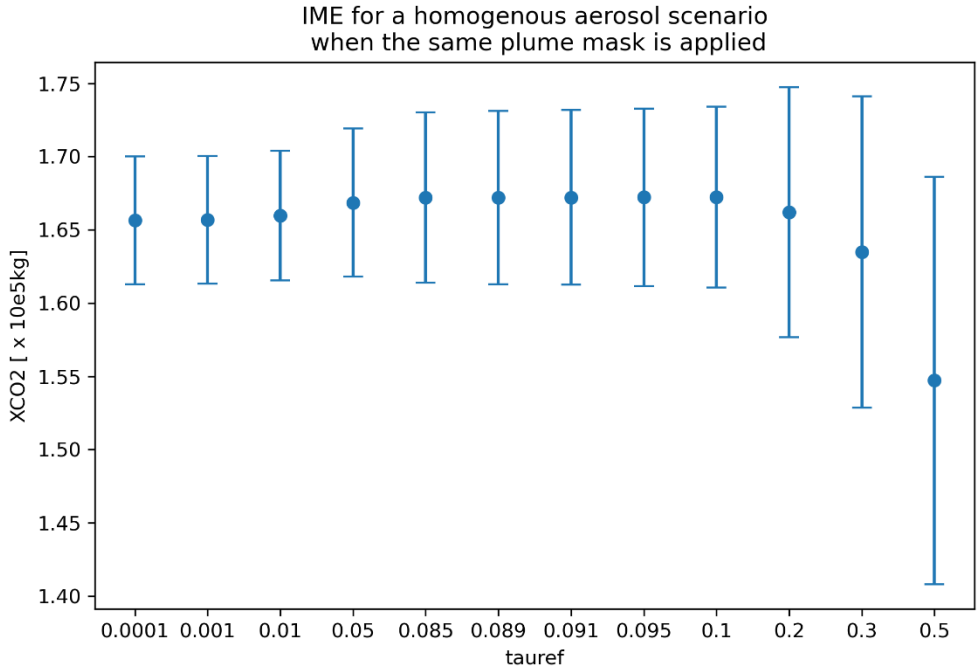

Figure 6.10: IME for the same plume mask depending on aerosol optical thickness. The aerosols are homogenously dispersed over the whole scene for the different simulations with increasing values for tau_ref. The IME is calculated for the scenario that for every simulation the plume mask of the simulation with tau_ref=0.0001 is applied. The background value varies as also there the aerosol scattering depending on tau_ref is applied.

Table 6.3: Parameters calculated for the dependence of aerosol amount when the aerosols are homogeneously dispersed over the whole scene. The same plume mask is applied to all simulations.

Tau_ref	**Mean background CO_2 [ppm]**	**Mean enhancement [ppm]**	**Mean mass enhancement plume [kg]**	**IME [x 10^5 kg]**	**IME error [x10^5 kg]**
0.0001	427.9	17.4	0.263	1.657	0.044
0.001	427.8	17.4	0.263	1.657	0.044
0.01	427.3	17.4	0.263	1.660	0.044
0.05	425.0	17.5	0.265	1.669	0.051
0.085	423.1	17.6	0.265	1.672	0.058
0.089	422.9	17.6	0.265	1.672	0.059
0.091	422.8	17.6	0.265	1.672	0.060
0.095	422.6	17.6	0.265	1.672	0.061
0.1	422.3	17.6	0.265	1.672	0.062
0.2	417.2	17.5	0.264	1.662	0.085
0.3	412.5	17.2	0.259	1.635	0.106
0.5	403.6	16.3	0.246	1.547	0.139

6.3.2 Study 2: Increasing aerosol optical thickness inside plume, low aerosol density in background

This study investigates the effect of an increase in the aerosol optical thickness inside the plume while the aerosols amount outside the plume stays low. As it is assumed that industries not only emit CO_2 but also other small particles, this is the most realistic case.

Hence, runs with increasing aerosol amounts inside the plume are made and compared to always the same background scenario with values for the aerosol optical thickness of 0.001, aerosol height distribution of 3000 m and aerosol size distribution of 3.5. Also, from this scene the aerosol plume mask is applied to all simulations like it has been done in study 1. Figure 6.11 shows the mass enhancement inside the plume for the different scenarios with increasing aerosol amount inside the plume compared to always the same mean background value of 427.9 ppm out of the scenario with very few aerosols. Also, the enhancement inside the plume for increasing tau_ref values is compared to a constant background with an aerosol amount of 0.001. The mass enhancement goes from -1.0 kg up to 0.7 kg. With increasing values of the aerosol amount the pixels showing the mass enhancement inside the plume range from positive values over zero into the negative spectrum. The simulations with tau_ref equal to 0.3 and 0.5 appear to have dark blue pixels with values in the negative range down to -1.0 kg. Having negative values already leads to the assumption that many pixels are considered inside the plume with no enhancement against the background and should therefore not be taken into account. The enhancement in ppm versus the constant background of 427.9 ppm reaches values from 17.4 ppm (tau_ref=0.001) down to -8 ppm (tau_ref=0.5). Compared to the mass enhancement of plumes with increasing aerosol amounts that are homogenously dispersed over the whole scene like in Figure 6.9, the enhancement in Figure 6.11 reaches more negative values. Hence, the IME and thus the retrieved CO_2 get more underestimated if the aerosols are not homogenously dispersed over the whole scene but have a low aerosol amount outside of the plume.

Figure 6.12 shows the IME with an increase of the aerosol optical thickness inside the plume whereas the aerosol amount outside the plume stays low. Accordingly, the background, to which the enhancement is compared to, stays constant for each calculation. With increasing values for the aerosol amount the IME constantly decreases from $1.657 \pm 0.044 \times 10^5$ kg for the tau_ref value of 0.0001 down to $-0.762 \pm 0.043 \times 10^5$ kg

for an aerosol amount of 0.5. Two levels of the IME values can be determined during the decrease. One for simulations with very few aerosols in the plume (tau1_ref= 0.0001, 0.001 and 0.01) with an IME around $1.6 \pm 0.044 \times 10^5$ kg and one for aerosol amount values between 0.085 and 0.1 with an IME around $1.18 \pm 0.043 \times 10^5$ kg. For an aerosol amount exceeding 0.1 a very strong decrease down into the minus range is investigated. This implies that the retrieved CO_2 gets significantly underestimated if the aerosol amount only increases inside the plume, especially for an aerosol amount bigger than 0.1. The respective error to the IME stays constant for all simulations. Therefore, no increasing uncertainties with increasing aerosol amounts is observed.

Table 6.4 summarizes the parameters for the mean background value in ppm, the mean enhancement inside the plume in ppm and kg and the IME and its error for the scenario that the aerosol amount increases inside the plume while outside the plume is a constant very low aerosol amount.

XCO2 mass enhancement inside the plume depending on the aerosol optical thickness (tau_ref) for a heterogeneous aerosol scenario when the same plume mask is applied

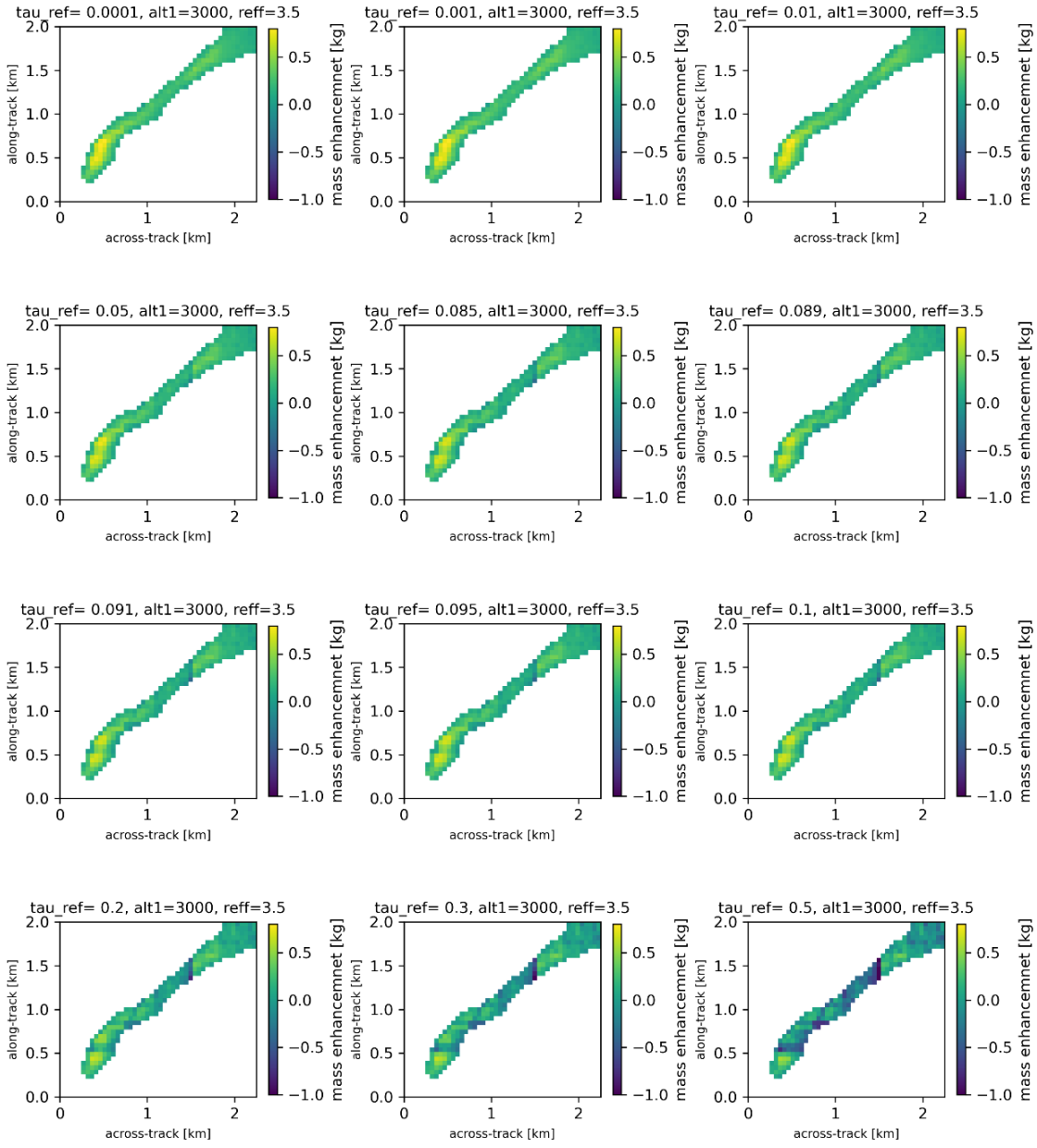

Figure 6.11: The XCO2 mass enhancement inside the plume is shown for simulations with different tau_ref values. The automatic plume mask detection of the simulation with tau_ref value 0.001 is applied for every other simulation to ensure that the plume mask is detected and the same. This makes comparison possible. The aerosol amount of the background against which the enhancement is calculated is also taken from this simulation with very few aerosols like the plume mask and therefore stays the same for all simulations with 427.9 ppm.

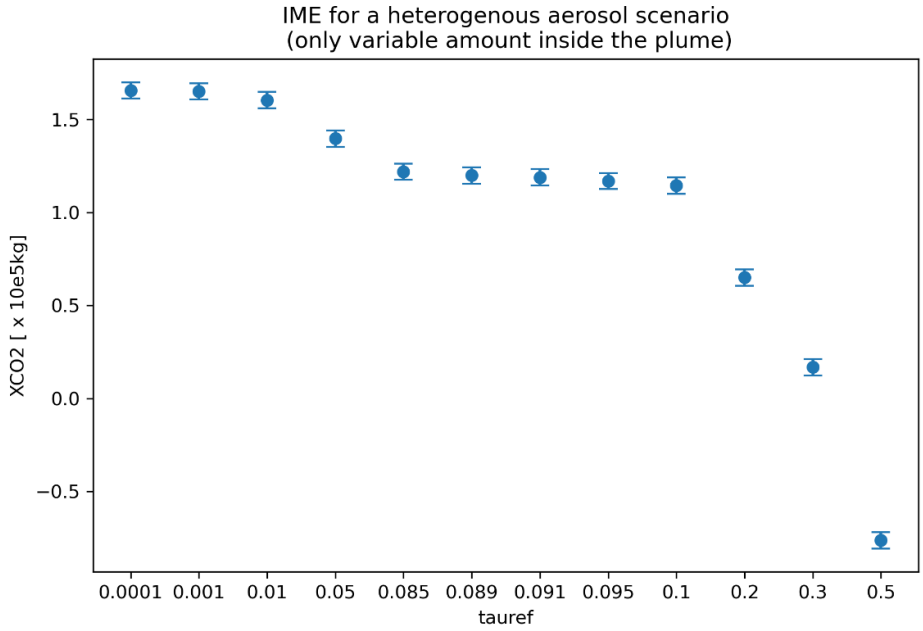

Figure 6.12: IME for the same plume mask depending on aerosol optical thickness for the different simulations with increasing values for tau_ref. In this scenario the aerosols are heterogeneously dispersed over the scene, thus the aerosol optical thickness is only changed inside the plume. The IME is calculated for the scenario that for every simulation the plume mask of the simulation with tau_ref=0.0001 is applied. Also, the background is the same for all with mean background value of the simulation with tau_ref=0.0001 with 427.9 ppm.

Table 6.4: Parameters for the dependence of the aerosol optical thickness for the heterogenous aerosol scenario. Furthermore, the same plume mask is applied to all the simulations. Therefore, the mean background values is always the same of the tau_ref =0.0001 simulation (427.9 ppm).

Tau_ref	**Mean background CO_2 [ppm]**	**Mean enhancement [ppm]**	**Mean mass enhancement plume [kg]**	**IME [x 10^5 kg]**	**IME error [x10^5 kg]**
0.0001	427.9	17.4	0.263	1.657	0.044
0.001	427.9	17.4	0.262	1.652	0.044
0.01	427.9	16.9	0.255	1.604	0.044
0.05	427.9	14.7	0.222	1.397	0.043
0.085	427.9	12.8	0.194	1.219	0.043
0.089	427.9	12.6	0.190	1.199	0.043
0.091	427.9	12.5	0.189	1.189	0.043
0.095	427.9	12.3	0.186	1.169	0.043
0.1	427.9	12.0	0.182	1.144	0.043
0.2	427.9	6.8	0.103	0.650	0.043
0.3	427.9	1.8	0.027	0.168	0.043
0.5	427.9	-8.0	-0.121	-0.762	0.043

6.3.3 Study 3: Increasing aerosol height distribution for a homogeneously dispersed aerosol scenario

This study presents the results of the influence of increasing aerosol height distribution on the quantification of CO_2. The steps taken to evaluate the influence of the aerosol height distribution are the same as in study 1. Different simulations with the values 0 m, 500 m, 1500 m, 3000 m, 5000 m, 8000 m and 12000 m for alt1 are performed.

Figure 6.13 shows the retrieved CO2 of each pixel for different simulations with increasing aerosol height distributions on the left column. Yellow pixels show higher CO_2 values and mark the emission plume. With increasing values for alt1 the CO_2 values are getting darker what shows a decrease in the retrieved CO_2. For the simulation with an aerosol height of 5000 m, 8000 m and 12000 m no coherent plume with higher CO_2 values is visible from the colouring of the pixels. The middle column presents the XCO_2 error which is growing significantly bigger with increasing aerosol height distribution. The simulations with alt1 values of 0 m, 500 m and 1500 m show only positive errors up to 22 ppm. The simulation with an aerosol height of 3000 m displays values in the negative and positive range (± 20 ppm), whereas simulations with aerosols higher than 3000 m have mainly errors in the negative range with values up to 110 ppm. This indicates that in higher altitude the retrieved CO_2 gets mostly underestimated, while in lower altitude the retrieved CO_2 gets overestimated. The right column shows the correlation of the XCO_2 error versus the albedo values for each pixel. With increasing aerosol height, the correlation between the XCO_2 error and the surface albedo gets stronger. For a small aerosol height (smaller than 1500 m) low albedo values correlate with less negative XCO_2 errors than high albedo values. This signifies that the retrieved CO_2 gets more overestimated for brighter surfaces.

To validate this first impression, the enhancement inside the plume is calculated. Hence, an automatic plume mask detection is applied for each simulation. Figure 6.14 shows the mass enhancement inside the plume for different aerosol heights. The plume mask differs in size and shape for each simulation as the algorithm has problems finding the whole plume for simulations with aerosols in greater height. The mean background value, to which the enhancement is compared to, drops down from 427.5 ppm of the simulation at 0 m, over 422.3 ppm at 3000 m, down to 394.4 ppm in an aerosol height of 12000 m. The enhancement in ppm increases from 17.7 ppm (alt1= 0) up to 31. ppm

(alt1=12000). The increase in enhancement can be explained with a smaller plume size which only detects one coherent plume and therefore does not take many low enhancement pixels into account.

From the mass enhancement per pixel the IME of the whole plume against the mean value of the defined background is calculated. To be able to compare the IME even if the plume masks have different sizes the IME per plume length is calculated. Figure 6.15 presents the IME per plume length depending on the aerosol size distribution. The IME per plume length depending on the aerosol height can be grouped into three levels. The IME per plume length starts with $0.0021 \pm 0.0001 \times 10^5$ kg for the aerosol heights of 0m, 500m and 1500m. Then there is a significant drop down to an IME per plume length around $0.00185 \pm 0.00015 \times 10^5$ kg for the aerosol heights of 3000 m, 5000 m and 8000 m. The lowest IME per plume length is for the aerosol heights of 12000 m with a value of $0.0015 \pm 0.002 \times 10^5$ kg. Since between these three levels is also a significant change in the pixels which are counted to the plume it is assumed that the change of the IME per plume length is still mostly coming from the change in the plume size.

Table 6.5 summarizes the parameters for each simulation with increasing aerosol heights. It shows the values for the mean background value in ppm, the mean enhancement inside the plume in ppm and kg, the IME and its error, as well as the IME per plume length, and the respective error and the number of pixels of the plume mask.

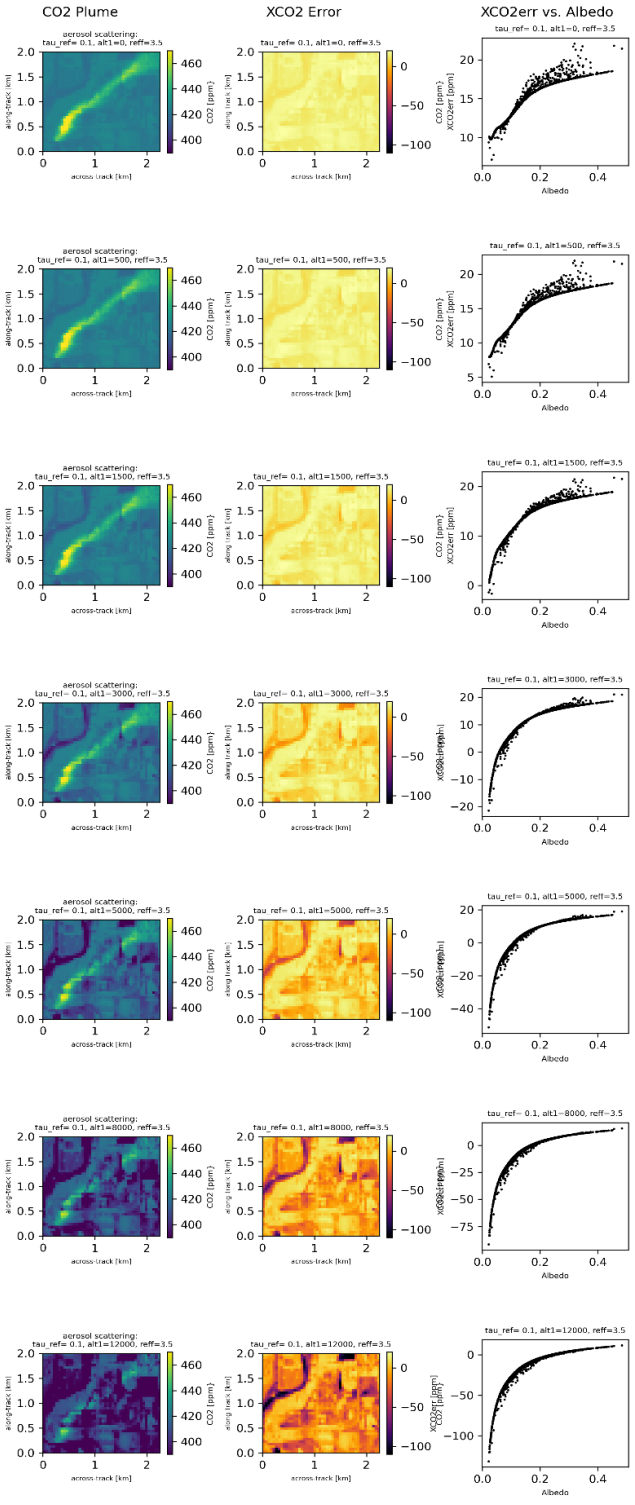

Figure 6.13: CO2 plume, XCO2 error and its correlation to albedo values for simulations with different values for the aerosol height distribution (alt1). The values for alt1 are 0, 500, 1500, 3000, 5000, 8000 and 12000 m. The aerosol optical thickness is constant with tau_ref=0.1 for every simulation. Also, the aerosol size distribution (reff) has a constant value of 3.5 for each simulation of varying values for alt1.

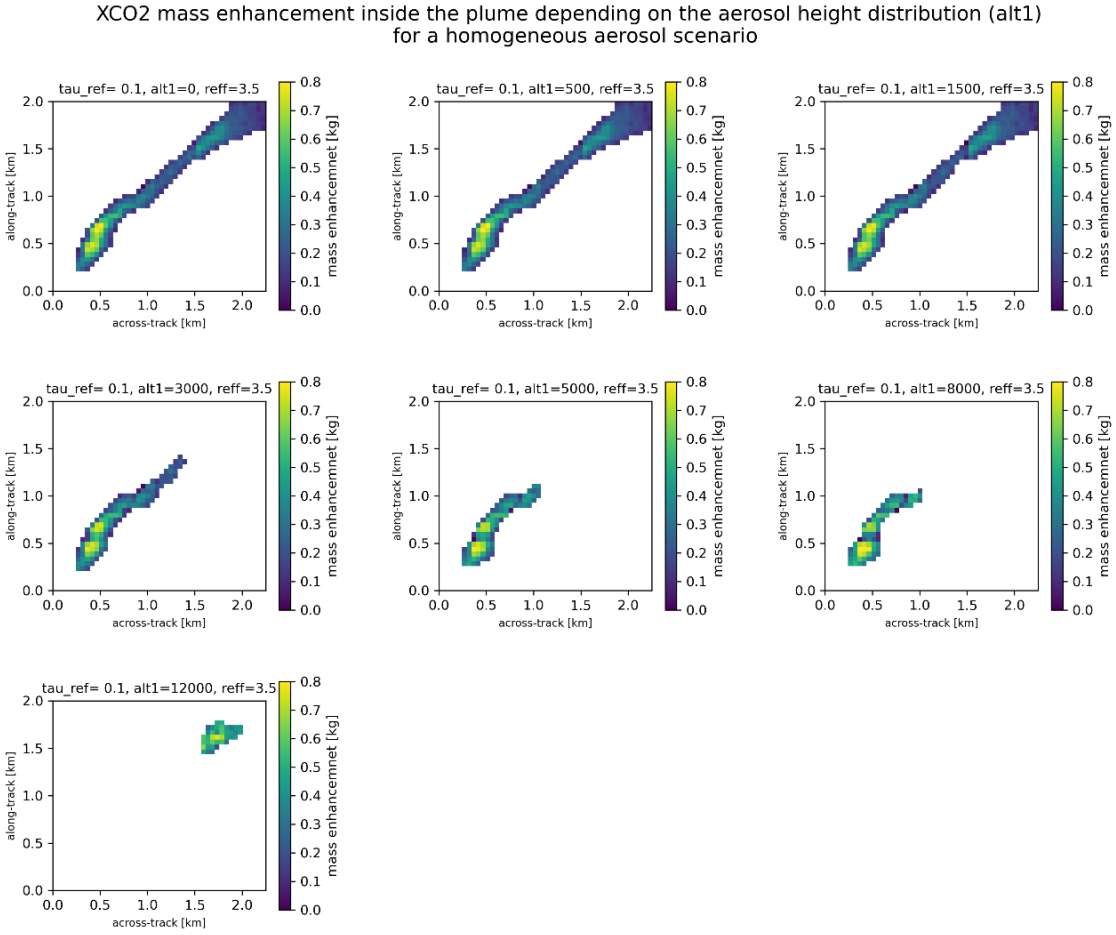

Figure 6.14: The mass enhancement of the XCO2 values inside the plume for different simulations with different alt1 values is shown. The automatic plume mask is applied for every simulation separately. Therefore, every plume mask has a different size and shape depending on the enhancement of each pixel against the mean background value.

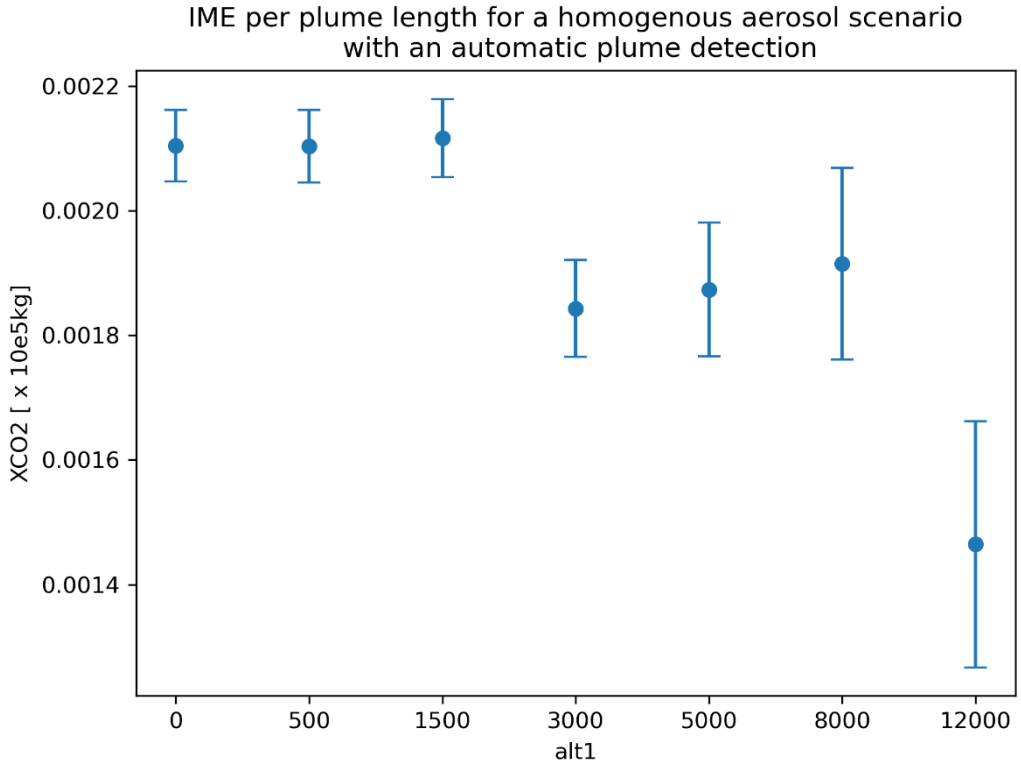

Figure 6.15: IME per plume length depending on aerosol height distribution for the different simulations with increasing values for alt1. In this scenario the aerosols are homogenously dispersed over the whole scene. The IME is calculated for the scenario, where every simulation has their own detected plume mask. As then the plume mask for every simulation is different in size and shape, the IME is divided through the plume length. This makes the different calculated IME comparable to each other.

Table 6.5: Parameters for the dependence on aerosol height distribution. The aerosols are homogenously dispersed over the whole scene. The automatic plume detection is applied to every simulation and thus the plume differs in size and shape between the simulations.

Alt 1	**Mean Background CO2 [ppm]**	**Mean CO2 enhancement [ppm]**	**mean mass enhancement [kg]**	**IME [x10^5 kg]**	**Error IME**	**IME per plume length [x10^5 kg]**	**Error IME per plume length [x10^5 kg]**	**number of plume pixel**
0	427.5	17.7	0.267	1.660	0.045	0.0021	0.0001	249
500	427.2	17.6	0.265	1.666	0.046	0.0021	0.0001	251
1500	426.0	17.7	0.268	1.667	0.049	0.0021	0.0001	248
3000	422.3	21.5	0.324	1.046	0.044	0.0018	0.0001	129
5000	415.7	25.6	0.386	0.908	0.052	0.0019	0.0001	94
8000	405.4	27.5	0.415	0.862	0.069	0.0019	0.0002	81
12000	394.4	31.0	0.469	0.457	0.062	0.0015	0.0002	39

To be able to compare the different simulations and the IME and thus be able to make valid statements about the influence of the aerosol height distribution on the quantification of CO_2, the same plume mask is applied for all simulations. Figure 6.16 presents the mass enhancement inside the plume if the plume size and shape is known and is the same for all simulations. In the following case the aerosols are homogenous dispersed over the whole scene. Hence, the mean background value to which the CO_2 values in the plume are compared to, is different for each case. As already stated in study 1, the mean background value is the same as in the case of changing the plume mask for simulations with increasing aerosol height distributions, as the background is a defined area which does not change (see Figure 5.4).

The mass enhancement inside the plume already shows a wide range between the pixels in simulations with a high aerosol altitude. The pixels for simulations with an aerosol height of 5000 m or higher range from 0.75 kg enhancement down to -1.0 kg. Therefore, in this simulation pixels which are not enhanced compared to the background are also considered to the plume mask. Simulations with lower altitude than 5000 m show a more homogenous mass enhancement inside the plume between 0 kg and 0.75 kg. However, these simulations show less pixels with 0.5 kg or more mass enhancement than simulations with aerosols present in greater height. The enhancement inside the plume is always calculated against the mean background value. As the aerosols are homogenously dispersed over the whole scene, the background value changes for each simulation. The simulation at 0 m has with 427.5 ppm the highest value of all simulations. With increasing aerosol height, the mean background value decreases down to 394.5 ppm for an altitude of 12000 m. The enhancement inside the plume against the respective mean background value is very similar for all simulations. It varies from 17.4 ppm for the simulation with aerosols on the ground level up to 19 ppm for the simulation with aerosols at a height of 12000 m. Thus, the enhancement varies by only 1.6 ppm with increasing aerosol height.

To see the enhancement towards the background for the whole plume and have a comparable parameter, the IME is calculated. Figure 6.17 shows the IME depending on the increase in the aerosol height distribution when the same plume mask is applied to every single simulation. Furthermore, the aerosols are homogeneously dispersed over the whole scene with no difference inside and outside the plume regarding the aerosols. With an increasing altitude where the aerosols are present the IME increases from 1.656 ±

0.045 x 10^5 kg (alt1=0) up to 1.807 ± 0.157 x 10^5 kg (alt1=12000). Also, the respective error to the IME increases significantly. This indicates that the uncertainties in the quantification of the retrieved CO_2 grow with increasing altitude.

Table 6.6 gives the overview of the mentioned parameters for every simulation depending on the aerosol height for the case that the aerosols are dispersed homogenously over the whole scene. The parameters listed for every simulation separately are the mean background value in ppm, the mean enhancement in ppm and kg, as well as the IME and its respective error.

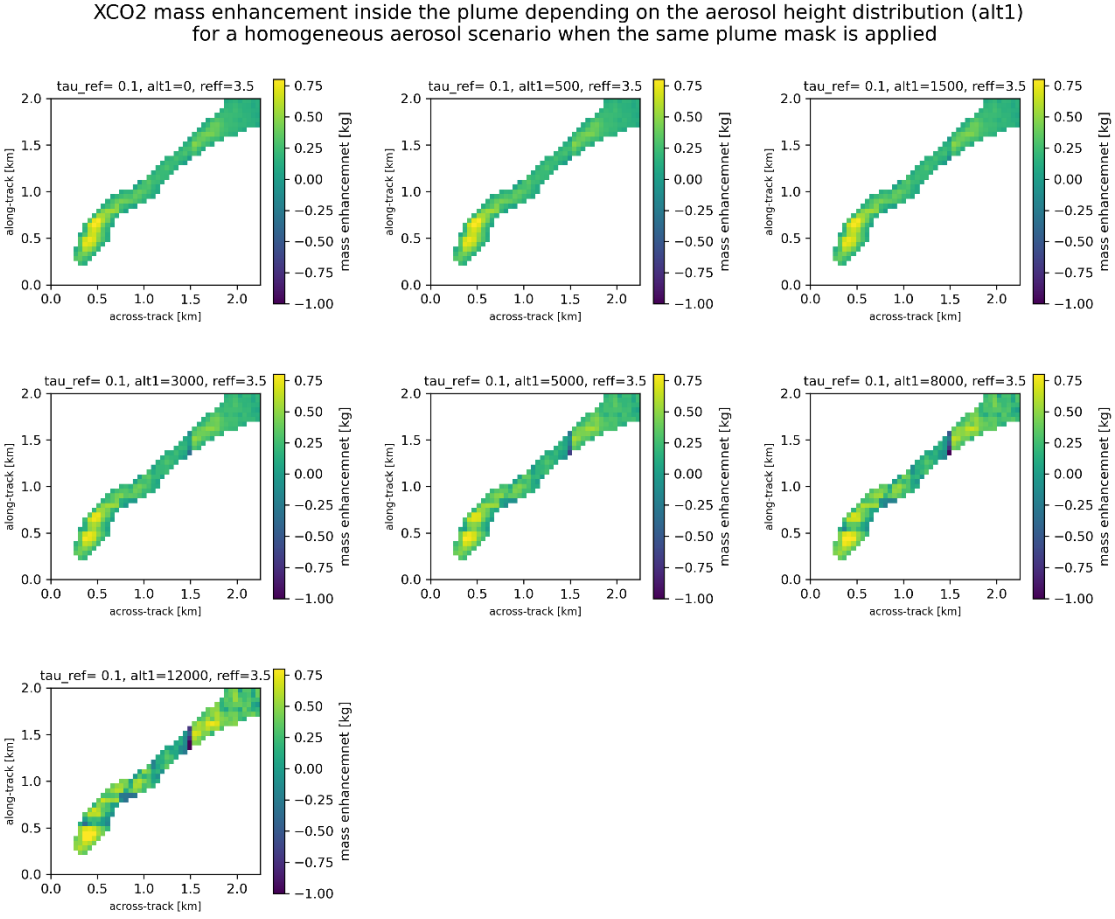

Figure 6.16: The XCO_2 mass enhancement inside the plume is shown for simulations with different values. The automatic plume mask detection of the simulation with tau_ref value 0.001 is applied for every other simulation to ensure that the plume mask is completely detected and has the same size and shape for every simulation. This makes comparison possible. Aerosols are dispersed homogenous over the whole scene.

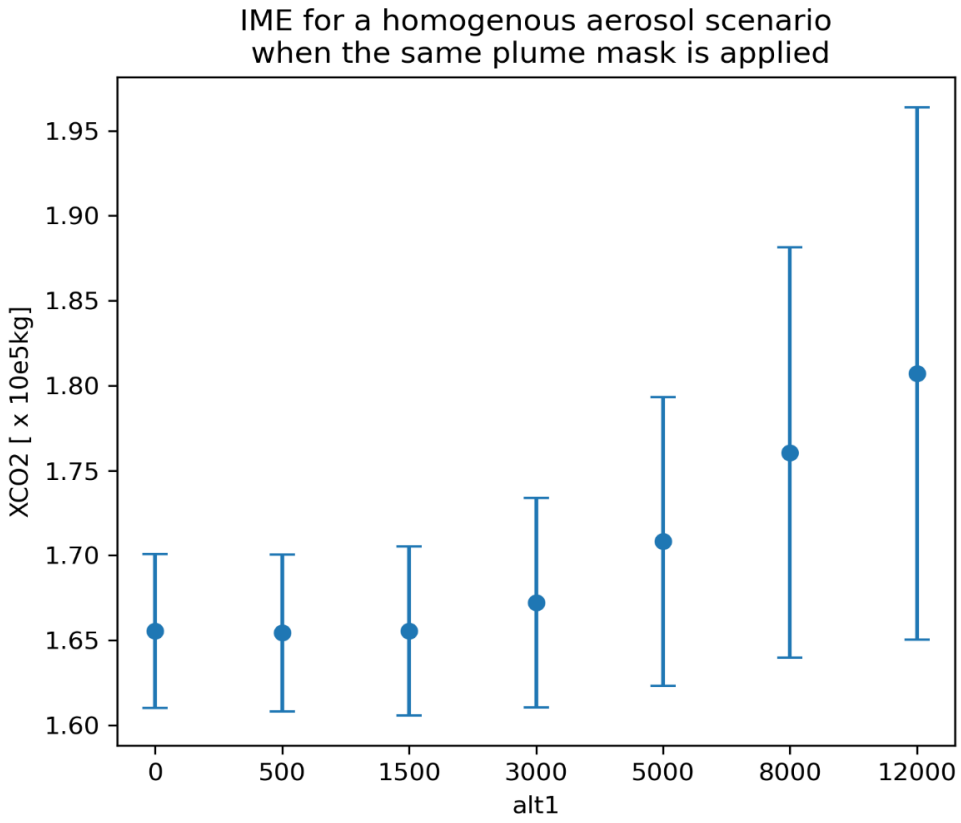

Figure 6.17: IME for the same plume mask depending on aerosol height distribution. The aerosols are homogeneously dispersed over the whole scene for the different simulations with increasing values for alt1. The IME is calculated for the scenario that for every simulation the plume mask of the simulation with tau_ref=0.0001 is applied. The background value varies as also there the aerosol scattering depending on alt1 is applied.

Table 6.6: Parameters for the dependence on aerosol height distribution. The aerosols are homogenously dispersed over the whole scene. The IME is calculated for the scenario that for every simulation the plume mask of the simulation with tau_ref=0.0001 is applied. The background value varies as also there the aerosol scattering depending on the varying alt1 value is applied.

alt1	**mean background CO_2 [ppm]**	**mean enhancement [ppm]**	**Mean enhancement mass [kg]**	**IME [x10^5 kg]**	**Error IME [x10^5 kg]**
0	427.5	17.4	0.263	1.656	0.045
500	427.1	17.4	0.263	1.654	0.046
1500	425.9	17.4	0.263	1.656	0.050
3000	422.3	17.6	0.265	1.672	0.062
5000	415.7	17.9	0.271	1.708	0.085
8000	405.4	18.5	0.279	1.761	0.121
12000	394.4	19.0	0.287	1.807	0.157

6.3.4 Study 4: Increasing aerosol height distribution inside plume, outside plume very less aerosols

Study 4 presents the case that the aerosol height distribution increases inside the plume but outside the plume the aerosol amount stays constantly low. The same procedure as in study 2 for increasing aerosol amount is executed. Furthermore, the background values and the plume mask come from the same simulation as in study 2 with tau_ref=0.0001, alt1=3000 and reff=3.5.

Figure 6.18 presents the mass enhancement inside the plume compared to a constant background for all simulations depending on an increase in the aerosol height. The plots show that with increasing aerosol height the mass enhancement gets lower and even reaches negative values. The enhancement compared to the background reaches values from 0.75 kg down to -1.0 kg per pixel. Pixels with negative values in the mass enhancement signify that there is no enhancement when comparing the pixels inside the plume against the mean background value. The mean background value to which the enhancement for all simulations is compared to is 427.9 ppm. This is the mean background value when there are very few aerosols present in the atmosphere. The enhancement inside the plume decreases from 17 ppm at ground level going down to 12 ppm for an aerosol height of 3000 m, into a negative range. The enhancement at 1200 m against the background is -14.518. To make valid statements about the enhancement of the whole plume, the IME is calculated and presented in Figure 6.19. The IME decreases from $1.621 \pm 0.0043 \times 10^5$ kg down to $-1.382 \pm 0.043 \times 10^5$ kg at an aerosol height of 12000 m for the scenario that aerosols are at the ground level. A deep drop is observed at an aerosol height of 3000 m from $1.144 \pm 0.043 \times 10^5$ kg down to $0.548 \pm 0.043 \times 10^5$ kg at 5000 m. The respective error to the IME and therefore the uncertainties are the same for each simulation and do not change with increasing aerosol heights. The IME shows that with increasing aerosol heights the retrieved CO_2 gets underestimated. Moreover, for simulations with great aerosol heights like 8000 m and 12000 m there is no enhancement compared to a mean background value with very few aerosols present in the atmosphere.

Table 6.7 summarizes the values of the parameters mean background value in ppm, mean enhancement in ppm and kg, as well as the IME and the respective error for each simulation with increasing aerosol heights inside the plume while the background has very few aerosols.

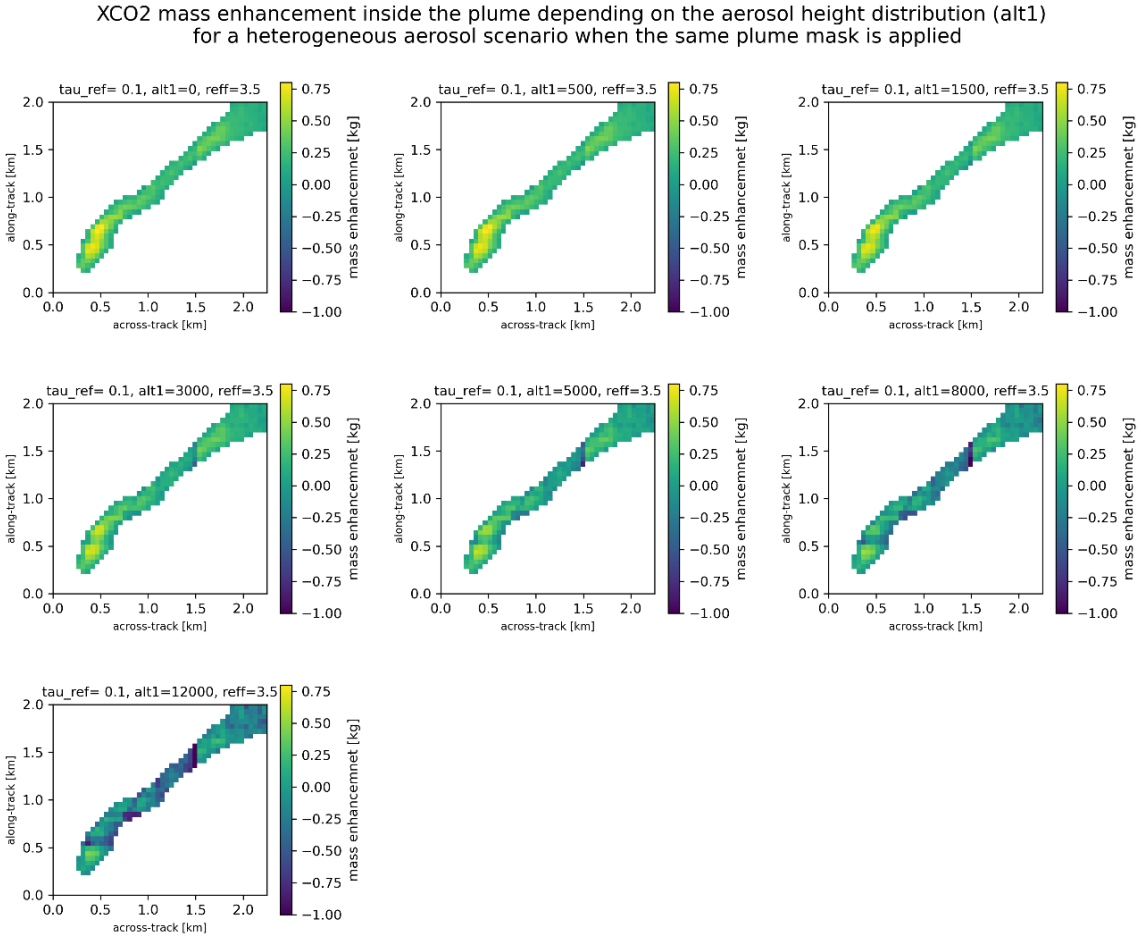

Figure 6.18: The XCO2 mass enhancement inside the plume is shown for simulations with different values for the aerosol height distribution. The automatic plume mask detection of the simulation with tau_ref value 0.001 is applied for every other simulation to ensure that the plume mask is detected and the same. This makes comparison possible. The aerosol amount of the background against which the enhancement is calculated is also taken from this simulation with very few aerosols and aerosols in a height of 3000 m like the plume mask and therefore stays the same for all simulations with 427.9 ppm.

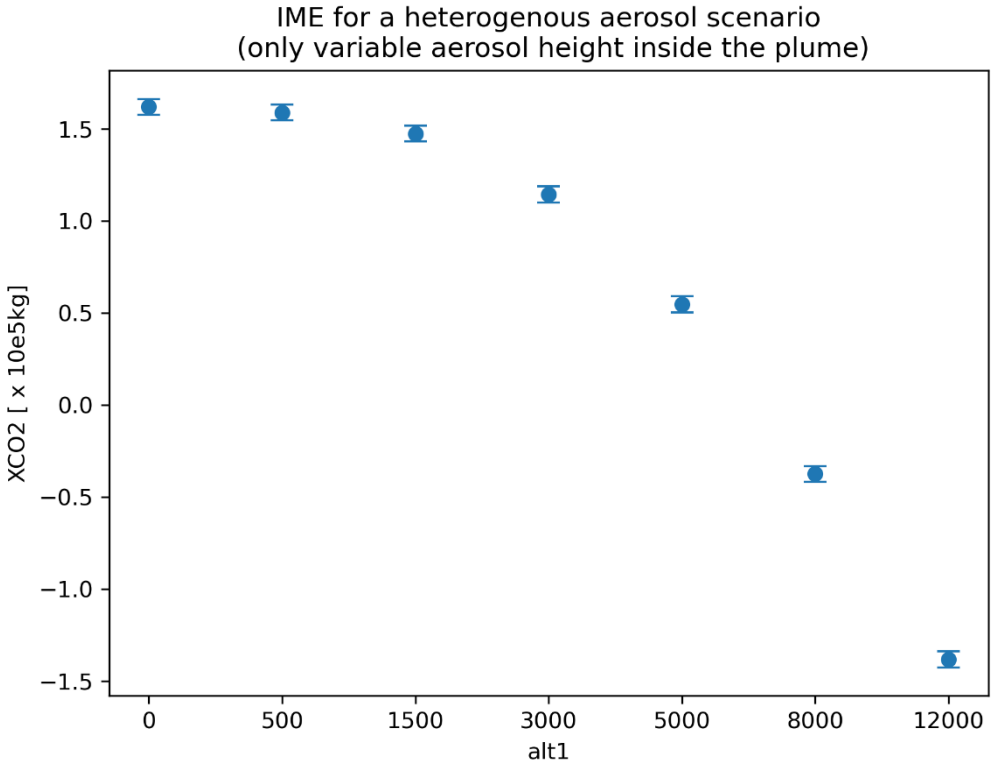

Figure 6.19: IME for the same plume mask depending on the aerosol height distribution. The IME is calculated for the scenario that for every simulation the plume mask of the simulation with tau_ref=0.0001 is applied. Also, the background is the same for all with mean background value of the simulation with tau_ref=0.0001 with 427.9 ppm.

Table 6.7: Parameters for the dependence of the aerosol height distribution for the heterogenous aerosol scenario. Furthermore, the same plume mask is applied to all the simulations. Therefore, the mean background values are always the same of the tau_ref =0.0001 simulation (427.9 ppm).

alt1	**mean background CO_2 [ppm]**	**mean enhancement [ppm]**	**Mean mass enhancement [kg]**	**IME [x10^5 kg]**	**Error IME [x10^5 kg]**
0	427.9	17.0	0.257	1.621	0.043
500	427.9	16.7	0.252	1.590	0.043
1500	427.9	15.5	0.234	1.475	0.043
3000	427.9	12.0	0.182	1.144	0.043
5000	427.9	5.8	0.087	0.548	0.043
8000	427.9	-3.9	-0.060	-0.375	0.043
12000	427.9	-14.5	-0.219	-1.382	0.043

6.3.5 Study 5: Influence of increasing aerosol size for a homogeneously dispersed aerosol scenario

This study presents the influence of the aerosol size distribution on quantifying CO_2 emissions in the CO2Image mission. In this case the aerosols are dispersed homogeneously over the whole scene. Different simulations with increasing aerosol sizes been made and evaluated. The values for the aerosol sizes are 2.5, 3.5, 4.5 and 5.5. Thereby, it should be noted that small values for the aerosol size distribution signify aerosols with a big radius according to equation 5.4 (Butz et al., 2009).

Figure 6.20 shows the retrieved CO2 for each pixel for the four simulations with the different values for the aerosol size distribution (left column). The colour scale is set to 380 ppm until 470 ppm for all four scenarios, with yellow pixels marking the highest retrieved CO_2 values. It should receive attention that the highest plot has the lowest reff value, although this is the simulation with the aerosols having the biggest radius. The left column shows that big aerosols (reff=2.5 and 3.5) lead to lower values in the retrieved CO_2 than the scenarios with smaller radius of the aerosols. Hence, the upper two plots with aerosols that are big in size appear darker. In these two scenarios a coherent plume is not that clearly visible anymore. The middle column presents the XCO_2 values for each pixel. The errors reach values from -40 ppm up to 20 ppm. With increasing radius of the aerosols, the XCO_2 error show more negative values. The lower two plots with values for the aerosol size distribution of 4.5 and 5.5 (small aerosols) show XCO_2 values mainly in the positive range. Positive values imply that the retrieved CO_2 gets overestimated, whereas negative values show an underestimation of the retrieved CO_2 for this individual pixel. The right column displays the correlation between the XCO_2 error and the surface albedo for each pixel. The x-axis shows the surface albedo and the y-axis gives the XCO_2 error in ppm. It can be observed that the correlation between XCO_2 error and surface albedo is stronger for big aerosols. Furthermore, with increasing surface albedo, the XCO_2 error decreases into a more positive range up to 20 ppm for all four simulations with varying aerosol sizes. This means that the retrieved CO_2 gets more overestimated for bright surfaces. For the simulation with big aerosols (reff=2.5) low albedo values correlate with negative XCO_2 errors and with increasing albedo values the XCO_2 error increases up to 20 ppm. This indicates that for scenarios with big aerosols over the whole

scene the retrieved CO_2 gets underestimated for very dark surfaces and overestimated for albedo values greater than 0.1.

Figure 6.21 presents the mass enhancement inside the plume when the automatic plume detection is applied. The enhancement per pixel in kg reaches values between 0 kg and 0.8 kg. The enhancement is always calculated against a defined background. For the two scenarios with bigger aerosol sizes (reff= 2.5 and 3.5) the automatic plume detection is not able to find the whole plume. The mean background value varies from 425.1 ppm for small aerosols down to 417.3 ppm for the simulation with reff=2.5. The mean enhancement is 17.7 ppm and 17.9 ppm for reff=5.5 and reff=4.5, whereas the mean enhancement for bigger aerosols is 21.4 ppm (reff=3.5) and 24.7 ppm (reff=2.5). However, the automatic plume detection accounts less pixels to the plume, as it is not possible to find the whole coherent plume. This leads to a significant lower mean enhancement in ppm for big aerosols. As next evaluation step of the influence of the aerosol size on the quantification of CO_2 the IME per plume length is calculated and presented in Figure 6.22 to make statistical valid statements about the influence of the aerosol size on the quantification of CO_2. The plot shows the IME per plume length, with its respective error. The x-axe shows the value for the aerosol size, while the y-axe gives the enhancement of the retrieved CO_2 for the area of the plume mask in kg. The first thing that stands out is the two levels of the IME per plume length with one level around $0.0021 \pm 0.0001 \times 10^5$ kg for smaller aerosol sizes and one level around $0.0018 \pm 0.0001 \times 10^5$ kg for bigger aerosol sizes. These two levels can be explained through the different plume sizes as the automatic plume detection finds 250 pixels as a plume for very small aerosols (reff=5.5) and only 97 pixels for simulations with big aerosols. Apparently, calculating the IME per plume length does not bring the expected effect. The influence of a smaller plume still prevails and therefore the IME is smaller for simulations with big aerosols. Hence, the retrieved CO_2 gets underestimated significantly for simulations with bigger aerosols.

Table 6.8 presents the overview of the mean background value in ppm, the mean enhancement inside the plume in ppm and kg, the IME and the respective error, as well as the IME per plume length and its error for all simulations with increasing aerosol size. Furthermore, the number of pixels, which are accounted to the plume from the automatic plume detection, is given.

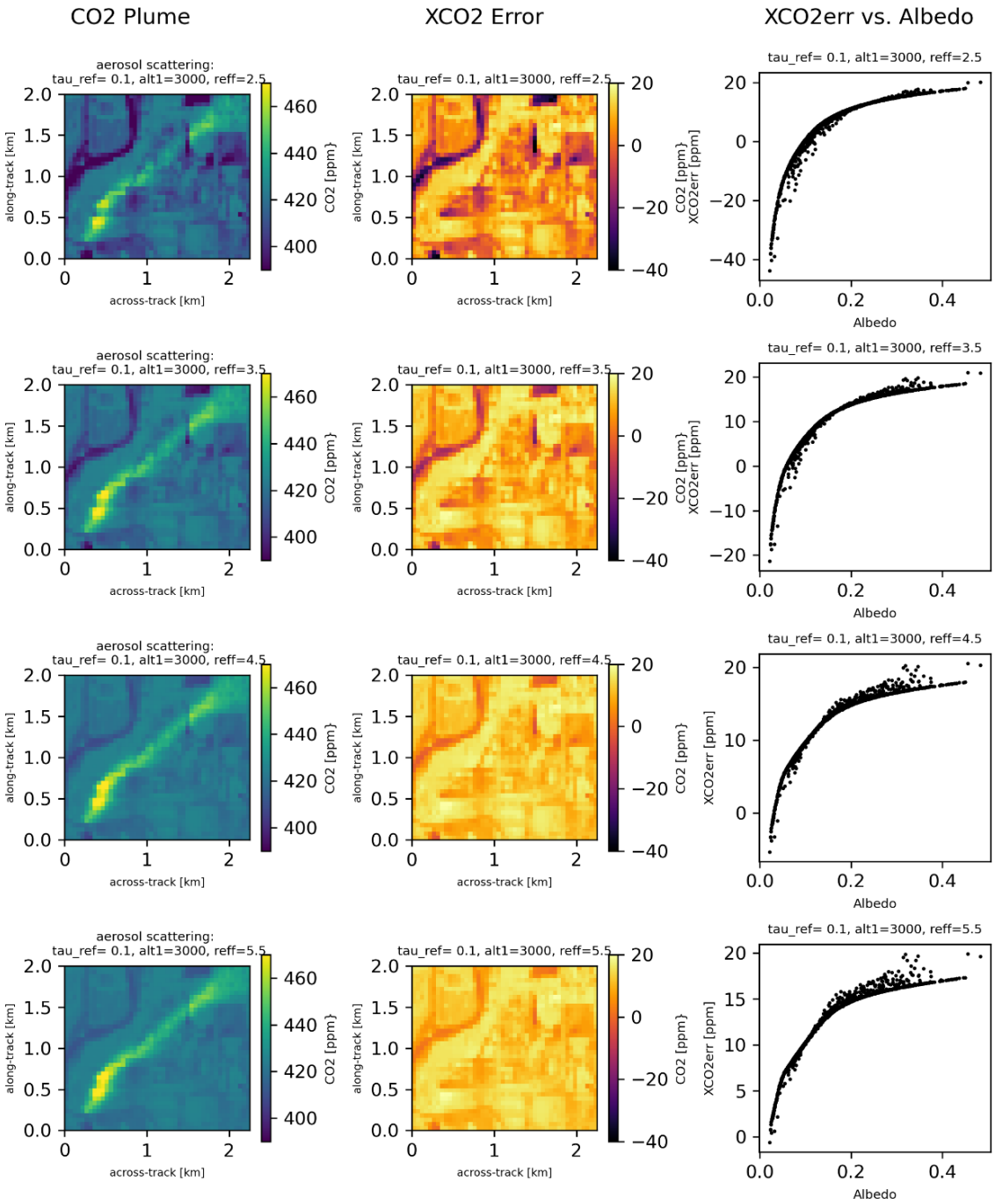

Figure 6.20: CO2 plume, XCO2 error and its correlation to albedo values for simulations with different values for the aerosol size distribution (reff). The values for alt1 are 2.5, 3.5, 4.5, 5.5. The aerosol optical thickness is constant with tau_ref=0.1 for every simulation. Also, the aerosol height distribution (alt1) has a constant value of 3000m for each simulation of varying values for alt1. The left column shows the retrieved CO2 per pixel. Furthermore, the XCO2 error (middle) and the error versus the surface albedo for each pixel (right) is shown.

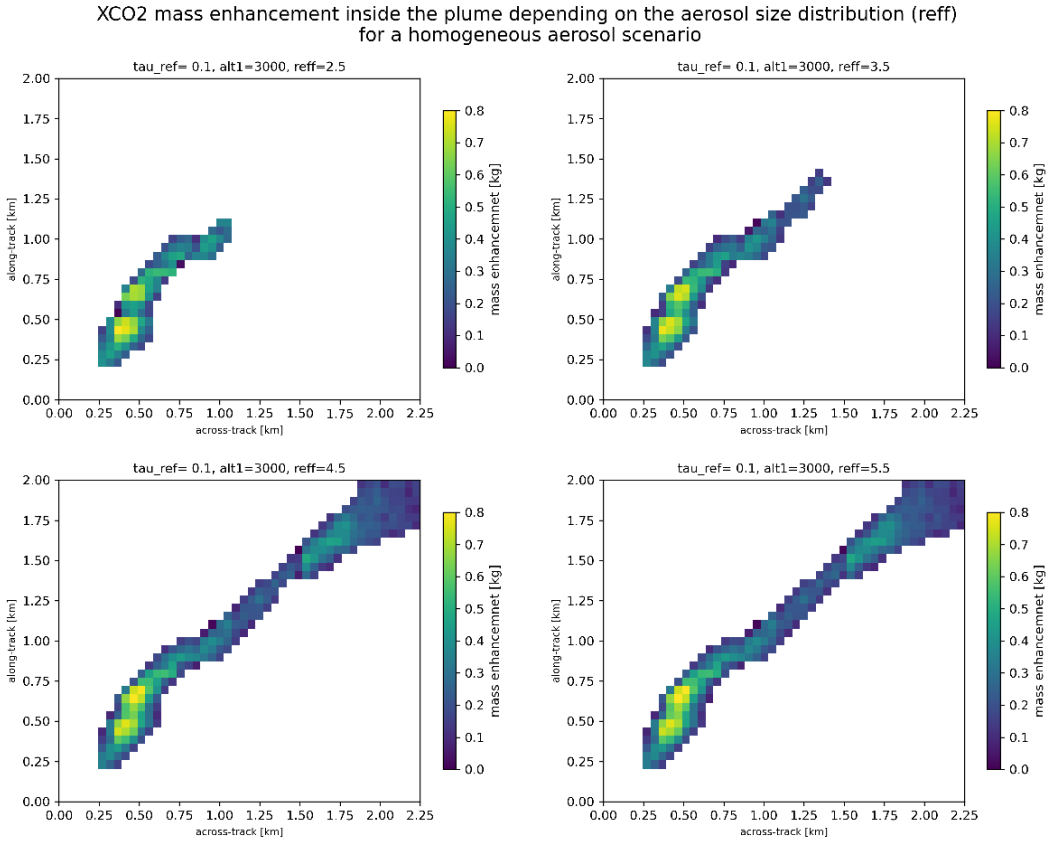

Figure 6.21: The mass enhancement of the XCO2 values inside the plume for different simulations with different values for the aerosol size distribution is shown. The automatic plume mask is applied for every simulation separately. Therefore, every plume mask has a different size and shape depending on the enhancement of each pixel against the mean background value.

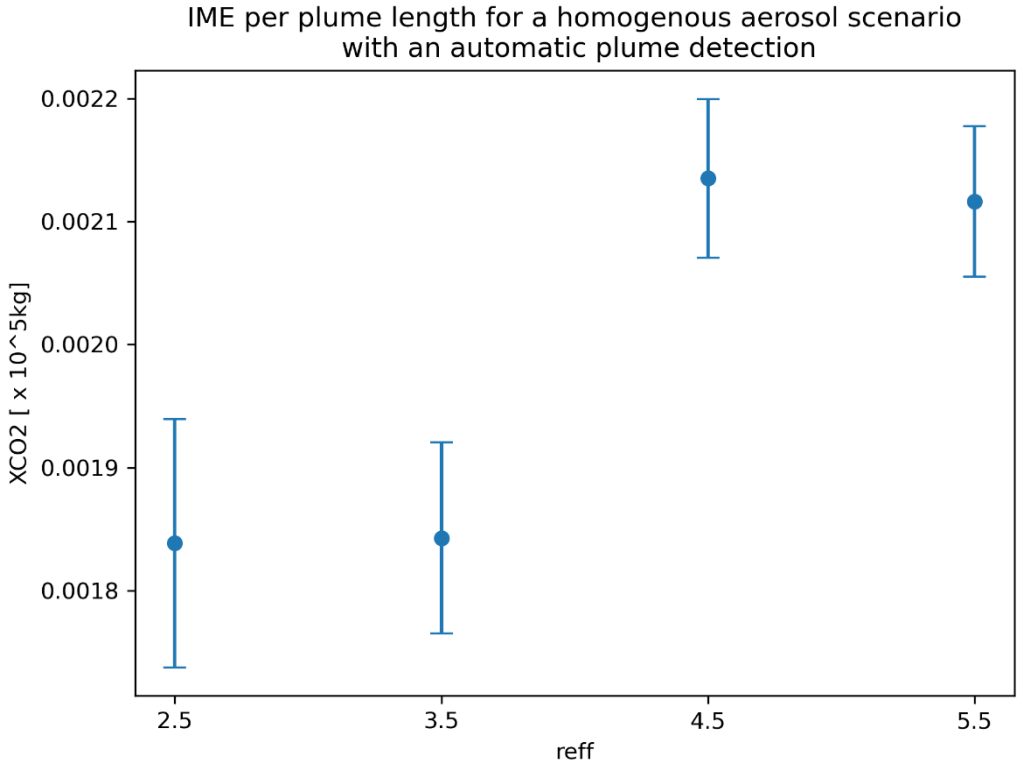

Figure 6.22: IME per plume length depending on aerosol size distribution for the different simulations with increasing values for reff. In this scenario the aerosols are homogeneously dispersed over the whole scene. The IME is calculated for the scenario, where every simulation has their own detected plume mask. As then the plume mask for every simulation is different in size and shape, the IME is divided through the plume length. This makes the different calculated IME comparable to each other.

Table 6.8: Parameters for the dependence on aerosol height distribution. The aerosols are homogenously dispersed over the whole scene. The automatic plume detection is applied to every simulation and thus the plume differs in size and shape between the simulations.

reff	mean background CO_2 [ppm]	mean enhancement [ppm]	mean mass enhancement [kg]	IME [x10^5 kg]	Error IME [x10^5 kg]	IME per plume length	Error IME per plume length [x10^5 kg]	Number of plume pixel
2.5	417.3	24.7	0.373	0.905	0.050	0.0018	0.0001	97
3.5	422.3	21.4	0.324	1.046	0.044	0.0018	0.0001	129
4.5	424.7	17.9	0.271	1.674	0.051	0.0021	0.0001	246
5.5	425.1	17.7	0.268	1.673	0.048	0.0021	0.0001	250

To avoid errors coming from different plume shapes and sizes, the plume mask of the simulation with an aerosol optical thickness of 0.0001, aerosol height of 3000 m and an aerosol size of 3.5 is applied to all simulations with different values for the aerosol size distribution. Figure 6.23 shows the mass enhancement per pixel inside the plume when the location and size of the plume is known and the same plume mask is applied to all simulations. Nevertheless, the aerosols are still dispersed homogenously over the whole scene with increasing aerosol sizes between the four simulations. The mass enhancement eaches values from 0.8 kg per pixel down to some single pixels, which are not enhancend against the background, with -0.6 kg. The simulation in the upper left corner shows the scenario for the biggest aerosol size. This simulation appears the most heterogenous in colours per pixel as here the enhancment varies the most between the pixels. The mean background value, to which the enhancment inside the plume is compared to, goes from 425.1 ppm for a reff value of 5.5 down to 417.3 ppm (reff=2.5). The mean enhancement against the mean background values is nearly the same for all simulations. With the highest mean enhancement of 17.568 ppm for the aerosol size distribution of 3.5 and the lowest of 17.4 ppm for reff=2.5 the mean enhancement against the background has a difference of 0.144 ppm between the simulations with different aerosol sizes. Figure 6.24 shows the IME for different aerosol sizes when the aerosols are dispersed homogenuously over the whole scene and the same plume mask is applied for all simulations. The IME is nearly the same for all simulations with a value slightly above 1.65×10^5 kg. However, the respective error to the IME increases with increasing aerosol sizes from 0.049×10^5 kg up to 0.080×10^5 kg. Therefore, the uncertainties in the quantification of the CO_2 grow bigger with increasing aerosol sizes. Nevertheless, for the scenario that the aerosols are dispersed homogenously over the whole scene and the same identical plume mask is applied to all the simulations the IME is nearly the same and thus the retrieved CO_2 does not get under- or overestimated for this scenario.

Table 6.9 summarizes the calculated parameters for the increasing aerosol sizes. It provides information about the mean background value, the mean enhancment inside the plume in ppm and kg and the IME and its respective error.

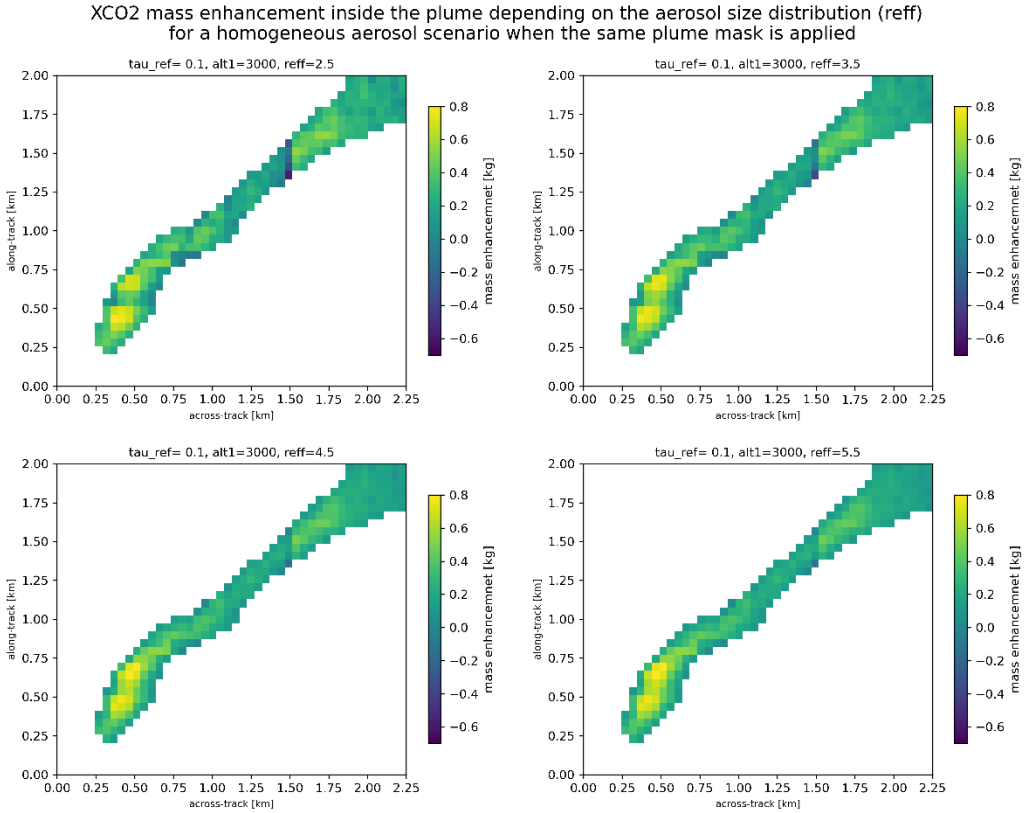

Figure 6.23: The XCO2 mass enhancement inside the plume is shown for simulations with different values for the aerosol size distribution. The automatic plume mask detection of the simulation with tau_ref value 0.001 is applied for every other simulation to ensure that the plume mask is detected and the same. This makes comparison possible. Aerosols are dispersed homogenous over the whole scene.

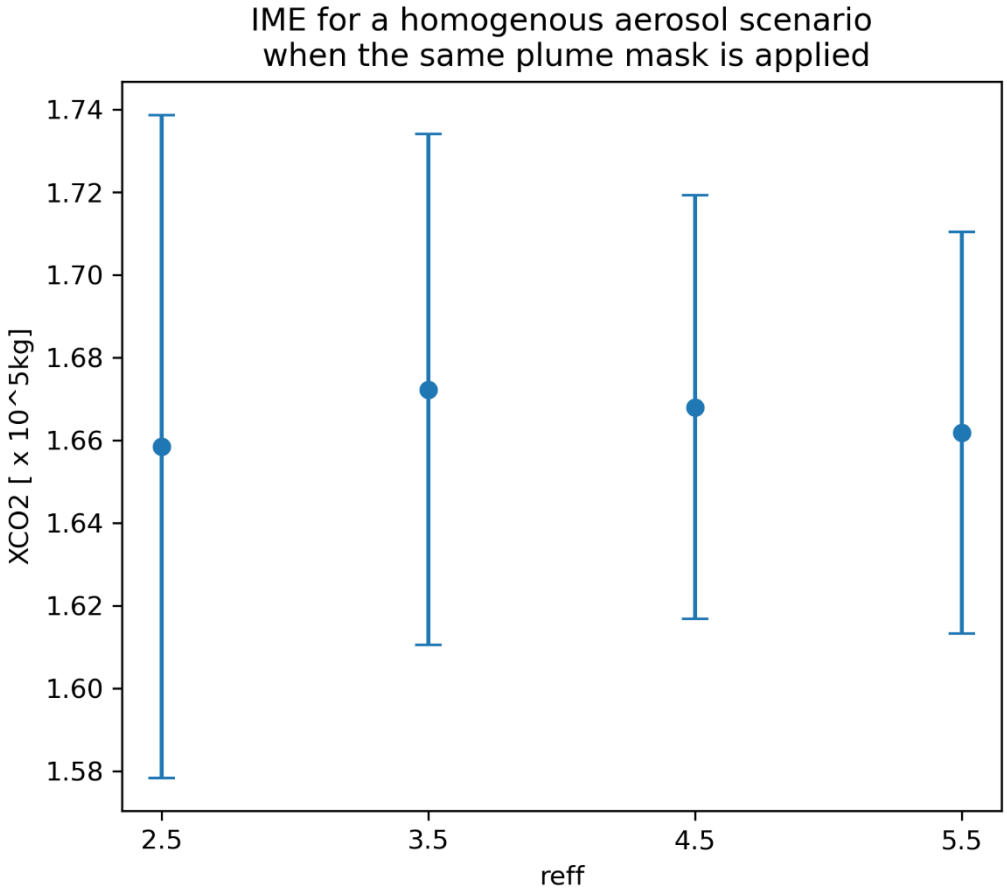

Figure 6.24: IME for the same plume mask depending on aerosol size distribution. The aerosols are dispersed homogenous over the whole scene for the different simulations with increasing values for reff. The IME is calculated for the scenario that for every simulation the plume mask of the simulation with tau_ref=0.0001 is applied. The background value varies as also there the aerosol scattering depending on reff is applied.

Table 6.9: Parameters for the dependence on aerosol size distribution. The aerosols are homogenously dispersed over the whole scene. The IME is calculated for the scenario that for every simulation the plume mask of the simulation with tau_ref=0.0001 is applied. The background value varies as also there the aerosol scattering depending on the varying reff value is applied.

reff	**mean background CO_2 [ppm]**	**mean enhancement[ppm]**	**mean mass enhancement [kg]**	**IME [x10^5 kg]**	**Error IME [x10^5 kg]**
2.5	417.3	17.4	0.263	1.659	0.080
3.5	422.3	17.6	0.265	1.672	0.062
4.5	424.8	17.5	0.265	1.668	0.051
5.5	425.1	17.5	0.264	1.662	0.049

6.3.6 Study 6: Influence of increasing aerosol size inside plume, outside plume very less aerosols

This study presents the influence of the aerosol size distribution for the scenario that the aerosol size is just changed inside the plume whereas the background stays with a constantly low aerosol amount. For all simulations the same plume mask is applied, thus the plume mask does not differ in size and shape.

Figure 6.25 displays the mass enhancement inside the plume against a constant background. The mean background value comes from the simulation with an aerosol optical thickness of 0.0001 in an aerosol height of 3000 m and an aerosol size distribution of 3.5. For this simulation the mean background value is 427.9 ppm. Compared to this value the enhancement inside the plume for different aerosol sizes is calculated. The enhancement is differing significantly for each simulation. The simulation has the greatest enhancement with small aerosols (reff=5.5) with 14.7 ppm and the smallest enhancement against the constant background is found with 6.918 ppm for an aerosol size distribution of 2.5. Also, Figure 6.25 shows that the mass enhancement for each pixel reaches values between 0.8 kg and -0.6 kg. The lower two plots show the mass enhancement for small aerosols inside the plume. In these two simulations the enhancement is mainly in the positive range, having light blue and yellow colours. The upper two plots show the mass enhancement for big aerosols inside the plume. The pixels in these plots are more heterogenous in colours and are reaching more negative values, what implies that there is no enhancement against the mean background value for this pixel. Figure 6.26 presents the IMEs and their respective errors for the four simulations with increasing aerosol sizes inside the plume. With increasing aerosol sizes the IME decreases from $1.402 \pm 0.043 \times 10^5$ kg for small aerosols (reff=5.5) down to $0.658 \pm 0.043 \times 10^5$ kg for an aerosol size distribution of 2.5. The error does not change with increasing aerosol sizes. The IME and its error signify that the retrieved CO_2 gets significantly underestimated for big aerosols inside the plume when the background has a very low aerosol abundance in the atmosphere.

Table 6.10 summarizes the above mentioned parameters of the mean background value, the enhancement inside the plume in ppm and kg and the IME and the respective error for the four simulation with different aerosol size distributions inside the plume.

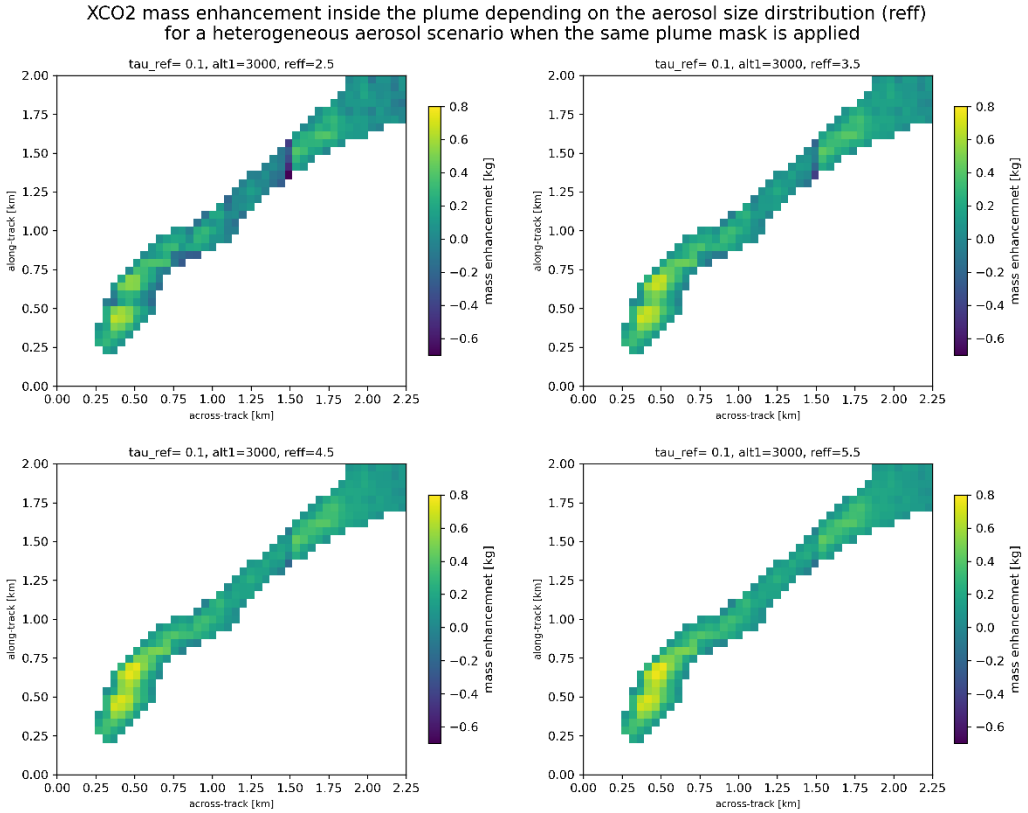

Figure 6.25: The XCO2 mass enhancement inside the plume is shown for simulations with different values for the aerosol size distribution. The automatic plume mask detection of the simulation with tau_ref value 0.001 is applied for every other simulation to ensure that the plume mask is detected and the same. This makes comparison possible. The aerosol amount of the background against which the enhancement is calculated is also taken from this simulation with very few aerosols and a reff value of 3.5 like the plume mask and thus stays the same for all simulations with 427.9 ppm.

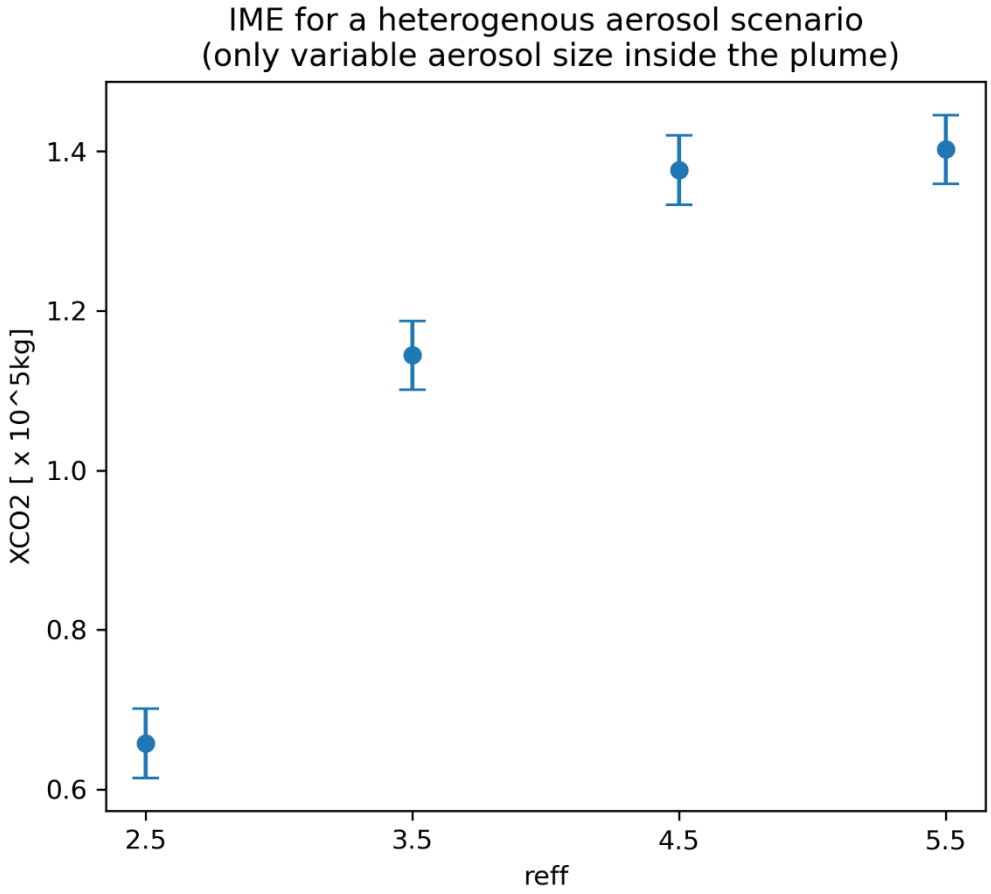

Figure 6.26: IME for the same plume mask depending on aerosol size distribution. In this scenario the aerosols are heterogeneously dispersed over the scene. Thus, the aerosol size only changes inside the plume. The IME is calculated for the scenario that for every simulation the plume mask of the simulation with tau_ref=0.0001 is applied. Also, the background is the same for all with mean background value of the simulation with tau_ref=0.0001 with 427.853 ppm.

Table 6.10: Parameters for the dependence of the aerosol size distribution for the heterogenous aerosol scenario. Furthermore, the same plume mask is applied to all the simulations. Therefore, the mean background values are always the same of the tau_ref =0.0001 simulation (427.9 ppm).

reff	**mean back-ground CO_2 [ppm]**	**mean enh ancement [ppm]**	**Mean mass enhance-ment [kg]**	**IME [x10^5 kg]**	**Error IME [x10^5 kg]**
2.5	427.9	6.9	0.104	0.658	0.043
3.5	427.9	12.0	0.182	1.144	0.043
4.5	427.9	14.5	0.218	1.376	0.043
5.5	427.9	14.7	0.223	1.402	0.043

6.4 Results of the influence of albedo

In the previous studies a strong correlation between the XCO_2 error coming from aerosol scattering and the surface albedo was discovered. Therefore, the influence of the surface albedo at a height of 2000 nm is investigated in detail in this chapter. As the biggest influence of aerosol scattering was found for a simulation with high aerosol amount, the simulation with tau_ref= 0.5, alt1=3000m and reff=3.5 is used to investigate the influence of different surface albedo. For all the presented simulations above the albedo scene was the same albedo scenario as the one at 2000 nm like shown in Figure 6.1. To investigate the influence of the surface albedo, different albedo scenarios were simulated and put as an input file into the RemoTeC algorithm. Four scenarios were generated with the albedo being homogenous over the whole scene with the values of 0.1, 0.3, 0.5 and 0.6. These four scenarios have been applied to an aerosol scattering run with an aerosol amount of 0.5. Accordingly, the influence of a very dark scene with an albedo of 0.1 and a bright scene with an albedo of 0.6 is considered for a run with many aerosols present in the atmosphere.

Figure 6.27 shows the retrieved CO_2 values with different homogenous albedo scenarios. The XCO_2 for the scenario with albedo values of 0.6 and 0.5 over the whole scene, standing for homogenous bright surfaces, have values between 430 ppm and 490 ppm, while the scenario with an albedo of 0.3 only reaches values between 420 ppm and 480 ppm. The scene with an albedo value of 0.1, thus being a homogenous dark surface, reaches values between 390 ppm and 420 ppm. Therefore, this scene appears a lot darker. Nevertheless, in all scenarios a visible plume with much higher XCO_2 values is recognizable. Compared to the simulation with a heterogenous albedo scene and an aerosol amount of 0.5, where no coherent plume was visible, in this case a coherent plume is detected for all scenarios with a homogenous surface albedo. The bottom plot on the left side in Figure 6.4**.** shows the retrieved CO_2 for the same aerosol scattering scenario with an heterogenous albedo scenario. Because of the fact that a coherent plume is found when the same aerosol scattering is applied for the scenarios with a homogenous albedo scene with different values, it can already be assumed that the surface albedo in combination with aerosol scattering has a big influence on the retrieved CO_2 and thus on the quantification of CO_2 of point sources.

To validate this impression, the IME for each scenario was calculated. Figure 6.28 shows the IME for the different simulations with varying aerosol amounts as reference to the simulations with an aerosol amount of 0.5 and varying homogenous albedo scenarios. Compared to the IME of 0.4737 ± 0.0574 x 10^5 kg for the scenario with high aerosol amount and a heterogenous albedo scene, the IME for the homogenous scenes lies with 0.8854 ± 0.0232 x 10^5 kg for the albedo value of 0.1 increasing to 1.6634 ± 0.0419 x 10^5 kg for an albedo of 0.6, significantly higher. This means, that the IME gets less underestimated for homogenous albedo scenarios. However, the homogenous albedo scenarios assign more pixels to the plume than the heterogenous scene with the same aerosol amount. Hence, the plume for the homogenous scenarios is bigger and therefore also the IME is expected to be higher. To be able to compare the heterogenous scenario to the homogenous scenario, the IME per plume length is calculated. Figure 6.29 presents the IME per plume length. The most striking difference between the IME and the IME per plume length is that the IME for the albedo scenario of 0.1 was higher than the heterogenous scene and the IME per plume length is with 0.00110 ± 0.00003 x 10^5 kg significantly lower than the value of the heterogenous scene with an IME per plume length of 0.00144 ± 00018 x 10^5 kg. Therefore, the IME gets even more underestimated for a homogenous dark surface with an albedo of 0.1 than for a heterogenous scene when also applying aerosol scattering. For a brighter surface albedo of 0.3 and higher the homogenous scene brings much improvement with an IME per plume length of 0.00182 ± 0.00005 x 10^5 kg or higher. These scenarios reach values close to the IME per plume length of 0.00209 ± 0.00005 x 10^5 kg with very few aerosols present in the atmosphere. Consequently, not just the difference between a heterogenous and a homogenous surface albedo influences the quantification of CO_2, but also the exact albedo value. More precisely, a homogenous bright surface albedo improves the correct estimation for the retrieved CO_2, even if many aerosols in the atmosphere modify the light path. The underestimation of CO_2 due to aerosol scattering gets smaller when the surface over which the plume is measured is bright. Contrarily, the retrieved CO_2 gets even more underestimated for a homogenous dark surface than for a heterogenous surface.

Table 6.11 presents the overview for the mentioned parameters of the different simulations with an aerosol amount of 0.5 and a heterogenous albedo input. Furthermore, the parameters for the scenario of an aerosol amount of 0.5 and different homogeneous

surface albedo are listed. The parameters are the mean background value in ppm to which the enhancement is calculated to, the enhancement in ppm and kg, as well as the IME and its error. Furthermore, the IME per plume length and its respective error and the number of pixels considered to be part of the plume are given.

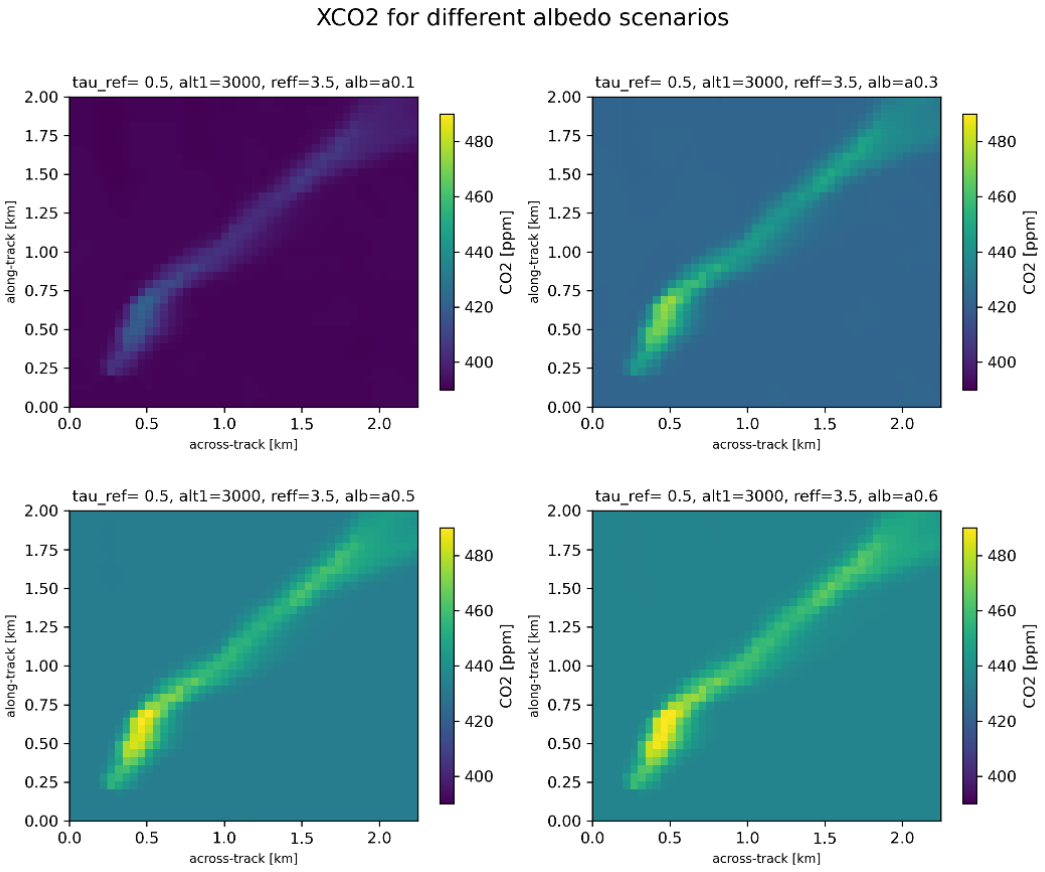

Figure 6.27: XCO2 values for the scene with different homogenous surface albedo scenarios. For all simulation aerosol scattering with an aerosol amount of 0.5 is applied.

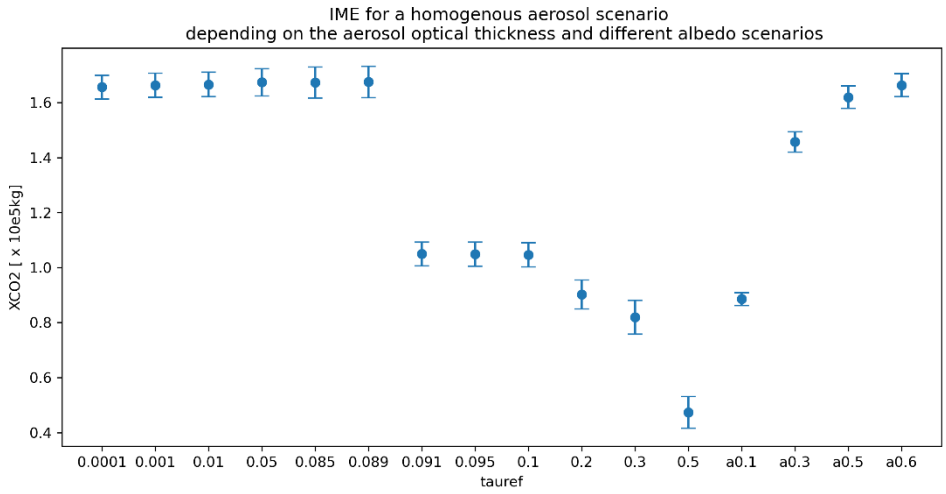

Figure 6.28: IME for the simulations with different values for the surface albedo for the simulation with an aerosol optical thickness of 0.5. The IME for the different values for the aerosol optical thickness is displayed again as a reference. For all simulation the automatic plume detection finds the plume and thus the plume mask can differ in size and shape for each simulation.

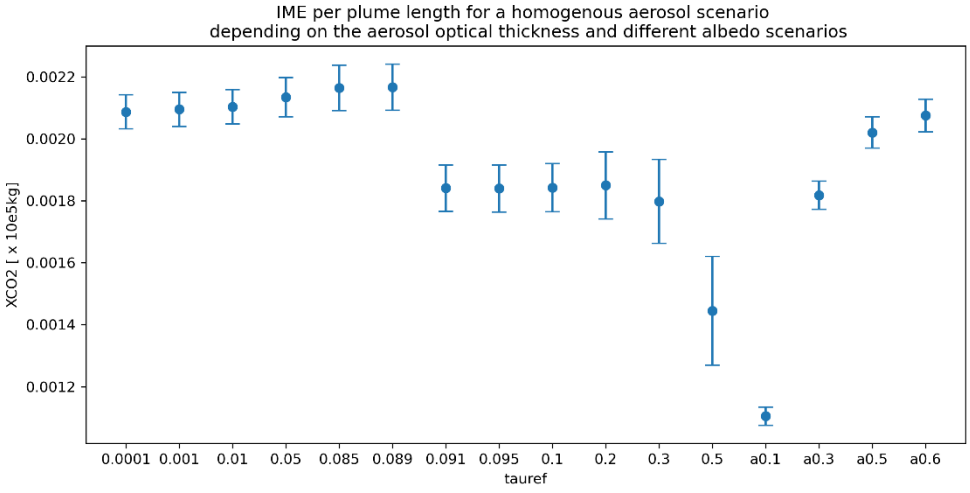

Figure 6.29: IME per plume length for the simulations with different values for the surface albedo for the simulation with an aerosol optical thickness of 0.5. The IME per plume length for the different values for the aerosol optical thickness is displayed again as a reference. For all simulation the automatic plume detection finds the plume and thus the plume mask can differ in size and shape for each simulation.

Table 6.11: Calculated parameters of the simulation with homogenous surface albedo for the whole scene. The simulations with varying albedo values are made for the aerosol optical thickness (tau_ref) of 0.5.

tauref	**Mean CO_2 background [ppm]**	**CO_2 enhancement [ppm]**	**mean mass enhancement [kg]**	**IME [x10^5 kg]**	**Error IME [x10^5 kg]**	**IME per plume length [x10^5 kg]**	**Error IME per plume length [x10^5 kg]**	**pixel number**
0.5	403.594	29.154	0.441	0.474	0.057	0.00144	0.00018	43
a0.1	392.909	9.121	0.138	0.885	0.023	0.00110	0.00003	257
a0.3	425.809	15.012	0.227	1.457	0.037	0.00182	0.00005	257
a0.5	435.523	16.684	0.252	1.620	0.041	0.00202	0.00005	257
a0.6	438.590	17.134	0.259	1.663	0.042	0.00208	0.00005	257

7 Discussion

This chapter includes a short discussion of the methods used and general problems that can influence the quantification of the CO_2 in the satellite mission CO2Image and were not considered in this thesis before. Then the results of the presented aerosol studies are discussed, followed by another discussion about the influence of the surface albedo considering aerosol scattering in the quantification of CO_2.

First, it should be noted that there are different aspects which make GHG observation from space challenging, especially in a high spatial resolution. This thesis does not discuss the different challenges of the satellite mission CO2Image that are related to the instrument design in order to achieve the accuracy and precision making it possible to quantify GHG from space or to the constantly moving satellite which is causing smearing. Furthermore, other components, which can modify the measured light path, like water clouds and cirrus are not considered. Clouds, consisting of water or ice, can cause problems and can even be responsible for the measured scene being not usable for further analysis. However, the prevailing work concentrates on the influence of aerosols on the quantification of CO_2.

Second, this work relies completely on the correct calculation of the retrieval algorithm RemoTeC. Yet, RemoTec is one of the few algorithms which considers aerosol scattering reliable (Butz et al., 2009; Butz et al., 2010; Butz et al., 2011). Therefore, at 750 nm RemoTeC is suited to perform simulations with aerosol scattering for aerosol optical thickness up to 0.25 (Guerlet et al., 2013). The studies in this thesis were performed at 765 nm and mostly with an aerosol optical thickness of less than 0.3, except one simulation having a higher aerosol optical thickness. However, in the performed simulations RemoTeC was only considering aerosol scattering in the forward run, but not in the retrieval. Another challenge is that information about the aerosol parameters (e.g. aerosol amount, type, size and height distribution), which is needed to calculate the scattering, is mainly not available. Therefore, the retrieval methods must deal with simultaneously inferring gas concentrations and correcting effects of aerosol scattering (Bril et al., 2009; Butz et al., 2009; Butz et al., 2010; Butz et al., 2012; Connor et al., 2008; Frankenberg, Meirink, et al., 2005).

A further uncertainty in this work is the background concentration to which the enhancement inside the plume is in respect to. Nassar et al. (2017) even state that the background is of concern for all studies with an defined enhancement compared to the background. In this study the background is a fixed area, that is chosen with knowledge of the location of the plume. Other methods would be to plot all retrieved CO_2 values for every pixel and fit a Gaussian distribution or to automatically select a region if the location of the point source is known as well as the wind direction and wind speed.

Moreover, depending on the value for the aerosol optical thickness the background concentration of CO_2 varies significantly with values between 403 ppm and 428 ppm. NOAA's Global Monitoring Lab reports a value of 414.72 ppm for the global average atmospheric carbon dioxide in 2021 (NOAA, 2022b). This thesis assumes knowledge about the airmass which is necessary for the algorithm RemoTeC to calculate the retrieved CO_2 as stated in the study of Strandgren et al. (2020). In fact, data about the meteorology and topography would be obligatory to calculate the air mass. Here also meteorological data like the wind speed or direction are not considered for the plume simulations. Nonetheless, the estimation of emission and its respective error is linearly dependent on wind speed (Bovensmann et al., 2010). However, even if these parameters are not available, it was possible to make a first meaningful estimate of the influence of aerosol scattering on the quantification of CO_2 in the CO2Image mission.

7.1 Influence of aerosol scattering on the quantification of XCO_2

This chapter presents a discussion about the influence of aerosol scattering on the quantification of CO2. It is structured into a first discussion about the uncertainties regarding aerosols in general, followed by a discussion about the results of the different scenarios listed in Table 6.1. The first scenario reflects the aerosols being homogenously dispersed over the whole scene. This scenario is split into two different cases. In the first case an automatic plume detection is applied to the simulations and thus the plume mask varies in size and shape. The other case of the homogenous dispersed aerosols applies the same plume mask of a simulation with very few aerosols to every other single simulation. This makes the results comparable and avoids errors resulting from different plume masks. Further on, the scenario which considers the circumstance that the aerosol parameters are

only changed inside the plume, whereas the background remains constant with a very low aerosol abundance in the atmosphere, is discussed. For every scenario all of the three aerosol parameters investigated in this work are discussed.

The aerosol studies are performed for one aerosol type with single scattering albedo and an index of refraction as it is given for liquid water. The optical parameters were calculated by RemoTeC through the defined physical parameters as the aerosol amount, aerosol size distribution and aerosol height distribution, as explained in chapter 5.2. Also, Huang et al. (2020) studied the influence of single scattering aerosols and states that these aerosols cause an underestimation when retrieving CH_4 and induce large biases in the retrieval.

Although aerosols can cause errors in the retrieval of CO_2, studies show that these errors can be reduced when the retrieval algorithm considers the scattering of aerosols. Observations found that, if aerosol scattering is taken into account in the retrieval algorithm, most of the XCO_2 difference to the true CO_2 is under 2.5 ppm (Strandgren et al., 2020). However, atmospheric aerosol, clouds and cirrus modify the light path of the measured solar radiation depending on the particle amount, the particle optical properties and their height, as well as the surface albedo (Strandgren et al., 2020). Therefore, this thesis investigated the influence of the aerosol amount, the aerosol height distribution and aerosol size distribution on the quantification of CO_2 of point sources in the satellite mission CO2Image of the DLR.

Homogeneous aerosol scenario with automatic plume detection

Regarding the scenario that aerosols are homogenously dispersed over the whole scene and an automatic plume detection is applied it can be seen that the automatic plume detection is not able to detect a coherent plume for aerosol optical thicknesses bigger than 0.089 (study 1). As a smaller number of pixels is accounted to the plume the IME inside the plume gets underestimated significantly. This is observed for the investigation of the influence on the quantification of CO_2 of the aerosol height distribution (study 3). If the aerosol height is exceeding 3000 m the automatic plume detection fails at finding the whole plume. Also, study 5 shows that for an aerosol size bigger than reff= 3.5 the IME is underestimated due to the loss in pixels accounting to the plume. Therefore, the figures

for all three aerosol parameters, presenting the IME, show different levels of the IME values. Thereby, the steps between the levels occur in the case that the automatic plume detection is not able to find the whole plume anymore.

To sum up, errors which occur due to different plume sizes were found when quantifying the CO_2. Furthermore, the approach of calculating the IME per plume length failed to compensate this source of error. Other studies had to deal with this problem as well and suggest different solutions (Bovensmann et al., 2010; Nassar et al., 2017; Strandgren et al., 2020). The wind direction and wind speed have a big impact on the plume and the transportation of the emitted CO_2 of the point source, as well as on the plume height. Due to turbulence and dilution of CO_2 caused by wind the CO_2 will be underestimated (Nassar et al., 2017). Likewise, Bovensmann et al. (2010) found that the estimation of GHG emissions is linearly dependent on the wind speed. Accordingly, one improvement in the automatic plume detection could be made by taking the wind speed and wind direction into account. Additionally, the kernel used for averaging over the neighbourhood of a spatial pixel could be changed into an oval averaging kernel, with its long axis oriented in the direction of the wind to reduce errors at the plume border (Strandgren et al., 2020). Another improvement would be to allow the automatic plume detection algorithm to identify two regions as plume, even if they are not directly connected. However, this can cause errors in finding enhancements which are not related to emissions of a point source. Furthermore, the size of the plume mask depends on the chosen p-value. Thus, developing an automatic plume mask algorithm can improve the results and avoid errors due to the smaller plume mask, which leads to an underestimation of the true CO_2.

To make the analysis of the enhancement inside the plume comparable and to avoid errors due to different plume sizes and shapes, the same plume mask from the simulation with very few aerosols was applied to all simulations. To apply the same plume mask on every simulation means to pretend that the location, shape, and size of the emission plume is known. Hence, knowledge about these parameters of the plume is necessary. Achieving this knowledge could be possible through different proxies. For instance, the CO2Image mission aims to additionally measure CH_4, which could be used in this case to clarify the plumes' location, shape and size.

Homogeneous aerosol scenario where the same plume mask is applied

In the case that the aerosols are homogenously dispersed over the whole scene and the same plume mask is applied to all simulations, study 1 finds that IME does not differ significantly for the simulations with an aerosol optical thickness between 0.0001 and 0.2. In this range the IME stays approximately the same with values slightly above 1.657 x 10^5 kg. For aerosol optical thicknesses bigger than 0.2 the IME decreases, indicating an underestimation of the retrieved CO_2 concentrations. Furthermore, the errors and thus the uncertainties increase with high aerosol amounts. Therefore, challenges are expected in areas with a high aerosol abundance in the atmosphere. This could lead to problems in quantifying point sources in highly polluted areas like metropolises in China. Further, challenges in the quantification of CO_2 concentrations could be dependent on the season. In the winter more aerosols are expected in the atmosphere and therefore more scattering due to aerosols is expected, which leads to an underestimation of the CO_2 emissions of point sources. Nevertheless, for the case that the aerosols are homogenously dispersed over the whole scene and the same plume mask is applied the IME differs just in a range of 0.11 x 10^5 kg. Therefore, measuring the SNR, when having homogenously dispersed aerosols over the whole scene, does not underestimate the quantification of the retrieved CO_2 significantly. Only in scenes with a high aerosol abundance in the atmosphere the XCO_2 is slightly underestimated. Accordingly, for most scenes with homogenously dispersed aerosols, scattering due to aerosols can be neglected. This gained knowledge verifies hypothesis two.

Study 3 finds that with increasing aerosol heights the IME is bigger and hence the retrieved CO_2 is slightly overestimated in heights above 5000 m. For this case it should be noted that, although aerosols can be in such high areas, the plume will not reach heights over 2000 m as the CO2Image mission is measuring during the day and the plume will always be in the planetary boundary layer at those times, which reaches heights of maximum 1500 m in Europe and 2000 m in the tropics (Seidel et al., 2010).

Study 5 finds that there are almost no differences in the IME for different aerosol sizes. Only the errors and thus the uncertainties, when estimating the enhancement inside the plume, grow bigger with increasing aerosol sizes. Consequently, the aerosol size does not play an important role when the aerosols are dispersed homogenously over the whole scene.

In summary, the case of homogenously dispersed aerosols, the influence of aerosol scattering in the CO2Image mission can be mostly neglected, as the SRN is measured. This is true for the case that the same plume mask is applied. Furthermore, it is only possible to neglect scattering due to aerosols as the retrieval algorithm RemoTeC is considering aerosol scattering. Also, other studies found that errors can be reduced when the retrieval algorithm is considering aerosol scattering which leads to the fact that the retrieved CO_2 does differ a lot from the true CO_2 (Strandgren et al., 2020). Therefore, the second hypothesis can be verified for homogenous scenarios as the CO_2 concentrations do not get significantly underestimated and scattering due to aerosols can be neglected for most scenes.

Heterogenous aerosol scenario

The other scenario investigated in this work assumes the case that the aerosols vary in their amount, height, and size distribution only inside the plume, whereas the background concentration, to which the enhancement is in respect to, stays constantly at 427.9 ppm for a scenario with a low aerosol optical thickness. To apply this scenario on the simulations, knowledge about the plumes location and size is necessary. Therefore, the same plume mask is applied for every simulation. This is considered to be the most realistic scenario, as it is assumed that point sources not only emit CO_2 but also other small particles like soot.

Study 2 finds that the IME is significantly underestimated with increasing aerosol optical thicknesses. It should be noted that also some pixels, which are not enhanced compared to the background are considered inside the plume, as the plume mask is not applied individually. This refers also to the results of study 4 and study 6. Likewise, Butz et al. (2009) state that the abundance of aerosols in the atmosphere shorten the measured light path and therefore the true CO_2 is significantly underestimated.

Study 4 shows that the IME is strongly underestimated for increasing aerosol heights. However, the plume and therefore the enhanced aerosols inside the plume are not expected to be higher than 2000 m. It is realistic that the measured plume will be lower than 2000 m, because the CO2Image mission will just be able to measure during the day. During the day the planetary boundary layer in Europa mostly reaches values below 1500 m, while it can reach up to 2000 m in the tropics due to heat exchange and turbulence

(Seidel et al., 2010). Only during the night the planetary boundary layer is thinner. Therefore, the plume will never reach the open troposphere at a measured moment. Furthermore, in study 4 the aerosols inside the plume are simulated for greater heights, while the CO_2 values get not changed in their height. Thus, there is no realistic simulation of a plume in heights bigger than 2000 m. Based on this, study 4 does not present physically relevant data, if assuming aerosols only inside the plume for the case that the plume height is over 2000 m.

Study 6 finds that with increasing aerosol size the IME is underestimated for bigger aerosols inside the plume than in the background. Therefore, hypothesis one can be partly verified. For a scene with heterogeneously dispersed aerosols the CO_2 concentrations of a point source are significantly underestimated due to aerosol scattering depending on the increase of the aerosol amounts, aerosol height distributions and aerosol size distributions. However, according to other studies, that are investigating the effect of aerosol scattering in the measured backscattered solar radiation, the light path shortening effect for cirrus is bigger than for aerosols and the effect differs notably between the stations (Guerlet et al., 2013). Further, Jacob et al. (2022) state that in the SWIR spectrum atmospheric scattering can be neglected, except for clouds and large aerosols. However, these studies were performed for a coarser spatial than in this work.

Moreover, studies testing the retrieval of simulated observations with aerosol and cirrus abundance support the results found in this work: using an algorithm that considers aerosol scattering, scattering errors can be reduced to less than 1% (Butz et al., 2012). This study was performed for CH_4. Only for high particle abundance or very small surface albedos difficulties in retrieving the CH_4 occurred. Granting all this, errors due to aerosols and clouds can be avoided with a retrieval algorithm that takes scattering into account, except for scenes with high aerosol abundance or thick clouds. These scenes would need to be filtered out before the further data processing (Strandgren et al., 2020). Furthermore, it should be noted that CO2Image will not be able to measure the emissions of a point source continuously. Therefore, the picture of the plume and the respective CO_2 emissions are only a snapshot, and it remains unknown if the point source is continuously emitting the measured amount of CO_2 or if it was emitting a high or low concentration of CO_2 only in this very moment depending on the performance of the industry in one single moment. However, it should be noted that that CO2Image is a demonstrator mission.

To sum up, this study found that for a spatial resolution of 50 x 50 m^2 scattering due to aerosols can be neglected if the aerosols are homogenously dispersed over the whole scene, the location and size of the plume is known and the retrieval algorithm takes aerosol scattering into account. However, if the aerosol amount, height or size only changes inside the plume and the background still has a low aerosol amount, errors occur and the IME is significantly underestimated. Therefore, in agreement with the study of Guerlet et al. (2013) a correlation between the retrieved CO_2 error and the aerosol parameters was found. The next chapter investigates if there is also an agreement with Guerlet et al. (2013) study that there is no significant correlation of errors with the surface albedo.

7.2 Influence of the surface albedo on the quantification of XCO_2

Studies about the influence of the surface albedo show that, if aerosol scattering is considered in the retrieval algorithm, the structures of the surface albedo are significantly more visible. This is caused by the effect of darker surfaces limiting the multiple scattering effect of aerosols as light "is swallowed" and lost for the measuring sensor due to the dark surface with less reflection. Hence, aerosols scatter the incoming solar radiation higher up back to the sensor and shorten the measured light path. The consequence is an underestimation of the retrieved CO_2. On the other hand, for bright surfaces the dominant effect is the multiple scattering between the aerosols. Multiple scattering causes an extension of the measured light path and the XCO_2 is overestimated (Strandgren et al., 2020). Therefore, aerosol scattering and the surface albedo are mutually reinforcing each other.

This work found that with decreasing albedo values the IME is significantly underestimated if aerosol scattering is applied. Nevertheless, for simulations with high aerosol optical thicknesses and bright homogenous surfaces the IME is not underestimated as much as in simulations with high aerosol abundances and heterogeneous albedo scene. Accordingly, the albedo can be a mediator for the effect of the light path shortening due to aerosols. This is also confirmed in the study of Butz et al. (2009), which points out that the albedo is controlling the fraction of incoming light which is then available for scattering effects due to aerosols. Whereas bright surfaces can be a mediator of aerosol scattering

effects, dark surfaces reinforce the scattering effect of aerosols, causing the retrieved CO_2 to be even more underestimated. Furthermore, studies about retrieving CH_4 show that very low and high albedo scenes present the biggest challenge for the retrieval algorithm (Lorente et al., 2021). Also, Strandgren et al. (2020) summarise that the surface albedo induces if the effect of the reduced or extended light path is dominating. Hence, in agreement with other studies hypothesis three can be verified. Dark surfaces amplify the effect of underestimation of the CO_2 concentrations due to aerosol scattering, whereas bright surfaces can mitigate this effect and thus the albedo can be a mediator.

Summarising the above, it should be noted that the aerosol amount, height and size, as well as the surface albedo influence the light path. The interaction between these parameters can lead to under- or overestimating of the true CO_2. While light path shortening occurs stronger for dark surfaces, bright surfaces cause light path enhancements due to multiple scattering between the aerosols and the surface (Butz et al., 2009; Butz et al., 2012). Dark surfaces therefore reinforce the underestimation of CO_2, whereas bright surfaces can be a mediator for aerosol effects which would lead to underestimating the CO2.

Therefore, a significant correlation between the errors when retrieving CO_2 and the surface albedo is found, as well as the above stated correlation between the errors and the aerosol parameters.

8 Summary and Conclusion

To mitigate climate change successfully, independent verification of GHG emissions is important. DLRs' new satellite mission CO2Image with a spatial resolution of 50 x50 m^2 will help to monitor medium to large point sources.

The instrument of the CO2Image mission will measure the backscattered solar radiation to quantify the CO_2 emissions. Different environmental parameters such as scattering due to aerosols or the surface albedo modify the measured light path.

This work successfully performed simulations with different values for the three aerosol parameters: aerosol optical thickness, aerosol height distribution and aerosol size distribution. Furthermore, a short investigation of the influence of the surface albedo was presented. The results of the aerosol studies in this thesis performed with the RemoTeC algorithm show that, if aerosol scattering is considered homogenous over the whole scene, no significant difference between the IME of the individual simulations depending on aerosol parameters was found. Therefore, scattering through aerosols can be neglected, if the operating algorithm considers aerosol scattering and the aerosols are dispersed homogenously over the whole scene.

For heterogeneously dispersed aerosol scenes with increasing values for the aerosol optical thickness, height and size distributions inside the plume while the background stays constant a significantly underestimation of the retrieved CO_2 was found. Due to the performed studies the first hypothesis of this work can be partly verified. In a scenario with increasing values for the aerosol amounts, the aerosol height distributions and the aerosol size distributions inside the plume the retrieved CO_2 concentrations are significantly underestimated. However, this does only apply if the aerosols are heterogeneously dispersed.

The second hypothesis that aerosols can be neglected in the CO2Image mission of the DLR is true for the scenario of homogenously dispersed aerosols. In this scenario no significant difference in the IME with increasing values for the aerosol parameters was found. Due to the measured SNR of the instrument and a homogeneously dispersed aerosol scenario aerosol scattering can be neglected, whereas in a heterogenous scenario scattering due to aerosols cannot be neglected.

This work was able to verify the third hypothesis that dark surfaces will amplify the effect of aerosol scattering while bright surfaces can be a mediator and diminish the underestimation of retrieved CO_2 concentrations through aerosol scattering.

To sum up, this study found that in the CO2Image of the DLR mission with a spatial resolution of 50 x 50 m^2 to quantify CO_2 emissions of point sources scattering due to aerosols can be neglected, if the aerosols are homogenously dispersed over the whole scene. This requires knowledge about the location, size and shape of the plume. However, with increasing values for the aerosol optical thickness, aerosol height or size distributions inside the plume and a constant background with a low aerosol amount outside the plume errors occur. In this case the IME gets significantly underestimated with increasing values of the aerosol optical thickness, the aerosol height or the aerosol size distributions. Furthermore, this work found a strong correlation of the surface albedo to the errors in the retrieved CO_2. While dark surfaces reinforce the underestimation of the true CO_2 due to aerosol scattering, bright surfaces can be a mediator for errors caused by aerosol scattering.

9 Outlook

The performed aerosol studies give an important impression of the influence of aerosol scattering on the quantification of CO_2 of point sources for the CO2Image mission with a spatial resolution of 50 x50 m^2. However, some improvements of these studies should be made to create a more detailed impression of the errors in the quantification of CO2 caused by aerosol scattering.

Firstly, the automatic plume detection needs further adaptions to avoid errors related to different plume sizes and shapes. Therefore, it should be assured that the plume always starts at the source and the algorithm is able to find the plume starting at the point source. Another possible improvement of the automatic plume detection could be to allow two regions to be part of the plume, even if they are not directly connected. Furthermore, a proxy to gain knowledge about the plume location and size could be helpful. As CO2Image also aims to measure CH_4, this could be one possible proxy as reference.

Secondly, difficult scenes with high abundances of aerosols or thick layers of clouds should be identified and filtered out (Strandgren et al., 2020). For this, the two CO_2 absorption bands could be evaluated separately. Therefore, the effect of scattering due to aerosols could be investigated in the strong and weak CO_2 band separately. If there is no difference between the two bands, it would indicate a low aerosol abundance. Differences between the two bands would show the impact of the aerosol abundance. Consequently, this difference could be used to filter out scenes with high aerosol abundances and a most likely an underestimation of the CO_2.

Moreover, so far only the forward run simulating the spectra considers aerosol scattering. Further studies, that also take the aerosol abundance in the retrieval into account, are recommended. As every pixel is needed to be calculated separately and there are many spectra needed to be calculated, the analysis time would be very high.

This study found that the surface albedo can be a mediator for bright surfaces. Dark surfaces amplify the effect of underestimating the CO_2 concentrations due to aerosol scattering. To deal with the challenge of heterogenous surfaces, one attempt could be to classify the scenes accordingly to their albedo heterogeneity. This could be one possibility to correct the effect of the albedo.

In general, it should be noted that the viewing angel of the satellites instrument over scene is not considered. Due to the movement of the satellite, the viewing angle is changing during the measurement of the individual point source. Hence, this should be considered in further studies. Furthermore, similar studies for CH_4 could be performed, but the requirements for the CO2Image mission concentrate on the monitoring of CO_2. Another capability of the CO2Image mission could be to not only observe anthropogenic sources but also natural sources, like volcanic emissions.

Above all, if the dealing with errors due to environmental parameters like scattering through aerosols is improved, the CO2Image mission of the DLR has a high potential of detecting and estimating 90% of the CO_2 point source emissions as a great contribution to mitigate the anthropogenic climate change.

Acknowledgements

This work would not have been possible without the great support and help from the people around me.

Firstly, I want to thank Dr. Dietrich Feist for supervising this thesis and for always being available for me, even in a personal difficult time. I also thank Prof. Dr. Schmullius for supervising and reviewing my thesis.

Another thanks goes to Prof. Dr. André Butz and Leon Scheidweiler for providing and helping to set up RemoTeC and especially André for providing his expertise in aerosol studies.

Furthermore, I want to thank Dr. Anke Roiger and her department for making this thesis at the DLR possible. Especially to Dr. Julia Marshall and Dr. Friedemann Reum for always being available for questions.

Thank you, Famke for your moral support and encouragement in every emotional stage of my life and the common suffering through the master thesis.

Thank you, Helene and Franka for reviewing my thesis and giving valuable feedback.

Finally, I want to thank my parents for always being there and giving exceptional support. Without you my whole studies would not have been possible.

Bibliography

Ayasse, A. K., Thorpe, A. K., Roberts, D. A., Funk, C. C., Dennison, P. E., Frankenberg, C., Steffke, A., & Aubrey, A. D. (2018). Evaluating the effects of surface properties on methane retrievals using a synthetic airborne visible/infrared imaging spectrometer next generation (AVIRIS-NG) image. *Remote Sensing of Environment*, *215*, 386–397. https://doi.org/10.1016/j.rse.2018.06.018

Bertaux, J.-L., Hauchecorne, A., Lefèvre, F., Bréon, F.-M., Blanot, L., Jouglet, D., Lafrique, P., & Akaev, P. (2020). The use of the 1.27 µm O_2 absorption band for greenhouse gas monitoring from space and application to MicroCarb. *Atmospheric Measurement Techniques*, *13*(6), 3329–3374. https://doi.org/10.5194/amt-13-3329-2020

Boden, T., Andres, R., & Marland, G. (2017). *Global, Regional, and National Fossil-Fuel CO2 Emissions (1751 - 2014) (V. 2017).* https://doi.org/10.3334/CDIAC/00001_V2017

Bovensmann, H., Buchwitz, M., Burrows, J. P., Reuter, M., Krings, T., Gerilowski, K., Schneising, O., Heymann, J., Tretner, A., & Erzinger, J. (2010). A remote sensing technique for global monitoring of power plant CO_2 emissions from space and related applications. *Atmospheric Measurement Techniques*, *3*(4), 781–811. https://doi.org/10.5194/amt-3-781-2010

Bovensmann, H., Burrows, J. P., Buchwitz, M., Frerick, J., Noël, S., Rozanov, V., Chance, K. V., & Goede, A. P. H. (1999). SCIAMACHY: Mission Objectives and Measurement Modes. *Journal of the Atmospheric Sciences*, *56*(2), 127–150. https://doi.org/10.1175/1520-0469(1999)056<0127:SMOAMM>2.0.CO;2

Bril, A., Oshchepkov, S., & Yokota, T. (2009). Retrieval of atmospheric methane from high spectral resolution satellite measurements: A correction for cirrus cloud effects. *Applied Optics*, *48*(11), 2139–2148. https://doi.org/10.1364/ao.48.002139

Buchwitz, M., Reuter, M., Bovensmann, H., Pillai, D., Heymann, J., Schneising, O., Rozanov, V., Krings, T., Burrows, J. P., Boesch, H., Gerbig, C., Meijer, Y., & Löscher, A. (2013). Carbon Monitoring Satellite (CarbonSat): assessment of atmospheric CO_2 and CH_4 retrieval errors by error parameterization. *Atmospheric Measurement Techniques*, *6*(12), 3477–3500. https://doi.org/10.5194/amt-6-3477-2013

Butz, A., Galli, A., Hasekamp, O. P., Landgraf, J., Tol, P., & Aben, I. (2012). TROPOMI aboard Sentinel-5 Precursor: Prospective performance of CH4 retrievals for aerosol and cirrus loaded atmospheres. *Remote Sensing of Environment*, *120*, 267–276. https://doi.org/10.1016/j.rse.2011.05.030

Butz, A., Guerlet, S., Hasekamp, O. P., Schepers, D., Galli, A., Aben, I., Frankenberg, C., Hartmann, J.-M., Tran, H., Kuze, A., Keppel-Aleks, G., Toon, G. C., Wunch, D., Wennberg, P. O., Deutscher, N., Griffith, D. W. T., Macatangay, R., Messerschmidt, J., Notholt, J., & Warneke, T. (2011). Toward accurate CO 2 and CH 4 observations from GOSAT. *Geophysical Research Letters*, *38*(14), n/a-n/a. https://doi.org/10.1029/2011GL047888

Butz, A., Hasekamp, O. P., Frankenberg, C., & Aben, I. (2009). Retrievals of atmospheric CO2 from simulated space-borne measurements of backscattered near-infrared sunlight: Accounting for aerosol effects. *Applied Optics*, *48*(18), 3322–3336. https://doi.org/10.1364/ao.48.003322

Butz, A., Hasekamp, O. P., Frankenberg, C., Vidot, J., & Aben, I. (2010). CH 4 retrievals from space-based solar backscatter measurements: Performance evaluation against simulated aerosol and cirrus loaded scenes. *Journal of Geophysical Research*, *115*(D24). https://doi.org/10.1029/2010JD014514

Canadell, J. G., Le Quéré, C., Raupach, M. R., Field, C. B., Buitenhuis, E. T., Ciais, P., Conway, T. J., Gillett, N. P., Houghton, R. A., & Marland, G. (2007). Contributions to accelerating atmospheric CO2 growth from economic activity, carbon intensity, and efficiency of natural sinks. *Proceedings of the National Academy of Sciences of the United States of America*, *104*(47), 18866–18870. https://doi.org/10.1073/pnas.0702737104

Connor, B. J., Boesch, H., Toon, G. C., Sen, B., Miller, C. E., & Crisp, D. (2008). Orbiting Carbon Observatory: Inverse method and prospective error analysis. *Journal of Geophysical Research*, *113*(D5), n/a-n/a. https://doi.org/10.1029/2006JD008336

Corazza, M., Bergamaschi, P., Vermeulen, A. T., Aalto, T., Haszpra, L., Meinhardt, F., O'Doherty, S., Thompson, R., Moncrieff, J., Popa, E., Steinbacher, M., Jordan, A., Dlugokencky, E. J., Brühl, C., Krol, M. C., & Dentener, F. (2011). Inverse modelling of European N_2O emissions: assimilating observations from different networks. *Atmospheric Chemistry and Physics*, *11*(5), 2381–2398. https://doi.org/10.5194/acp-11-2381-2011

Crisp, D., Pollock, H. R., Rosenberg, R., Chapsky, L., Lee, R. A. M., Oyafuso, F. A., Frankenberg, C., O'Dell, C. W., Bruegge, C. J., Doran, G. B., Eldering, A., Fisher, B. M., Fu, D., Gunson, M. R., Mandrake, L., Osterman, G. B., Schwandner, F. M., Sun, K., Taylor, T. E., . . . Wunch, D. (2017). The on-orbit performance of the Orbiting Carbon Observatory-2 (OCO-2) instrument and its radiometrically calibrated products. *Atmospheric Measurement Techniques*, *10*(1), 59–81. https://doi.org/10.5194/amt-10-59-2017

Cusworth, D., Duren, R. M., Thorpe, A. K., Eastwood, M. L., Green, R. O., Dennison, P. E., Frankenberg, C., Heckler, J. W., Asner, G., & Miller, C. E. (2021). Quantifying Global Power Plant Carbon Dioxide Emissions With Imaging Spectroscopy. *AGU Advances*, *2*(2). https://doi.org/10.1029/2020AV000350

Cusworth, D., Jacob, D. J., Varon, D. J., Chan Miller, C., Liu, X., Chance, K. V., Thorpe, A. K., Duren, R. M., Miller, C. E., Thompson, D. R., Frankenberg, C., Guanter, L., & Randles, C. A. (2019). Potential of next-generation imaging spectrometers to detect and quantify methane point sources from space. *Atmospheric Measurement Techniques*, *12*(10), 5655–5668. https://doi.org/10.5194/amt-12-5655-2019

DLR. (2022). *DLR CO2Image Mission – focusing on the climate*. https://www.dlr.de/eoc/en/desktopdefault.aspx/tabid-18220/29005_read-77522/

DLR - Institute for Atmospheric Physics. (2022, June 29). *DLR takes a closer look at global CO_2 emissions with a dedicated mission*. https://www.dlr.de/pa/en/desktopdefault.aspx/tabid-2342/6725_read-77610/

Duren, R. M., Guido, J., Herner, J., Rao, S., Green, R. O., Belloy, M. de, Schingler, R., Ardila, D. R., Thorpe, A. K., Cusworth, D., Falk, M., Scheehle, E., Vahlsing, C., Ide, T., Asner, G., & Lawrence, R. (2020). Carbon Mapper: Global tracking of methane and CO2 point-sources. *AGU Fall Meeting Abstracts*, *2020*, A247-01.

EPA. (2016). *Global Greenhouse Gas Emissions Data | US EPA*. https://www.epa.gov/ghgemissions/global-greenhouse-gas-emissions-data

Frankenberg, C., Meirink, J. F., van Weele, M., Platt, U., & Wagner, T. (2005). Assessing methane emissions from global space-borne observations. *Science*, *308*(5724), 1010–1014. https://doi.org/10.1126/science.1106644

Frankenberg, C., Platt, U., & Wagner, T. (2005). Iterative maximum a posteriori (IMAP)-DOAS for retrieval of strongly absorbing trace gases: Model studies for CH_4 and CO_2 retrieval from near infrared spectra of SCIAMACHY onboard ENVISAT. *Atmospheric Chemistry and Physics*, *5*(1), 9–22. https://doi.org/10.5194/acp-5-9-2005

Grace, J. (2004). Understanding and managing the global carbon cycle. *Journal of Ecology*, *92*(2), 189–202. https://doi.org/10.1111/j.0022-0477.2004.00874.x

Guanter, L., Irakulis-Loitxate, I., Gorroño, J., Sánchez-García, E., Cusworth, D., Cogliati, S., Colombo, R., & Varon, D. J. (2022). *Mapping methane point emissions with the PRISMA spaceborne imaging spectrometer*. California Digital Library (CDL). https://doi.org/10.31223/x5vc9c

Guerlet, S., Butz, A., Schepers, D., Basu, S., Hasekamp, O. P., Kuze, A., Yokota, T., Blavier, J.-F., Deutscher, N., Griffith, D. W. T., Hase, F., Kyro, E., Morino, I., Sherlock, V., Sussmann, R., Galli, A., & Aben, I. (2013). Impact of aerosol and thin cirrus on retrieving and validating XCO 2 from GOSAT shortwave infrared measurements. *Journal of Geophysical Research: Atmospheres*, *118*(10), 4887–4905. https://doi.org/10.1002/jgrd.50332

Gurney, K. R., Liang, J., O'Keeffe, D., Patarasuk, R., Hutchins, M., Huang, J., Rao, P., & Song, Y. (2019). Comparison of Global Downscaled Versus Bottom-Up Fossil Fuel CO 2 Emissions at the Urban Scale in Four U.S. Urban Areas. *Journal of Geophysical Research: Atmospheres*, *124*(5), 2823–2840. https://doi.org/10.1029/2018JD028859

Gurney, K. R., Razlivanov, I., Song, Y., Zhou, Y., Benes, B., & Abdul-Massih, M. (2012). Quantification of fossil fuel CO2 emissions on the building/street scale for a large U.S. City. *Environmental Science & Technology*, *46*(21), 12194–12202. https://doi.org/10.1021/es3011282

Hasekamp, O. P., & Butz, A. (2008). Efficient calculation of intensity and polarization spectra in vertically inhomogeneous scattering and absorbing atmospheres. *Journal of Geophysical Research*, *113*(D20). https://doi.org/10.1029/2008JD010379

Hergert, W., & Wriedt, T. (Eds.). (2015). *Springer series in optical sciences: Vol. 169*. *The Mie theory: Basics and applications*. Springer.

Hirsch, A. I., Michalak, A. M., Bruhwiler, L. M., Peters, W., Dlugokencky, E. J., & Tans, P. P. (2006). Inverse modeling estimates of the global nitrous oxide surface flux from 1998-2001. *Global Biogeochemical Cycles*, *20*(1), n/a-n/a. https://doi.org/10.1029/2004GB002443

Hogue, S., Marland, E., Andres, R., Marland, G., & Woodard, D. (2016). Uncertainty in gridded CO 2 emissions estimates. *Earth's Future*, *4*(5), 225–239. https://doi.org/10.1002/2015EF000343

Houweling, S., Bergamaschi, P., Chevallier, F., Heimann, M., Kaminski, T., Krol, M. C., Michalak, A. M., & Patra, P. (2017). Global inverse modeling of CH_4 sources and sinks: an overview of methods. *Atmospheric Chemistry and Physics*, *17*(1), 235–256. https://doi.org/10.5194/acp-17-235-2017

Huang, Y [Yunxia], Natraj, V., Zeng, Z.-C., Kopparla, P., & Yung, Y. L. (2020). Quantifying the impact of aerosol scattering on the retrieval of methane from airborne

remote sensing measurements. *Atmospheric Measurement Techniques*, *13*(12), 6755–6769. https://doi.org/10.5194/amt-13-6755-2020

ICON. (2022). *ICON-ESM.* Max-Planck-Institut für Meteorologie Hamburg. https://mpimet.mpg.de/en/science/models/icon-esm/

IEA. (2019). *Global Energy and CO2 Status Report 2018: The latest trends in energy and emissions in 2018*. https://www.iea.org/reports/global-energy-co2-status-report-2019

IPCC (Ed.). (2014). *Climate change 2014: Working group 3*. *Climate change 2014: Mitigation of climate change ; Working Group III contribution to the Fifth Assessment Report of the Intergovernmental Panel on Climate Change*. Cambridge Univ. Press. http://www.loc.gov/catdir/enhancements/fy1606/2014451899-d.html

IPCC (Ed.). (2021). *Climate Change 2021: The Physical Science Basis. Contribution of Working Group I to the Sixth Assessment Report of the Intergovernmental Panel on Climate Change.*

IPCC (Ed.). (2022). *Climate Change 2022: Summary for Policymakers Mitigation of Climate Change; Working Group III Contribution to the Sixth Assessment Report of the Intergovernmental Panel on Climate Change*. Cambridge University Press.

Jacob, D. J., Varon, D. J., Cusworth, D., Dennison, P. E., Frankenberg, C., Gautam, R., Guanter, L., Kelley, J., McKeever, J., Ott, L. E., Poulter, B., Qu, Z., Thorpe, A. K., Worden, J. R., & Duren, R. M. (2022). *Quantifying methane emissions from the global scale down to point sources using satellite observations of atmospheric methane.* https://doi.org/10.5194/acp-2022-246

Jervis, D., McKeever, J., Durak, B. O. A., Sloan, J. J., Gains, D., Varon, D. J., Ramier, A., Strupler, M., & Tarrant, E. (2021). The GHGSat-D imaging spectrometer. *Atmospheric Measurement Techniques*, *14*(3), 2127–2140. https://doi.org/10.5194/amt-14-2127-2021

Kuhlmann, G., Broquet, G., Marshall, J., Clément, V., Löscher, A., Meijer, Y., & Brunner, D. (2019). Detectability of CO_2 emission plumes of cities and power plants with the Copernicus Anthropogenic CO_2 Monitoring (CO2M) mission. *Atmospheric Measurement Techniques*, *12*(12), 6695–6719. https://doi.org/10.5194/amt-12-6695-2019

Kuhlmann, G., Henne, S., Meijer, Y., & Brunner, D. (2021). Quantifying CO2 Emissions of Power Plants With CO2 and NO2 Imaging Satellites. *Frontiers in Remote Sensing*, *2*, Article 689838. https://doi.org/10.3389/frsen.2021.689838

Kuze, A., Suto, H., Shiomi, K., Kawakami, S., Tanaka, M., Ueda, Y., Deguchi, A., Yoshida, J., Yamamoto, Y., Kataoka, F., Taylor, T. E., & Buijs, H. L. (2016). Update on GOSAT TANSO-FTS performance, operations, and data products after more than 6 years in space. *Atmospheric Measurement Techniques*, *9*(6), 2445–2461. https://doi.org/10.5194/amt-9-2445-2016

Lock, J. A., & Gouesbet, G. (2009). Generalized Lorenz–Mie theory and applications. *Journal of Quantitative Spectroscopy and Radiative Transfer*, *110*(11), 800–807. https://doi.org/10.1016/j.jqsrt.2008.11.013

Lorente, A., Borsdorff, T., Butz, A., Hasekamp, O. P., Brugh, J. aan de, Schneider, A., Wu, L., Hase, F., Kivi, R., Wunch, D., Pollard, D., Shiomi, K., Deutscher, N., Velazco, V. A., Roehl, C. M., Wennberg, P. O., Warneke, T., & Landgraf, J. (2021). Methane retrieved from TROPOMI: improvement of the data product and

validation of the first 2 years of measurements. *Atmospheric Measurement Techniques*, *14*(1), 665–684. https://doi.org/10.5194/amt-14-665-2021

Miller, S. M., & Michalak, A. M. (2017). Constraining sector-specific CO_2 and CH_4 emissions in the US. *Atmospheric Chemistry and Physics*, *17*(6), 3963–3985. https://doi.org/10.5194/acp-17-3963-2017

Mishchenko, M. I., Geogdzhayev, I. V., Cairns, B., Rossow, W. B., & Lacis, A. A. (1999). Aerosol retrievals over the ocean by use of channels 1 and 2 AVHRR data: Sensitivity analysis and preliminary results. *Applied Optics*, *38*(36), 7325–7341. https://doi.org/10.1364/ao.38.007325

MPI. (2022, November 21). *Department Biogeochemical Systems | ARS / TCCON Maps.* Max Planck Institute for Biogeochemistry. https://www.bgc-jena.mpg.de/bgc-systems/index.php/ARS/TCCONMaps

Nassar, R., Hill, T. G., McLinden, C. A., Wunch, D., Jones, D. B. A., & Crisp, D. (2017). Quantifying CO 2 Emissions From Individual Power Plants From Space. *Geophysical Research Letters*, *44*(19). https://doi.org/10.1002/2017GL074702

Nisbet, E., & Weiss, R. (2010). Atmospheric science. Top-down versus bottom-up. *Science (New York, N.Y.)*, *328*(5983), 1241–1243. https://doi.org/10.1126/science.1189936

NOAA. (2022a). *Global Monitoring Laboratory - CarbonTracker CT2019B*. https://gml.noaa.gov/ccgg/carbontracker/

NOAA. (2022b, June 27). *Climate Change: Atmospheric Carbon Dioxide*. https://www.climate.gov/news-features/understanding-climate/climate-change-atmospheric-carbon-dioxide

Oda, T., Maksyutov, S., & Andres, R. (2018). The Open-source Data Inventory for Anthropogenic Carbon dioxide (CO2), version 2016 (ODIAC2016): A global, monthly fossil-fuel CO2 gridded emission data product for tracer transport simulations and surface flux inversions. *Earth System Science Data*, *10*(1), 87–107. https://doi.org/10.5194/essd-10-87-2018

Parker, R. J., Webb, A., Boesch, H., Somkuti, P., Barrio Guillo, R., Di Noia, A., Kalaitzi, N., Anand, J., Bergamaschi, P., Chevallier, F., Palmer, P. I., Feng, L., Deutscher, N., Feist, D. G., Griffith, D. W. T., Hase, F., Kivi, R., Morino, I., Notholt, J., . . . Wunch, D. (2020). A decade of GOSAT Proxy satellite CH_4 observations. *Earth System Science Data*, *12*(4), 3383–3412. https://doi.org/10.5194/essd-12-3383-2020

Payne, R. E. (1972). Albedo of the Sea Surface. *Journal of the Atmospheric Sciences*, *29*(5), 959–970. https://doi.org/10.1175/1520-0469(1972)029<0959:AOTSS>2.0.CO;2

Peters, W., Jacobson, A. R., Sweeney, C., Andrews, A. E., Conway, T. J., Masarie, K., Miller, J. B., Bruhwiler, L. M. P., Pétron, G., Hirsch, A. I., Worthy, D. E. J., van der Werf, G. R., Randerson, J. T., Wennberg, P. O., Krol, M. C., & Tans, P. P. (2007). An atmospheric perspective on North American carbon dioxide exchange: Carbontracker. *Proceedings of the National Academy of Sciences of the United States of America*, *104*(48), 18925–18930. https://doi.org/10.1073/pnas.0708986104

Petty, G. W. (2006). *A first course in atmospheric radiation* (2. ed.). Sundog Publ.

Pöschl, U. (2005). Atmospheric aerosols: Composition, transformation, climate and health effects. *Angewandte Chemie (International Ed. In English)*, *44*(46), 7520–7540. https://doi.org/10.1002/anie.200501122

Prentice, I., Farquhar, G., Fasham, M., Goulden, M., Heimann, M., Jaramillo, V., Kheshgi, H., Le Quéré, C., Scholes, R., Wallace, D., Archer, D., Ashmore, M., Aumont, O., Baker, D., Battle, M., Bender, M., Bopp, L., Bousquet, P., Caldeira, K., . . . Yool, A. (2001). *The carbon cycle and atmospheric carbon dioxide*. https://hal.archives-ouvertes.fr/hal-03333974

Reuter, M., Buchwitz, M., Schneising, O., Krautwurst, S., O'Dell, C. W., Richter, A., Bovensmann, H., & Burrows, J. P. (2019). Towards monitoring localized CO_2 emissions from space: co-located regional CO_2 and NO_2 enhancements observed by the OCO-2 and S5P satellites. *Atmospheric Chemistry and Physics*, *19*(14), 9371–9383. https://doi.org/10.5194/acp-19-9371-2019

Reuter, M., Buchwitz, M., Schneising, O., Noël, S., Bovensmann, H., Burrows, J. P., Boesch, H., Di Noia, A., Anand, J., Parker, R. J., Somkuti, P., Wu, L., Hasekamp, O. P., Aben, I., Kuze, A., Suto, H., Shiomi, K., Yoshida, Y., Morino, I., . . . Schepers, D. (2020). Ensemble-based satellite-derived carbon dioxide and methane column-averaged dry-air mole fraction data sets (2003–2018) for carbon and climate applications. *Atmospheric Measurement Techniques*, *13*(2), 789–819. https://doi.org/10.5194/amt-13-789-2020

Román-Palacios, C., & Wiens, J. J. (2020). Recent responses to climate change reveal the drivers of species extinction and survival. *Proceedings of the National Academy of Sciences of the United States of America*, *117*(8), 4211–4217. https://doi.org/10.1073/pnas.1913007117

Sánchez-García, E., Gorroño, J., Irakulis-Loitxate, I., Varon, D. J., & Guanter, L. (2022). Mapping methane plumes at very high spatial resolution with the WorldView-3 satellite. *Atmospheric Measurement Techniques*, *15*(6), 1657–1674. https://doi.org/10.5194/amt-15-1657-2022

Schwandner, F. M., Gunson, M. R., Miller, C. E., Carn, S. A., Eldering, A., Krings, T., Verhulst, K. R., Schimel, D. S., Nguyen, H. M., Crisp, D., O'Dell, C. W., Osterman, G. B., Iraci, L. T., & Podolske, J. R. (2017). Spaceborne detection of localized carbon dioxide sources. *Science (New York, N.Y.)*, *358*(6360). https://doi.org/10.1126/science.aam5782

Seidel, D. J., Ao, C. O., & Li, K. (2010). Estimating climatological planetary boundary layer heights from radiosonde observations: Comparison of methods and uncertainty analysis. *Journal of Geophysical Research*, *115*(D16). https://doi.org/10.1029/2009JD013680

Sentinel-2. (2022). *Sentinel-2 - Data Products - Sentinel Handbook - Sentinel Online*. https://sentinel.esa.int/web/sentinel/missions/sentinel-%202/data-products

Sentinel-5P. (2022). *Sentinel-5 Precursor Level 1B Irradiances - Sentinel Online*. https://sentinels.copernicus.eu/web/sentinel/data-products/-/asset_publisher/fp37fc19FN8F/content/id/4673574

Sierk, B., Fernandez, V., Bézy, J.-L., Meijer, Y., Durand, Y., Bazalgette Courrèges-Lacoste, G., Pachot, C., Löscher, A., Nett, H., Minoglou, K., Boucher, L., Windpassinger, R., Pasquet, A., Serre, D., & te Hennepe, F. (2021, March 30 – April 2). The Copernicus CO2M mission for monitoring anthropogenic carbon dioxide emissions from space. In Z. Sodnik, B. Cugny, & N. Karafolas (Eds.), *International Conference on Space Optics — ICSO 2020* (p. 128). SPIE. https://doi.org/10.1117/12.2599613

Stephens, G. L., O'Brien, D., Webster, P. J., Pilewski, P., Kato, S., & Li, J. (2015). The albedo of Earth. *Reviews of Geophysics*, *53*(1), 141–163. https://doi.org/10.1002/2014RG000449

Strandgren, J., Krutz, D., Wilzewski, J. S., Paproth, C., Sebastian, I., Gurney, K. R., Liang, J., Roiger, A., & Butz, A. (2020). Towards spaceborne monitoring of localized CO_2 emissions: an instrument concept and first performance assessment. *Atmospheric Measurement Techniques*, *13*(6), 2887–2904. https://doi.org/10.5194/amt-13-2887-2020

Turnbull, J. C., Keller, E. D., Norris, M. W., & Wiltshire, R. M. (2016). Independent evaluation of point source fossil fuel CO2 emissions to better than 10%. *Proceedings of the National Academy of Sciences of the United States of America*, *113*(37), 10287–10291. https://doi.org/10.1073/pnas.1602824113

Varon, D. J., Jacob, D. J., McKeever, J., Jervis, D., Durak, B. O. A., Xia, Y., & Huang, Y [Yi] (2018). Quantifying methane point sources from fine-scale satellite observations of atmospheric methane plumes. *Atmospheric Measurement Techniques*, *11*(10), 5673–5686. https://doi.org/10.5194/amt-11-5673-2018

Varon, D. J., Jervis, D., McKeever, J., Spence, I., Gains, D., & Jacob, D. J. (2021). High-frequency monitoring of anomalous methane point sources with multispectral Sentinel-2 satellite observations. *Atmospheric Measurement Techniques*, *14*(4), 2771–2785. https://doi.org/10.5194/amt-14-2771-2021

Velazco, V. A., Buchwitz, M., Bovensmann, H., Reuter, M., Schneising, O., Heymann, J., Krings, T., Gerilowski, K., & Burrows, J. P. (2011). Towards space based verification of CO_2 emissions from strong localized sources: fossil fuel power plant emissions as seen by a CarbonSat constellation. *Atmospheric Measurement Techniques*, *4*(12), 2809–2822. https://doi.org/10.5194/amt-4-2809-2011

Vermote, E., Justice, C., Claverie, M., & Franch, B. (2016). Preliminary analysis of the performance of the Landsat 8/OLI land surface reflectance product. *Remote Sensing of Environment*, *Volume 185*(Iss 2), 46–56. https://doi.org/10.1016/j.rse.2016.04.008

Wilzewski, J. S., Roiger, A., Strandgren, J., Landgraf, J., Feist, D. G., Velazco, V. A., Deutscher, N., Morino, I., Ohyama, H., Té, Y. V., Kivi, R., Warneke, T., Notholt, J., Dubey, M., Sussmann, R., Rettinger, M., Hase, F., Shiomi, K., & Butz, A. (2020). Spectral sizing of a coarse-spectral-resolution satellite sensor for XCO_2. *Atmospheric Measurement Techniques*, *13*(2), 731–745. https://doi.org/10.5194/amt-13-731-2020

Wu, L., Hasekamp, O. P., Hu, H., Landgraf, J., Butz, A., Brugh, J. aan de, Aben, I., Pollard, D. F., Griffith, D. W. T., Feist, D. G., Koshelev, D., Hase, F., Toon, G. C., Ohyama, H., Morino, I., Notholt, J., Shiomi, K., Iraci, L., Schneider, M., . . . Té, Y. V. (2018). Carbon dioxide retrieval from OCO-2 satellite observations using the RemoTeC algorithm and validation with TCCON measurements. *Atmospheric Measurement Techniques*, *11*(5), 3111–3130. https://doi.org/10.5194/amt-11-3111-2018

Wunch, D., Toon, G. C., Blavier, J.-F. L., Washenfelder, R. A., Notholt, J., Connor, B. J., Griffith, D. W. T., Sherlock, V., & Wennberg, P. O. (2011). The total carbon column observing network. *Philosophical Transactions. Series A, Mathematical, Physical, and Engineering Sciences*, *369*(1943), 2087–2112. https://doi.org/10.1098/rsta.2010.0240

Wunch, D., Wennberg, P. O., Osterman, G. B., Fisher, B. M., Naylor, B., Roehl, C. M., O'Dell, C. W., Mandrake, L., Viatte, C., Kiel, M., Griffith, D. W. T., Deutscher, N., Velazco, V. A., Notholt, J., Warneke, T., Petri, C., Maziere, M. de, Sha, M. K., Sussmann, R., . . . Eldering, A. (2017). Comparisons of the Orbiting Carbon Observatory-2 (OCO-2) X_{CO2} measurements with TCCON. *Atmospheric Measurement Techniques*, *10*(6), 2209–2238. https://doi.org/10.5194/amt-10-2209-2017

Yiğit, E., & Medvedev, A. S. (2019). Obscure waves in planetary atmospheres. *Physics Today*, *72*(6), 40–46. https://doi.org/10.1063/PT.3.4226

Zhang, M., Leifer, I., & Hu, C. (2017). Challenges in Methane Column Retrievals from AVIRIS-NG Imagery over Spectrally Cluttered Surfaces: A Sensitivity Analysis. *Remote Sensing*, *9*(8), 835. https://doi.org/10.3390/rs9080835

Zhou, M., Dils, B., Wang, P., Detmers, R., Yoshida, Y., O'Dell, C. W., Feist, D. G., Velazco, V. A., Schneider, M., & Maziere, M. de (2016). Validation of TANSO-FTS/GOSAT XCO_2 and XCH_4 glint mode retrievals using TCCON data from near-ocean sites. *Atmospheric Measurement Techniques*, *9*(3), 1415–1430. https://doi.org/10.5194/amt-9-1415-2016

A Moving RemoTeC from DKRZ's supercomputer "Mistral" to "Levante"

The previous described full physics algorithm RemoTeC used for this work is running on the Supercomputer for Earth System Research of the DKRZ. This high-performance computer is the fourth supercomputer at DKRZ and is called "Levante". The last years climate research was running on "Mistral", the predecessor model of Levante. But after six years the DKRZ changed from Mistral to Levante, because Levante has more calculation capacity due to more cores and is therefore faster in the calculation process. The transition period from moving from Mistral to Levante went from March 3, 2022 until the end of May, 2022. Since then, Mistral is no longer available. To transfer the algorithm from Mistral to Levante and get it properly running, brought some challenges, which are described in this section.

The full physics algorithm RemoTeC was provided by Prof. Dr. André Butz at the University Heidelberg and transferred from their server with the help of Leon Scheidweiler to Mistral in February 2022 to give access to the DLR. After a few problems the algorithm was compiled and running at Mistral.

As Mistral would not be available from June on any longer, everything needed to be moved from Mistral to Levante in the transition period. After compiling on Levante, first simulations have been tried. But the simulations were always cancelled without giving any error or warning messages. It was discovered that in the ATM_OUT-File, created in the forward run and used in the retrieval, the parameter for total optical thickness used to simulate spectrum (Ot_inp), had the value of exactly zero in simulations on Mistral whereas simulations on Levante filled the parameter Ot_inp with "NaN"'s. Furthermore, the parameter for cirrus optical thickness, used to simulate spectrum (Cot_inp) differed from Mistral to Levante slightly from 10^{-324} to 10^{-312}. Also, in the L1B file the radiance value differed slightly from the run on Mistral to the run on Levante.

During the time of searching for the reason of this difference, maintenance on Levante was and is still going on. Surprisingly, simulations on Levante been possible without having the before mentioned differences for around a week. However, since June 20, 2022 the retrieval simulations on Levante were cancelled again. The main problem was that the parameter about the window spectra structure was not initialized and

therefore the algorithm used whatever was in the memory as start value. After adding "win%ot = 0.0" to the code, the simulations on Levante are running. Still, it was unknown if there are any hidden problems. For this reason, an analysis about the differences of Mistral runs to simulations on Levante was performed, in order to also find possible hidden errors or differences.

Figure A.1 shows the CO_2 plume of a simulation with RemoTeC on Levante for a scene used in the sensitivity studies of this work. The differences, going from -10 ppm to +10 ppm, between two runs on Mistral and between Mistral and Levante are also visualized and do not vary significantly. The highest differences come from different noise in the background. Now having a realistic plume from the retrieval, there are no assumptions of any hidden problems on Levante anymore. To relieve doubt, simulations with fixed seed values have been made. Differences between these runs are zero for every pixel and ensure the reproducibility of following studies.

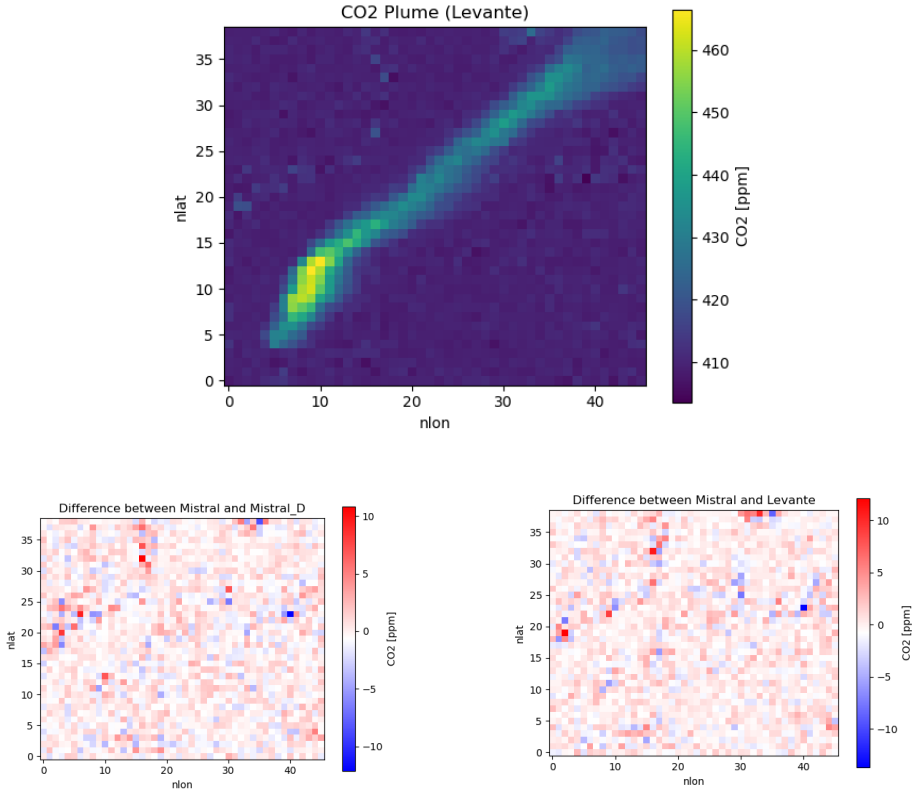

Figure A.1: CO2 Plume of the Simulation on Levante (upper), Differences in ppm between runs on Mistral (down left) and differences between runs on Mistral and on Levante (down right)

B Additional figures

Figure B.1 shows simulations on Levante with pixels having very high CO_2 concentrations. These pixels come from randomly added noise error. To solve this problem the seed for all simulations was set constantly to 3.1415. By having the same noise error for every pixel, these very high CO_2 values did not occur anymore what makes it possible to compare differences caused by environmental parameters and not by noise error. Precisely, with a fixed seed it is possible to compare the simulations and it is ensured that the observed differences are caused by the changed parameter. Furthermore, a fixed seed makes the simulations and also the analysis reproducible.

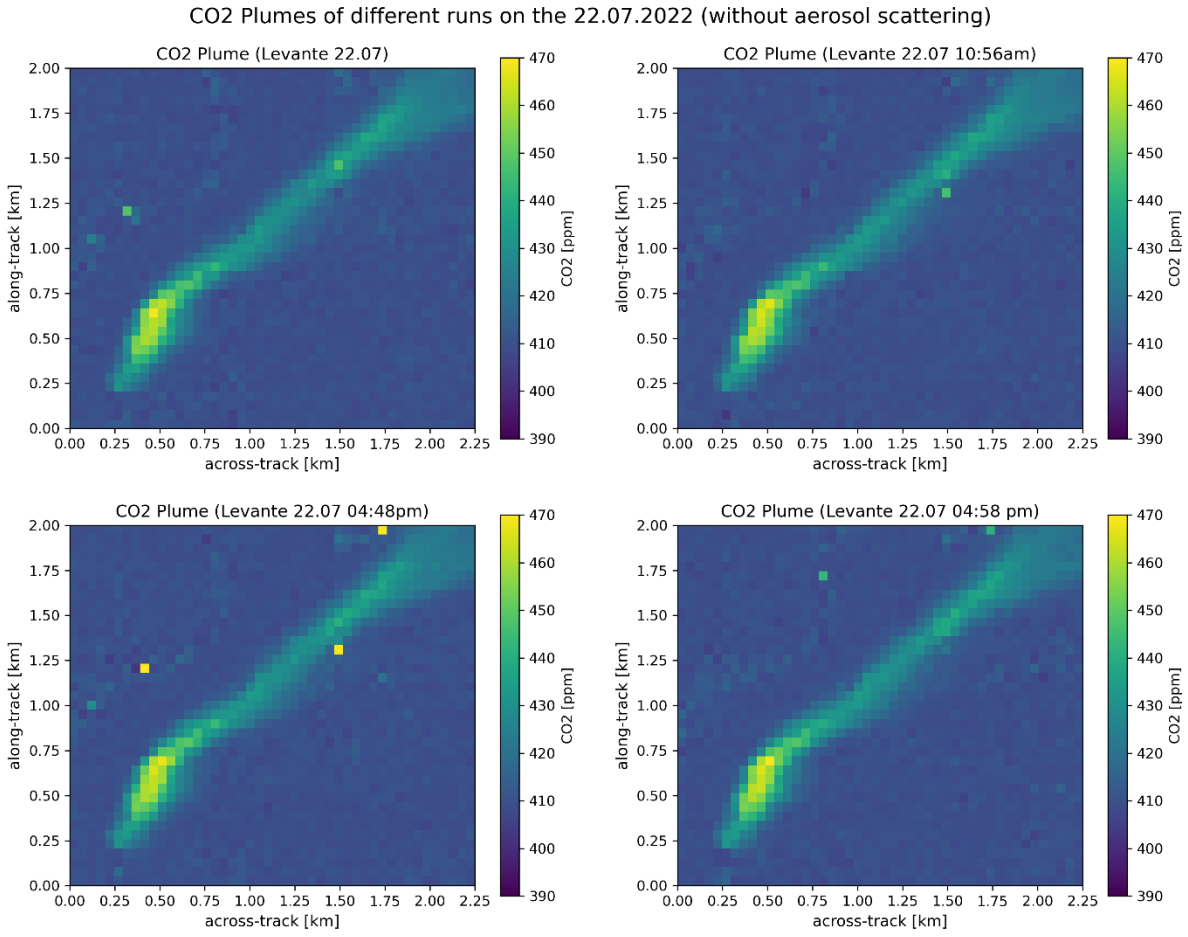

Figure B.1: Different runs of the retrieval algorithm RemoTeC on Levante. The simulations were performed without considering aerosol scattering. The problem of having pixels with very high CO2 concentrations occurred due to variable seed noise. Therefore, the seed was set to the value 3.1415 so solve this problem.

C Performing aerosol studies with RemoTeC

The aerosol studies in this thesis were performed with the retrieval algorithm RemoTeC. A detailed description of RemoTeC can be found in the PDF "RemoTeC_how_to_use" which was provided with the algorithm by Prof. Dr. André Butz and Leon Scheidweiler. Figure C.1 shows the main structure of the RemoTeC. The structure of the folder CO2IMAGE_REMOTEC is divided into the two executables RemoTeC_create and RemoTeC_sim. The SRC folder contains the source code with sim_create to simulate the spectra and sim_retrieval for the retrieval.

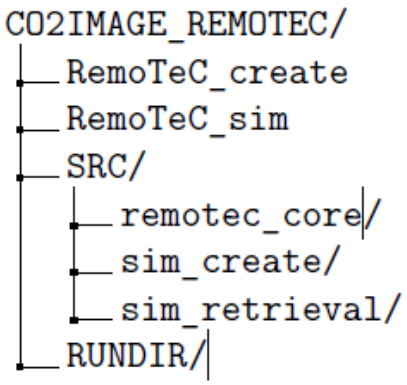

Figure C.1: Main folder structure of the retrieval algorithm RemoTeC.

The input and output files are provided in a netCDF4 format. Different simulations with varying values for the aerosol parameters aerosol optical thickness, aerosol height distribution and aerosol size distribution were performed.

To be able to perform the aerosol studies with RemoTeC the following modifications been necessary:

- Cores: on Levante change cores (more than on Mistral and with aerosol scattering it takes too long, so more cores needed): "CO2Image_Scripts/configs/templates/default/default.ini"
- fixed seed: same noise on every run to be able to compare: CO2Image_RemoteC/SRC/sim_create/calculate_syn_spectrum.f90: "errini=3.1415"

- make: CO2Image_RemoteC makefile, then run simulations with: CO2Image_Scripts: “. full.simulations.sh configs/default/default.ini”
- Aerosol scattering: include aerosol template for activating aerosol scattering: “CO2Image_Scripts/configs/templates/default/default.ini: change path to file “ settings_RTC_create_AEROSOL_LEVANTE”
  In this file also the aerosol parameters are defined and can be changed.
- Different Albedo scenarios: different netCDF files with different albedo scenarios are used for the simulations on RemoTeC

Eigenständigkeitserklärung

Hiermit versichere ich, die vorliegende Arbeit selbständig und nur unter Verwendung der angegebenen Hilfsmittel und Quellen angefertigt habe. Die eingereichte Arbeit ist nicht anderweitig als Prüfungsleistung verwendet worden oder in englischer, deutscher oder einer anderen Sprache als Veröffentlichung erschienen.

Jena, 24.11.2022

Ort, Datum

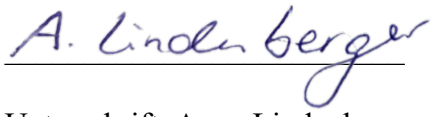

Unterschrift, Anna Lindenberger